Evaluation of the Crack Initiation and Crack Growth Characteristics in Hybrid Titanium Composite Laminates via In Situ Radiography

A Thesis
Presented to
The Academic Faculty

by

Matthew Wesley Hammond

In Partial Fulfillment
Of the Requirements for the Degree
Master of Science in Mechanical Engineering

Georgia Institute of Technology
December 2005

EVALUATION OF THE CRACK INITIATION AND CRACK GROWTH CHARACTERISTICS IN HYBRID TITANIUM COMPOSITE LAMINATES VIA IN SITU RADIOGRAPHY

Approved by:

Dr. W. Steven Johnson, Advisor
School of Materials Science and Engineering
School of Mechanical Engineering
Georgia Institute of Technology

Dr. Christopher Lynch
School of Mechanical Engineering
Georgia Institute of Technology

Dr. Rami Haj-Ali
School of Civil Engineering
Georgia Institute of Technology

Date Approved: August 08, 2005

In loving memory

of

my little girl

Ava Camille Hammond

Nov 4, 2002

ACKNOWLEDGEMENTS

There are a number of people who were instrumental in completion of this research, without them this would have not been possible. First, I would like to thank my advisor, Dr. W. Steven Johnson, for his guidance and opportunity to work on this project. The positive working environment that Dr. Johnson fosters provided me, as a member of Team Johnson, with a great deal of freedom to explore various scientific avenues in completion of this research. In addition I would like to thank Dr. Christopher Lynch and Dr. Rami Haj-Ali for their time, hands on support and insight, as members of my thesis committee.

Mr. Rick Brown, Georgia Institute of Technology Mechanical Properties Research Laboratory Head Technician, your support was vital to the completion of this work, your life stories inspire (or frighten) and your friendship will always be appreciated. Mr. Robert Cooper, I send my thanks for your help with strain gaging and testing control software issues.

Mr. Bill Westre and Mr. Edward Li, Boeing Company technical advisors, thank you for your trust, input and advice. Ms. Julie Duyree and Dr. Kip Findley I appreciate the excellent work and time volunteered to complete the microscopy of the titanium foils. Also I would like to thank Mr. Shane Johnson, Mr. Hoan Kee Kim, and Mr. Bo-Siou Wei, of Dr. Haj-Ali's research group, for teaching me the finer points of TSA and helping with my research.

To Mr. Rem Dubose, a true Yellow Jacket, I appreciate your help and encouragement to study at this great institution. I thank the Coast Guard, Office of Naval Engineering, for a great career and sponsoring my studies.

To my friends and peers I send the following gratitude. Mr. Kyle Webber, thank you for letting me know where I stand and helping a fellow sailor along. Mr. Paul Treasurer, I thank you for helping me with the analytical analysis and the lab entomology. Major Don "Big Daddy" Rhymer, I thank you for the HTCL conversation and coffee. Mrs. Amelia Case McVay, thank you for help with matrix reduction and being a good friend. Ms. Carrell Weeks, I appreciate the help in technical writing and formatting. Mr. Shelby Highsmith, thank you for helping with microscopy. And finally to Mr. Amar Atre, my brother, thank you for the finite element modeling and most importantly your friendship.

Ann and Bob Tankersley, my in-laws, I appreciate all that you have done for me and most importantly for my family during the course of my studies.

I would like to thank my parents, Gwen and Rich Hammond, for all the support that they have given me and my family during my life and graduate career

Finally I would like to thank my family, Loren, Spencer, Caroline and coming soon Lilly, for their love, smiles and reminding me everyday my most important job is being a "Hubbie" and "Daddy".

TABLE OF CONTENTS

LIST OF TABLES

LIST OF FIGURES

LIST OF SYMBOLS

α	alpha precipitate
β	beta precipitate
ε	strain
σ	stress
ν	Poisson's ratio
1025 HT	STA 1025 Ti foil heat treatment
1100 HT	STA 1100 Ti foil heat treatment
ASTM	American Society for Testing and Materials
AR	as received Ti foil heat treatment
ARALL	aramid fiber composite aluminum laminate
at.%	atomic percent
BCC	body center cubic, crystalline microstructure
°C	degrees Celsius, unit measure of temperature
cm	centimeters, unit measure of length - 10^{-2} meters
CTE	coefficient of thermal expansion
E	Young's modulus
°F	degrees Fahrenheit, unit measure of temperature
f	subscript designation for fiber properties
FCG	fatigue crack growth
FML	fiber metal laminate
g	gram, unit measure of mass

GLARE	glass fiber composite aluminum laminates
GPa	gigapascal, unit measure of stress - 10^9 Pascals
HCF	high cycle fatigue
HCP	hexagonal close pack, crystalline microstructure
HTCL	hybrid titanium composite laminate
in	inch, unit measure of length
hrs	hour, unit measure of time - 3600 seconds
kip	kilopounds-force, unit measure of load - 10^3 lb
ksi	kilopounds-force/inch^2, unit measure of stress - 10^3 psi
kV	kilo volt, unit measure of voltage - 10^3 volts
L	subscript designation for overall laminate properties
lb_f	force pound, unit measure of force
LCF	low cycle fatigue
m	subscript designation for matrix properties
μm	micrometer, unit measure of length – 10^{-6} meters
min	minute, unit measure of time – 60 seconds
ml	milliliter, unit measure of volume – 10^{-3} liters
mm	millimeter, unit measure of length – 10^{-3} meters
mm/mm	unit measure of strain
ME	mechanical engineering
MPa	megapascal, unit measure of stress – 10^6 Pascals
MPRL	Material Properties Research Laboratory, Georgia Tech
Msi	megapounds-force/inch^2, unit measure of stress – 10^6 psi

MSE	material science engineering
MTS	Mechanical Testing and Simulation, company
N	Newton, unit measure of force
Pa	Pascals, unit measure of stress
PA	primary annealed microstructure
PMC	polymer matrix composite
RD	roll direction
RT	room temperature
sec	seconds, unit measure of time
SN	solution treated Ti foil heat treatment
T	temperature
UTS	ultimate tensile strength
v_f	fiber volume fraction
YS	yield strength

SUMMARY

Hybrid Titanium Composite Laminates (HTCL) have vast potential for future commercial aircraft development. In order for this potential to be properly utilized the HTCL's material properties must first be well understood and obtained through experimentation. Crack initiation and crack growth characteristics of HTCLs are dependent on the heat treatment of the embedded constituent titanium foil. While high strength titanium foils may delay crack initiation, there may be an adverse effect of unsuitable crack growth rates in the HTCLs. Literature has indicated that when properly designed, cracks in HTCLs can arrest due to fiber bridging mechanisms and other crack closure mechanisms. Traditional surface inspection techniques employed on facesheet laminate evaluations will not be able to properly monitor the internal crack growth and damage progression for the internal plies.

The main objective of the this joint Georgia Tech/Boeing research project was to determine and compare crack initiation and crack growth characteristics of different heat-treated β-Ti 15-3 titanium foil embedded in HTCLs. Georgia Tech utilized a unique capability of x-raying the internal foils of the HTCL specimen in a servo-hydraulic test frame while under load. The titanium foil in this study represented four different heat treatments that result in four increasing levels of strength and decreasing levels of elongation. Specifically, open-hole HTCL coupons were tested at four stress load levels under constant amplitude fatigue cycles to determine a-N curves for the HTCL layups evaluated. The layup evaluated was [45/0/-45/0/Ti/0/-45/0/45]. Crack growth rates were determined once the initiated crack was detected via radiographic exposure.

Radiographic delamination analysis and thermoelastic stress analysis techniques were employed to determine additional damage mechanisms in the laminate. Analytical and finite element methods were utilized to determine ply stresses. Additionally, titanium foil properties were determined via dog-bone coupons for each of the four heat treatment conditions.

CHAPTER 1

INTRODUCTION

With the introduction of commercial aircraft designed primarily with composite materials, such as the Boeing 787, there exists a need to overcome the short comings of traditional composite designs. These applications call for materials which possess composites traditionally high performance characteristics, but also require that they be able withstand the introduction of damage mechanisms without catastrophic failure. This requirement for system durability has created a whole generation of materials that combine existing materials to form a new system that rivals either constituent part. The synergy created takes advantages of both while minimizing their disadvantages. This need led to the development of fiber metal laminates which combine the two well understood aerospace materials of metal and fiber reinforced polymer matrix composite.

Fiber metal laminates (FML) are a hybrid material consisting of thin, high-strength, metal sheets alternately bonded to plies of layers of fiber-reinforced epoxy adhesive. FML possess the advantages of both metals and polymer matrix composites (PMC) while minimizing their respective disadvantages [1]. The high strength to weight ratio is achieved while composite anisotropy is minimized. Also, several variants of FML have all consistently shown superior damage tolerance that neither the metal nor fiber polymer matrix composites (PMC) possess.

Hybrid Titanium Composite Laminates (HTCL), one of a number of Fiber Metal Laminate (FML) systems, have vast potential for future commercial aircraft development. In order for this potential to be properly utilized the HTCL's material properties must

first be well understood and obtained through experimentation. Crack initiation and crack growth characteristics of HTCLs are dependent on the heat treatment of the embedded constituent titanium foil among other factors. While high strength titanium foils may delay crack initiation, there may be an adverse effect of unsuitable crack growth rates in the HTCLs. Literature has indicated that when properly designed, cracks in HTCLs can arrest due to fiber bridging mechanisms and other crack closure mechanisms. Traditional surface inspection techniques employed on facesheet laminate evaluations cannot properly monitor the internal crack growth and damage progression for the internal plies. The purpose of this research project was to determine the crack growth characteristics of an embedded titanium ply within a HTCL system. Additionally, mechanical properties of the titanium were experimentally determined.

The remainder of this thesis is divided into six chapters. Chapter 2 provides the motivation and historical background information relevant to this research and these systems. Chapter 3 describes the constituent materials used in the HTCL and the fabrication of the laminate system. The titanium alloy is covered with respect to its composition, microstructure, and manufacturing processes, as well as detailing the geometry of the test specimens. The fiber reinforced polymer matrix prepreg used in this hybrid composite system is also described. Chapter 4 gives descriptions of all test equipment and experimental procedures used during testing. It also discusses the analytical tools and finite element methods used. Chapter 5 presents the results from the experimental testing, the analytical analysis, and the initial finite element work conducted. Results are summarized and discussed in Chapter 6, and the major

conclusions are listed. Chapter 7 provides recommendations for future work in this field of research.

CHAPTER 2

BACKGROUND

Hybrid Titanium Composite Laminates (HTCLs) and Fiber Metal Laminates (FMLs) in general have received increased attention as structural materials in the aerospace industry. The following chapter explains some of the motivation behind the research efforts into lightweight, high strength and stiffness materials for various aerospace applications where increased damage tolerance is a necessity. It also discusses some of the previous research and development of HTCLs and FMLs as well as the current state of this technology.

2.1 Metal Laminates

In 1967, J. Kaufman [2] showed that it was possible to improve the fracture toughness of monolithic aluminum 7075-T6 by laminating thin plies of aluminum together. In 1978, W. S. Johnson et al [3] demonstrated that by bonding thin aluminum plies together with adhesives the fatigue and crack growth resistance would be greatly improved when compared to a monolithic aluminum specimen of the same dimensions. Also Johnson [4] later showed that by adhesively laminating titanium plies an improved fracture toughness of almost 40% could be gained over an equivalent monolithic titanium plate. His work also showed a reduced through thickness crack growth rates and increased fatigue life by an order of magnitude could be achieved with the change from a plane strain condition to that of a plane stress condition as illustrated in Figure 2.1.

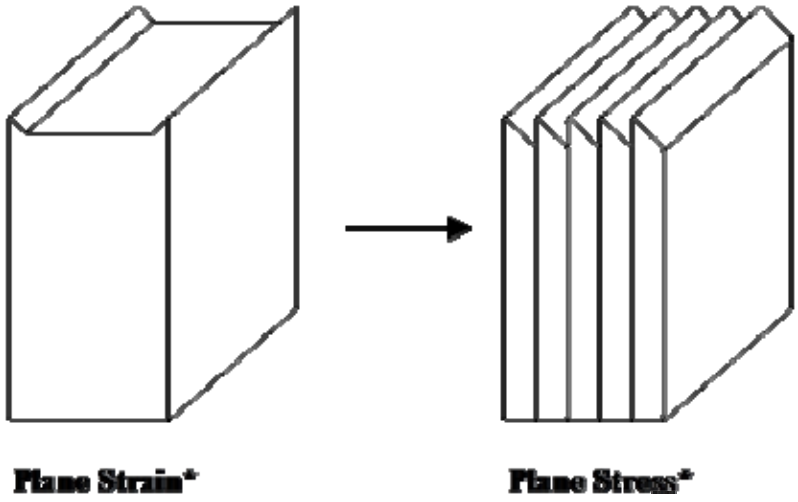

Figure 2.1 Schematic of monolithic metal specimen (plane strain) vs. a metal laminate specimen (plane stress) (ref. [5])

2.2 Fiber Metal Laminate Systems

Fiber metal laminates (FML) are a hybrid material consisting of thin, high-strength, metal sheet(s) bonded to plies of layers of fiber-reinforced epoxy adhesive as see in Figure 2.2. FML possess the advantages of both the metal and composite while not incorporating their respective disadvantages [1]. The vast majority of FML have all consistently shown improved damage tolerance that neither the metal nor fiber composite possess. This section reviews the development of FMLs and takes a broad look at the specific mechanics inherent in FML which gives them high damage tolerances and therefore make them prime candidates for fatigue driven aerospace applications.

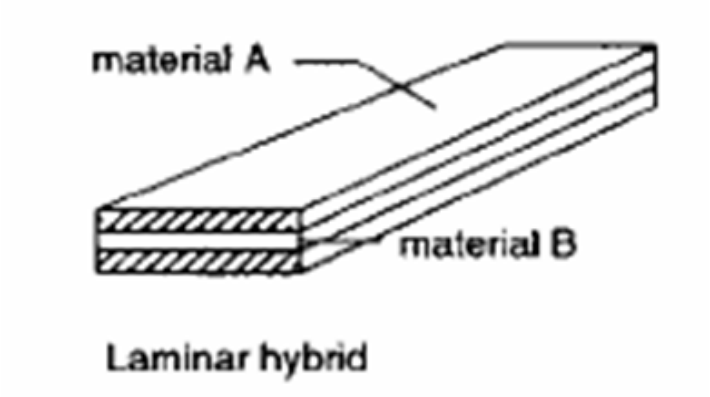

Figure 2.2 Fiber Metal Laminate (shown with material B as the metal alloy)

2.2.1 Aramid Fiber Composite/Aluminum Laminates (ARALL)

The first advancement in FMLs was made in 1978, L.B. Vogelsang [6] and colleagues at Delft developed the first fiber metal laminate called ARALL. Designed to be a high-strength and fatigue insensitive, while still retaining its light weight, ARALL was an obvious material for aerospace applications. ARALL is a laminated material of alternating thin aluminum alloy sheets with aramid-reinforced adhesive prepreg. Since the high strength-to-weight ratio of the material is inherent to the design based on the constituents, the major effort of ARALL was to combat and significantly arrest fatigue crack growth giving it optimal damage tolerance [7].

Four different types of ARALL were produced by varying the type of aluminum used (7075-T61, 2024-T3, 7475-T761, or 2024-T8). In 1983 the first production quality ARALL was being manufactured by ALCOA and significant testing steadily increased until the early 1990's when a new generation of fiber metal laminates appeared [6, 8]. The U.S. Air Force originally selected ARALL for use on the highly fatigued rear cargo door of the C-17 cargo aircraft to reduce overall weight [9].

2.2.2 Glass Fiber Composite/Aluminum Laminates (GLARE)

The next generation of FMLs, called GLARE, was developed in 1991. A major manufacturer of fibers and chemicals known as AKZO in partnership with ALCOA (Aluminum Company of America) and Delft utilized the same theory incorporating this similar material which uses glass instead of aramid as the fiber material [10]. GLARE was initially produced in four variants. The aluminum alloys were changed between different layups and the cross ply laminae of glass at different volume percentages were used [1]. These variations in the system and the enhanced compressive properties of glass over aramid fiber, gives GLARE more loading flexibility than ARALL. Currently the majority of GLARE laminates utilize Al 2024-T3 plies layered with S2-glass fiber/epoxy composite plies [11]. GLARE is currently being utilized on approximately 400 square meters of main fuselage skin on the Airbus A380 [12] .

2.2.3 Other Aluminum Fiber Laminate System

With the early success of GLARE additional aluminum based hybrid laminates have been developed for varying intended applications. ALOR are aluminum/organoplastic composites reinforced with aramid fibers, a material with a high fracture-toughness [13]. This research led to the development of CARALL and ALLIC which combined carbon fiber-reinforced plastics with aluminum and aluminum/lithium respectively [14]. A major concern of this combination is a chemical mismatch between the carbon fiber and the aluminum. Ritchie et al. [15] conducted substantial fatigue crack growth research on ARALL which combines aluminum alloys and aramid fiber. Gutierrez and Bradshaw [16] conducted crack growth research on aluminum facesheets

of a AFML which combined aluminum layers with graphite fiber-PMC material. That showed decreased crack growth rates as the fatigue life progressed.

2.2.4 Hybrid Titanium Composite Laminates (HTCL)

The first Hybrid Titanium Composite Laminate (HTCL), as seen in Figure 2.3, took the concept of fiber metal laminates and applied it to the high-temperature regime of supersonic flight [17]. The high temperatures found in supersonic flight require the use of titanium rather than aluminum. The initial analysis of the HTCL laminates was conducted by Miller et al. [17] at NASA Langley Research. They demonstrated that HTCL exceeded monolithic titanium in strength, stiffness, and damage tolerance using 6 layers of Ti-6Al-4V titanium and 5 layers of graphite-reinforced PMC. HTCLs showed significant improvement in fatigue life and crack growth resistance over monolithic Ti-6Al-4V titanium at both room temperature and elevated temperatures. Miller et al. [17] observed more damage tolerance where the fatigue crack growth through the laminate thickness was initially faster in the outer titanium plies or facesheets. Then the cracks would propagate slower as the crack tip encountered an interface zone between the plies.

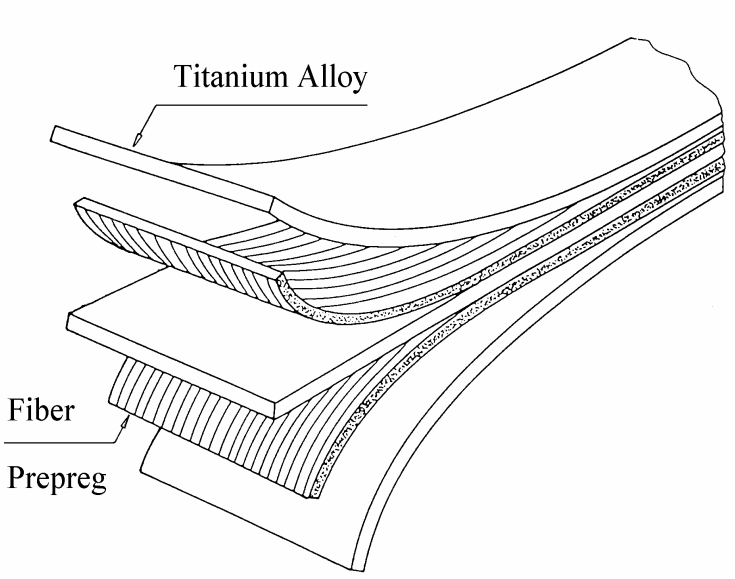

Figure 2.3 Schematic of HTCL with titanium facesheets and an embedded layer (ref. [17])

The improved damage tolerance and increased fatigue life of HTCLs determined by Miller et al. [17] were then validated by Li et al. [18]. They showed HTCLs of different compositions demonstrated an improvement in fatigue life over titanium alone using two beta-stable titanium alloys combined with a PMC layer comprised of LARC-IAX and IM7 graphite fiber. HTCLs performed even better in fatigue testing at elevated temperatures than at room temperature due to the relief of residual stresses induced in the titanium layers during processing. Li et al. [18] also discovered that delamination of the adhesively-bonded polymer matrix composite (PMC) plies from the titanium foils was occurring. Miller et al. [17]also showed that a lower interface bond strength, which leds to higher rates of delamination, can lead to an improved fatigue life in HTCLs. Verbruggen and Marrisen [7, 19] had observed debonding as a mode of failure during the testing of ARALL. Cobb and Johnson [20] conducted research on the integrity of the bonding between the titanium/PMC interface to be incorporated in a second-generation,

advanced HTCL. The FMx5 polyimide adhesive bonded with Boeing's Sol-Gel surface treatment possessed superior fracture toughness and fatigue crack growth characteristics when compared to the combination used on the initial HTCL fabrication [18, 20]. Burianek et al. [21] directly related the crack growth rate at the interface using the strain energy release rate to delamination growth in HTCLs. Rhymer and Johnson [22] then developed the advanced HTCL which modified the initial HTCL to achieve optimal strengthening of the titanium/PMC interface. The advanced HTCL did not significantly improve the materials fatigue life, but it increased damage tolerance of the titanium plies following initial damage up to 10 times as compared to the initial HTCL systems.

2.3 FML Fatigue Crack Growth

Delft University and Alcoa collected a large data base on crack growth behavior in FMLs during the development. A fatigue crack growth model that was developed by Marissen [19] assumes the basic observed relationship between fatigue crack growth and the stress intensity factor in monolithic aluminum could be used for ARALL. This simplistic model used two metal layers with one composite layer and he further included a resin rich layer between the aluminum/PMC layers as seen in Figure 2.4. The crack growth data was linked to the stress intensity factor with adjustments made for the effects of delamination, fiber bridging, adhesive shear deformation, specimen geometry, and residual stresses. He observed that fiber bridging is a damage mechanism for increasing fatigue crack growth resistance and that it is directly related to the amount of delamination and adhesive shear deformation [19]. Marissen [19] then created a FML

crack growth model where da/dn is dependent on both stress intensity and delamination growth parameters [19].

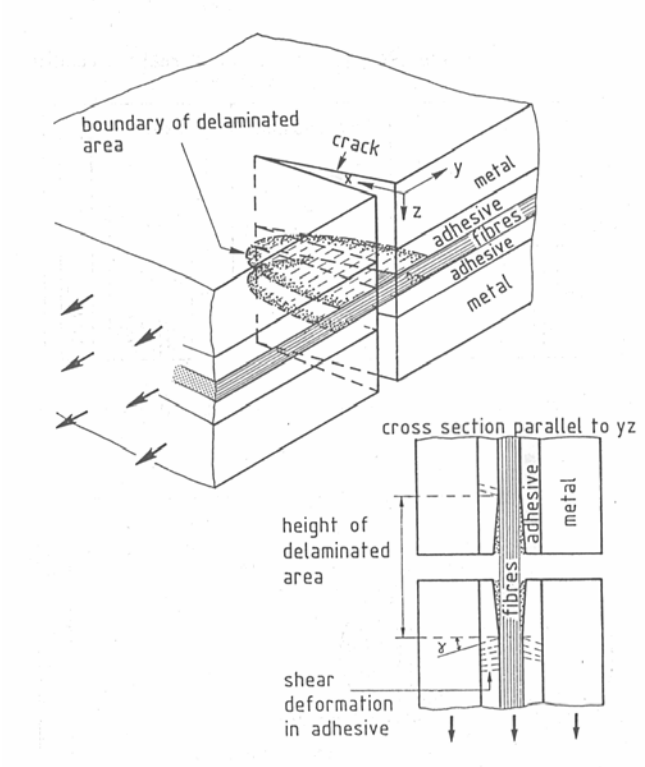

Figure 2.4 Schematic showing damage mechanisms in fiber metal laminates. Delamination with adhesive shear deformation inset (ref. [19])

2.4 Fatigue Damage Resistance Mechanism

As previously stated with the development of ARALL at Delft, significant research was conducted by Marrisen, Verbruggen, and others to characterize the damage tolerance capabilities found in FMLs. A typical damage progression in FMLs starts with a fatigue crack nucleating in the metal layer. This is then followed by debonding at the interface between the metal/PMC in the wake of the crack tip. In most cases the PMC layers stays intact and does not fail due the constituent fibers higher failure strength. It is these intact

PMC layers that bridge the crack in the metal laminate and provide increased damage tolerance for the entire FML [7].

2.4.1 Fiber Bridging

When a fatigue crack develops in the metal layer, the fiber-reinforced PMC layers remain intact in the wake of the crack tip due to load transfer through the metal/PMC adhesive interface. The assumption associated with fiber bridging is that there is a sufficient amount of 0^o fiber in the loading direction, next to the crack, to absorb the increased load without failing. Load sharing capability decreases quickly as the angle of fiber alignment to loading approaches the 90^o direction, where the matrix material is the only material supporting load. A schematic of this interaction can be seen in Figure 2.5. The fibers, which have assumed the additional load, reduce the stress intensity (K) at the metallic crack tip by retarding further crack tip opening.

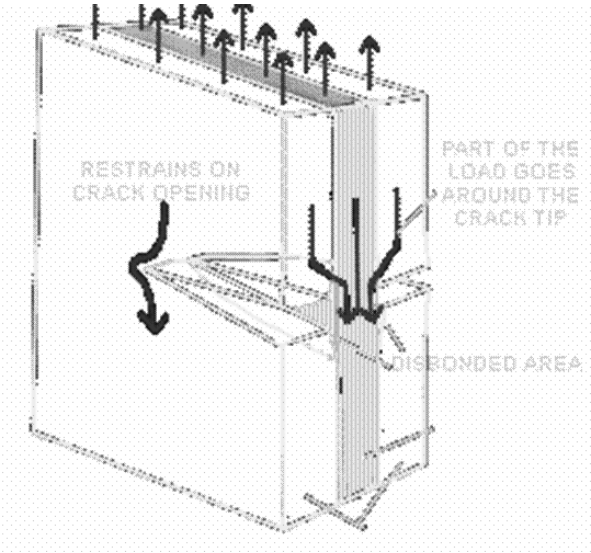

Figure 2.5 Schematic of load transfer due to fiber bridging

Ritchie et al. [15] stated that fiber bridging is an extrinsic toughening mechanism that can be designed into a material. He summarized these different mechanisms, seen in Figure 2.6, in his investigation of fiber bridging in ARALL [15]. Also known as "crack tip shielding", such toughening mechanisms have the goal of reducing the K at the crack tip by reducing the local "driving force" of the crack thereby leading to a reduced crack tip opening [15]. This mechanism allows more load to be carried in the wake of the crack tip. The fibers absorb energy that would be carried by the material ahead of the crack tip. So, instead of the entire load being concentrated ahead of the crack tip, the crack is "shielded" from this additional load by the fibers in the wake of the crack tip absorbing some of the applied energy. Marrisen showed that when high strength, fatigue resistant fibers are used to reinforce the matrix in the composite layer, and cracks initiate in the metal layer, the fibers serve as the toughening mechanism to absorb the energy given up by the metal [19]. This energy absorption is captured in the strain energy release rate [19]. This absorption of energy is what allows fiber bridging to lower the effective stress intensity factor K_{eff}. This reduced K at the crack tip ultimately leads to crack growth retardation in the metal layer [23].

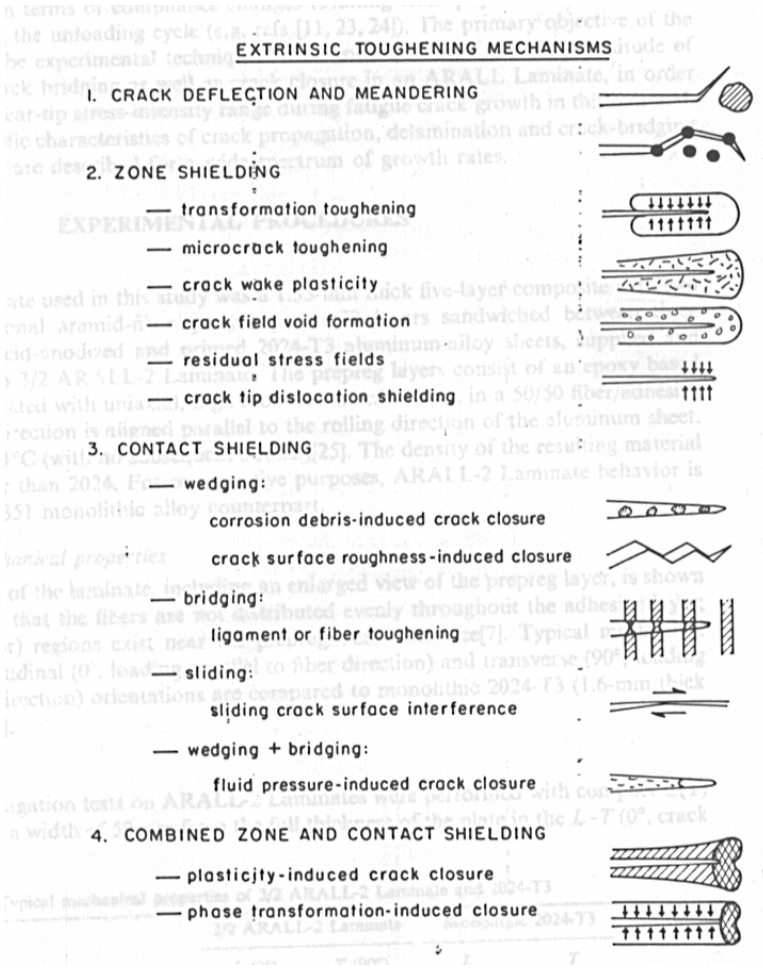

Figure 2.6 Schematics of extrinsic toughening mechanisms namely crack wake plasticity induced closure and contact shielding due to fiber bridging (ref. [15])

The generally accepted theory is that fiber bridging is the main extrinsic toughening mechanism for increasing damage tolerance among all FML systems. Some researches have stated that the major delamination mechanism occurs between the fibers and the epoxy in the PMC and not the metal/PMC interface, but they still agree on its fatigue enhancing properties [15, 24]. Bakuckas and Johnson [25] showed the desirable effects of fiber bridging in metal matrix composites. Marissen [19] has stated that it is the main mechanism for increased FML fatigue properties and controlling crack growth

rates. Marissen [19] does present one very unrealistic case where fiber bridging would be undesirable. "Perfect fiber bridging" is a theoretical situation where the combination of exact geometry, uniform intact fiber bridging, perfect bonding between layers, and an adhesive layer with infinite shear modulus, would lead to a K_{eff} at the crack tip to equal zero. The resulting stresses in the fibers at the notch root would be very high. Any fiber failure would in this condition lead to rapid and catastrophic failure. While this situation is extremely unlikely, it does reinforce the notion that the FML materials are designed to be damage tolerant or control damage, but not necessarily to stop damage from occurring.

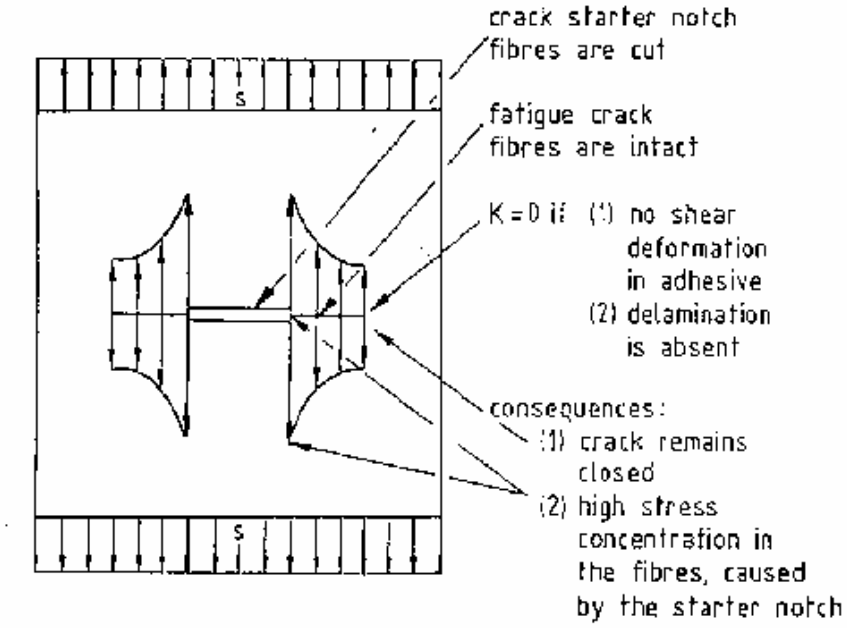

Figure 2.7 Schematic of a "perfect fiber bridging" condition (ref. [19])

2.4.2 Delamination

Miller et al. [17] showed the dependency, in HTCLs, of fiber bridging on delamination by showing that a laminate with a strong interlaminar bond had greater strength but a shorter fatigue life than one with a weaker interlaminar bond. The additional stresses assumed by the bridging fibers in the wake of the metal layer crack tip are transferred from the metal to the PMC via an adhesive bond. This bondline is located directly adjacent to the crack opening edges and is commonly called the crack flanks. Delamination occurs when the stress across the adhesive reaches a certain level as seen in Figure 2.8.

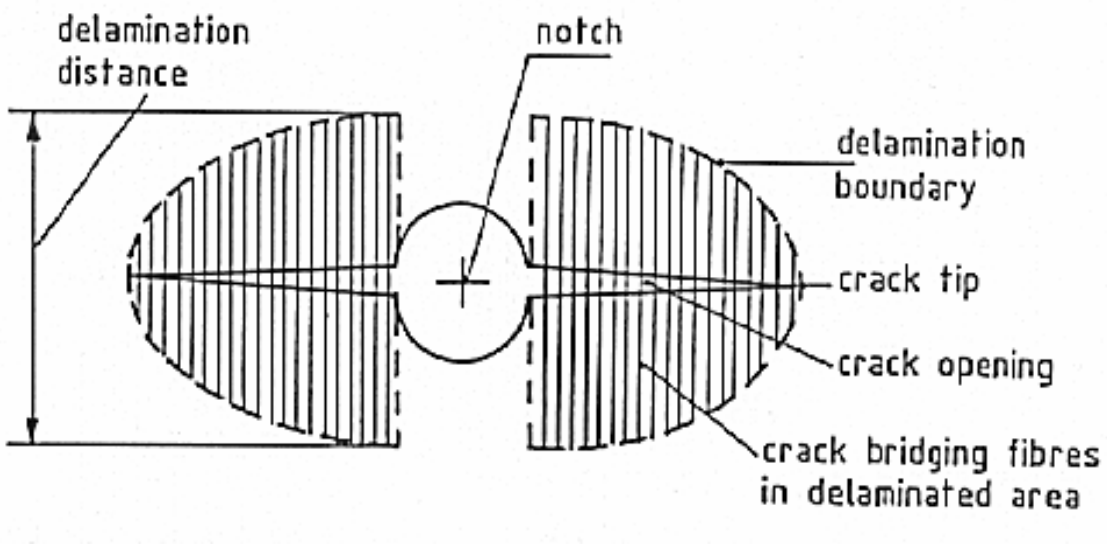

Figure 2.8 Schematic depicting an elliptical delamination region for typical fiber metal laminate with fibers bridging the crack (ref. [19])

At this point no additional load due to the cracked metal can be transferred to the fibers. Crack tip opening can and will likely occur due to lower crack bridging stresses. As the size of the delamination area increases, more crack opening and subsequent crack growth will be observed [19]. Macheret et al. [26] concluded that the delamination shape

for tension-tension tests is generally elliptical at the metal/PMC interface. Ritchie et al. [15] verified Marrisen's finding that an effective fiber bridging zone results from controlled delamination. Davidson and Austin [23] also showed better fatigue properties, at high ΔK levels, of ARALL over monolithic aluminum due to fiber bridging. Delamination will relieve some stresses in the fibers bridging the crack. A limit is needed to control the amount of delamination that is acceptable, because uncontrollable delamination would eliminate the benefits of fiber bridging. For all FMLs the preferred response to fatigue loading would be a controlled delamination, because this leads to stable crack growth. Therefore, great importance is placed on the ratio of crack length and delamination area when fiber bridging efficiency is needed for damage tolerance purposes.

2.4.3 Adhesive Shear Deformation

Another damage mechanism that occurs is the adhesive layer at the metal/PMC interface deforms due to shear stresses at the delamination boundary [19]. A schematic of shear deformation effects can be seen in Figure 2.4. This deformation could be desirable based on the shear modulus of the adhesive. If the shear stress exerted on the adhesive is lower than the shear modulus of the adhesive then this is positive, because energy is absorbed and only minor damage is imposed. If the shear stress is extremely high then massive deformation nullifies any fiber-bridging effectiveness and would be unwanted. There is a balanced medium in the amount of damage, both delamination and shear deformation, that is desirable for effective fiber bridging efficiency in a FML [17].

2.4.4 Residual Stresses

Residual stresses can be introduced into FMLs through both thermal and mechanical processes. Krishnakumar [1] determined that strain-hardening of FMLs, specifically ARALL and GLARE, will led to a higher yield strength than FMLs that have not been processed. Young et al. [10] saw increases in the fatigue life of GLARE specimens that had been subjected to overload cycles.

The differences in coefficient of thermal expansion (CTE) that occur between the adhered metal and the fiber reinforced PMC can led to residual stresses, both compressive and tensile, following cure of the laminate. Li [18] showed that HTCL specimens tested at elevated temperatures had more desirable fatigue and mechanical properties due to the relieving of residual tensile stress. Johnson and Rhymer [27] used embedded strain gages between plies of a HTCL to determine the extent of residual tensile stresses in the titanium foil that were created from the curing process. They also concluded that the residual stresses are greatly affected by the volume fraction in the laminate of the constituent materials and the associated orientation of the fiber reinforced prepreg.

CHAPTER 3

MATERIAL

The material studied in this program is a fiber metal laminate designated TiGr due to its constituent materials of titanium alloy foil and graphite fibers in an epoxy matrix. This chapter will discuss the rolled sheet titanium alloy used in the HTCL system as well as the PMC prepreg material (Carbon/Epoxy) used during hybrid metal composite consolidation at Boeing.

3.1 Constituent Material

As stated earlier, the benefit of a carefully engineered combining the two materials is that the key advantages of each constituent material may be promoted while their disadvantages are minimized. Each of the constituent materials with a short description and vital information is presented in the following sections.

3.1.1 Titanium Ti-15-3

The majority of titanium alloys require elevated temperature forming and complex processing techniques that greatly increase manufacturing costs [28]. The metastable beta (β) titanium alloy used in this research is Ti-15V-3Cr-3Sn-3Al or (Ti-15-3). The titanium alloy used in this HTCL is identical to that of the initial HTCL studies conducted by Miller, Johnson, Li, Cobb and Rhymer [17, 18, 20, 22]. Ti-15-3 is a high-strength, high temperature, and cold-formable alloy produced by TIMETAL Corporation. The cold working characteristics of this alloy are similar to those found in austenitic stainless steels [29]. The mechanical properties of titanium are more dependent on the

phases present than they are on the actual composition of the alloy. A schematic of these two phases can be seen in Figure 3.1. Substitutional elements partially replace the titanium atoms in the lattice and in this manner alter the properties. The purpose and percentages of the substitutional elements used in Ti-15-3 can be seen in Table 3.1. In actuality, the amount of any and all phases present is better governed by the heat treatment of the alloy than by atomic alteration. Most alloy additives stabilize the body centered beta phase and lower the temperature of transformation to such an extent that at room temperature the alloys are a mixture of both the hexagonal close pack alpha and beta phase.

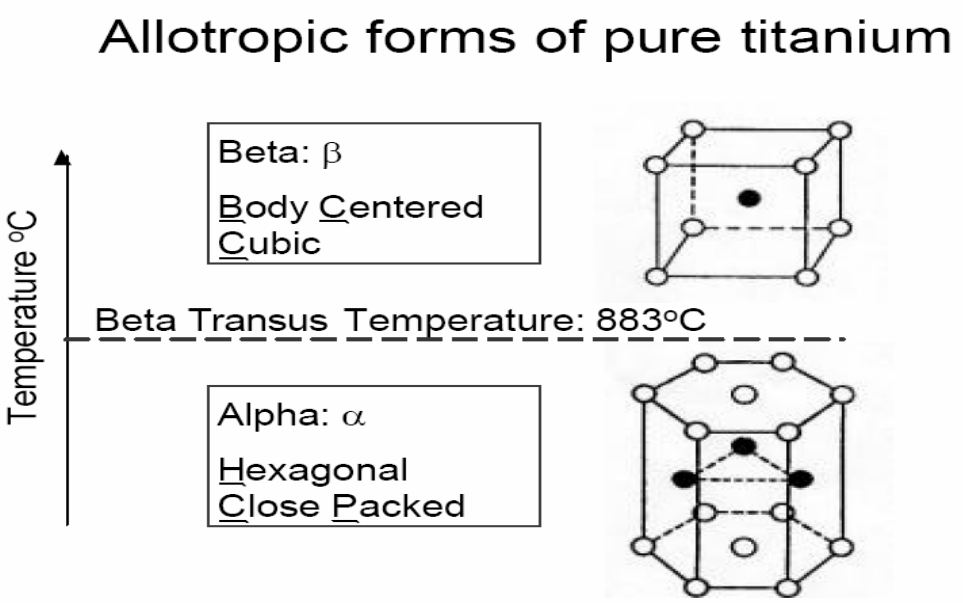

Figure 3.1 Schematic of Allotropic Forms of pure titanium (ref. [30])

Table 3.1: Substitutional elements in Ti-15-3

Alloying Element	wt %	Effect on micro structure	Effect on material
Vanadium (V)	15	β stabilizer	decrease density
Chromium (Cr)	3	β stabilizer	increase formability
Tin (Sn)	3	α stabilizer	increase aging response
Aluminum (Al)	3	α stabilizer	decrease density, increase aging response

Beta precipitate stability leads to cold formability [29]. To create this stability an all beta phase grain structure is produced, followed by a solution treatment and then aged to form finitely distributed alpha precipitates within the beta grains [29, 31, 32]. The associated beta grain refinement has been found to reduce the fracture toughness of Ti-15-3 which would led to early crack initiation [33, 34]. Ti-15-3 is used primarily for airframe applications although it has also been considered for a variety of aerospace fasteners which experience fatigue loading [28]. Nishida et al. [35] concluded that fatigue cracks initiate at the beta single phase in the beta matrix. There are two reasons for this; first, is that the strength of the beta (β) phase is lower than the alpha (α) phase and second, is the number of slip systems of β is higher than that of α [35].

The heat treatments of the Ti-15-3 used in this research are given in Table 4.1, including temperature and duration parameters for the solution treatment and aging process. The titanium heat treatment titled solution treatment, which is described in Table 4.1, were similar to the optimal heat treatment for fatigue as outlined by Nishida et al. [35]. The titanium foils were cold rolled to a final thickness of 0.178 mm (.007 in) for use in the dogbone shape tensile test specimens and HTCL fabrication.

3.1.2 PMC Prepreg

The fiber reinforced PMC, P2302-19, used in this HTCL research is also the primary material being used on the 787's primary structures [36]. Toray prepreg P2302-19, which is a combination of high-strength intermediate modulus fiber T800H and toughened epoxy resin 3900-2, qualified to the Boeing material specification BMS 8-276 for the Boeing 777 [37]. The prepreg lamina stiffness and strength properties used in this study were taken from a study conducted by Boeing [38]. These values are presented in Table 3.2. This material, used in both a unidirectional tape and woven formats, has equal design and component manufacturing performance as the original material specified for the 777, but Toray has changed the method for adding the thermoplastic toughening agent to reduce its cost. The more recent material product form is in production use on the 777 on a substitution basis [36].

Table 3.2: T800/3900-2 tape lamina properties from Boeing

Property	Value
E_{11}	142.0 GPa (20.6 msi)
E_{22}	7.79 GPa (1.13 msi)
G_{12}	3.99 GPa (0.58 msi)
υ_{12}	0.34
t_{ply}	.178 mm (7 mil)
σ_{1T}	2.48 GPa (360 ksi)
σ_{1C}	1.38 GPa (200 ksi) (initial analysis)
	2.11 GPa (306 ksi) (calibrated analysis)
σ_{2T}	33.0 MPa (4.79 ksi)
σ_{2C}	206.8 MPa (30 ksi)
τ_{12}	100.0 MPa (14.5 ksi)

CHAPTER 4

ANALYTICAL, MODELING, AND EXPERIMENTAL METHODS

The specifications and capabilities of the laboratory equipment used for the mechanical characterization of the material are presented. The experimental methods used for each phase of the mechanical testing are discussed in detail, so that replication of the testing conditions would be possible. All experimental testing was conducted at ambient room temperature. The HTCL consolidation process is discussed and the manufacturing procedure used to make the sample HTCL specimens is also described. This chapter also discusses both the 2-D laminate code developed in MATLAB that was used for the analytical modeling portion of this research as well as the 3-D finite element code, ANSYS, used for finite element modeling.

4.1 Experimental Equipment and Procedures

A variety of laboratory equipment was necessary to conduct mechanical characterization studies of the Ti-15-3 rolled sheet material and HTCLs in this program. The following sections discuss the equipment used for both imaging and mechanical testing as well as the procedures implemented.

4.1.1 Ti Foil

The titanium foil in this study shall represent four different heat treatments that result in titanium foil with four increasing levels of strength (decreasing levels of elongation). Titanium foil properties were determined via dog-bone coupons for the four heat treatment conditions.

4.1.1.1 Specimen Preparation

The titanium foil specimens were removed from the aluminum shipping brackets and then adhered to cardboard backer plates to restrict curvature. The titanium foils used in this study were of the dogbone configuration as see in Figure 4.1. The specimens have an average gage thickness value of .178 mm (7mil). The edges of the dogbone coupons were lightly buffed with 500 grit silicon carbide (SiC) paper to remove any machine scratches, notches, or defects that could create a stress concentration. Measurements of the average gage length, gage width, grip length and overall length were recorded.

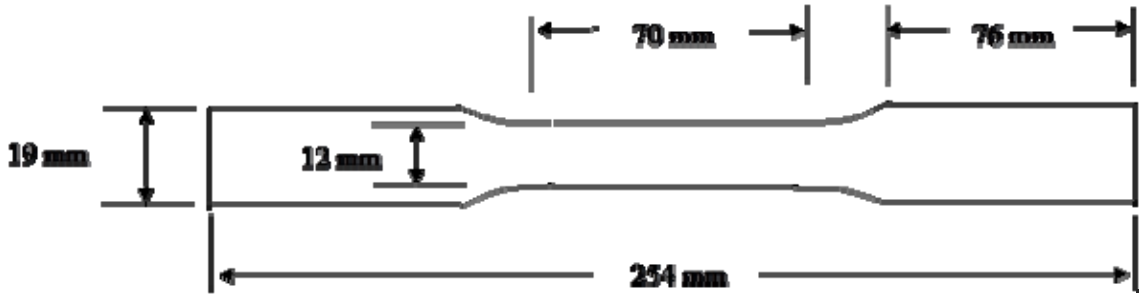

Figure 4.1 Schematic of titanium alloy dogbone specimen with measurements in mm.

All the Timetal β Ti-15-3 foil received by Boeing had been aged at 1050° F for 6 hours. The foils were then further heat treated to differing levels of material temper can be seen in Table 4.1.

Table 4.1: Ti foil heat treatment

Coil #	HT Designation	Temperature	Time	Cooling	Spec
KOB-6-12-055	STA 1025F	1025F +/- 10	8 hours	Vacuum down to 600F	BAC process
KOB-6-12-055	STA 1100F	1100F +/-10	8 hours	Vacuum down to 600F	BAC process
KOB-6-12-055	Solution Treat	1450F +25/-0	10 min	Rapid Argon Cool to 600F	BAC process

4.1.1.2 Ti-15-3 Foil Strain Gaging

Strain gages were bonded to each of the dogbone foil specimens to collect experimental data from the tensile tests. Strain gages (CEA-06-125UT-350) with a 5% strain limit were used for this test. Standard 350 ohm bi-axial strain gages were selected to collect both axial and transverse readings simultaneously. Strain gages were bonded using M-Bond 200 standard adhesive and the recommended preparation procedure outlined in Vishay Corporation strain gauging tutorial. Four strand strain gage wire (30-AWG), bondable terminals (CPF-50C), and silver-tin solder (M-Line 361A) were utilized for this application. The strain gage setup can be seen in Figure 4.2.

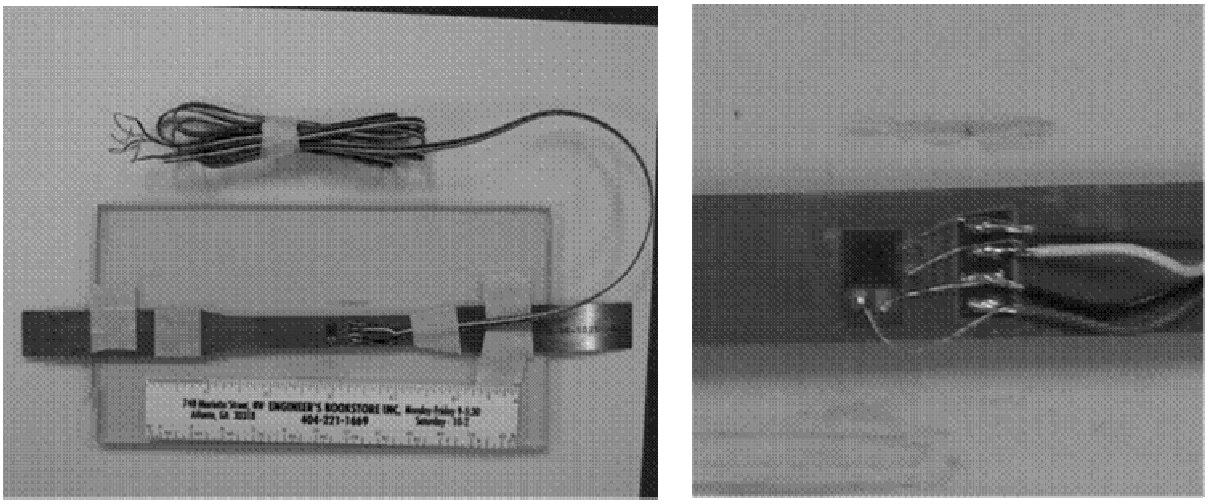

Figure 4.2 Ti foil dogbone coupon with strain gage and lead wires (left) and close up of strain gage (right)

4.1.1.3 Titanium Foil Test Frame

Initially, the titanium foils were tested in a MTI screw driven test frame with a 10 metric ton (22 kip) load cell as seen in Figure 4.3 to obtain modulus data. A Phoenix computer test control/data acquisition system was used to control testing and gather required data. The specimens were aligned and inserted into the mechanical friction grips. Great care was taken to ensure proper alignment of the specimen in the direction of loading. The strain gage wires were then attached to a strain gage amplifier. The mechanical properties of the titanium foils, at room temperature, were determined by tensile tests to failure. To determine the effect of titanium foil heat treatment on elastic modulus and Poisson's ratio, a series of three tension test measurements for properties were made over the range from 25% to 75% of the calculated elastic limit were conducted under displacement control at a rate of 1.27 mm (.05 in) per minute.

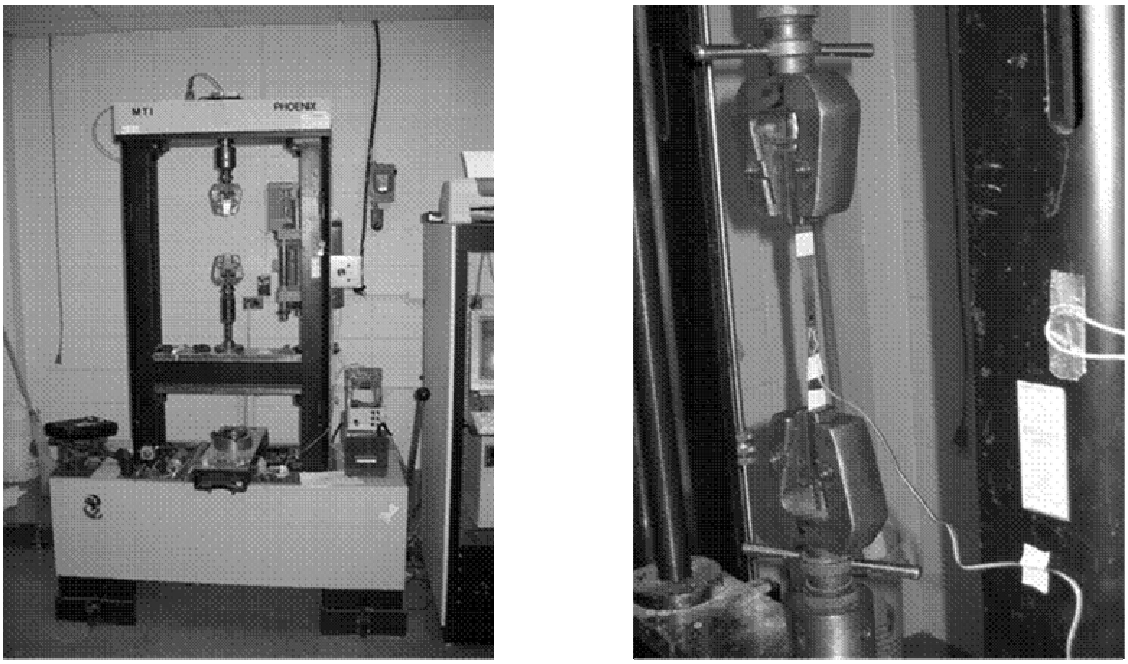

Figure 4.3 MTI Screw Drive with Ti foil in mechanical grips (left) and close up view of foil (right)

Upon further discussion with Boeing the specimens were then pulled to failure to gather strain to failure data. This was completed using the SATEC CATS system 20 kip servo hydraulic test frame outfitted with servo hydraulic grips. SURFALLOY surfaced (2 in) grips with centering guides were used to ensure proper gripping of the specimen without creating stress concentrations that could cause failure outside the gage section. Literature had stated that the expected elongation values of the Ti-15-3 would exceed the limitations of the bonded strain gages [28]. A MTS extensometer model 634.11E-25 (serial number 0349824) with a 25.4 mm (1 in) gage length was employed. The extensometer was mounted, and centered, to the face of the specimen using rubber bands as seen in Figure 4.4. In order to prevent slippage of the knife edge points on the foil surface, 3M double sided tape was place beneath each point. The specimen was then

tested under displacement control at a rate of 1.27 mm (.05 in) per minute until ultimate failure.

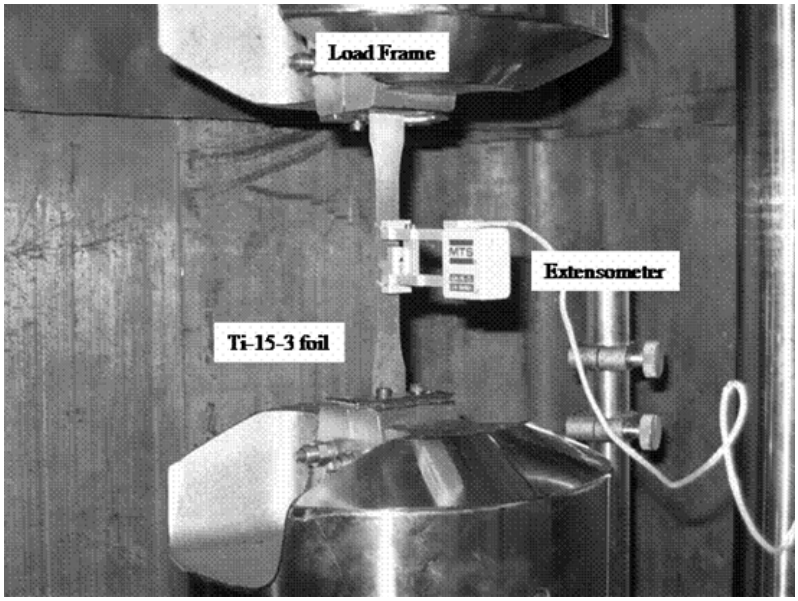

Figure 4.4 Image of Ti-15-3 foil test with extensometer

4.1.1.4 Microstructure Imaging of Ti-15-3

The following method was used primarily by undergraduate research assistant, Julie Duyree, School of Material Science and Engineering, Georgia Institute of Technology, to obtain microstructural information about the effect of the four heat treatments, listed in Table 4.1, on Ti-15-3. A sample of each temper of Ti-15-3 was cut using a Buehler Isomet 4000 linear precision saw to form approximately 2 cm^2 of surface are for mounting and polishing. The samples were then mounted in epoxy for handling during subsequent phases of this process.

The Ti-15-3 foil specimens that were tempered with a STA 1025 heat treatment, STA 1100 heat treatment and the solution treatment (designated 1025, 1100, and ST

respectively) were polished on the Struers Rotopol-2 with 500 grit silicon carbide abrasive paper. Next a Beuhler Ecomet 6 variable speed grinder-polisher was utilized to coarse polish with 1200 grit silicon carbide paper. Subsequent levels of polish were 9 μm diamond solution and a 1 μm alumina solution. Upon inspection further polishing was required. The process was repeated using the following levels: 500 grit silicon carbide paper, 1200 grit silicon carbide paper, 6 μm diamond solution and 1 μm alumina solution.

The as received specimen (designated AR) was first coarse polished with 500 grit silicon carbide paper. Then subsequent levels were 1200 grit silicon carbide paper, 6 μm diamond solution, and then 1 μm alumina solution. This specimen was hand polished due to an incorrectly used mold which could not be placed in the automatic polisher.

The polished specimens were then etched for imaging purposes. The etchant, Kroll's Reagent, was made by adding the following ingredients to a 250 mL Ehrlenmeyer flask under a wash down fume hood:

125 mL water

0.5 mL hydrofluoric acid

0.75 ml nitric acid

Each specimen was exposed to the etchant for 15 seconds, with the exception of the SN specimen which required three 15 second etching applications for a total of 45 seconds. The specimens were then rinsed with water and air dried.

Imaging of the microstructures was completed with a Leica optical microscope with a mounted digital camera. Each specimen was imaged at 100x, 200x, and 500x

magnification. The images were processed with ImagePro software to obtain the structure, grain size, and precipitates present in the Ti-15-3.

4.1.1.5 Ti-15-3 Foil Test Matrix

The testing conducted for this portion of the research was to determine how the four unique heat treatments of the Ti-15-3 foil affected the tensile material properties. These properties will be applied to both analytical and finite element analysis codes that will be used to gage the eventual performance of the HTCL specimens. The tensile test matrix is represented by Table 4.2.

Table 4.2: Tensile test matrix for Ti-15-3 foil

Titanium Alloy (condition)	Specimen Type	# of Specimens
7 mil Ti-15-3 (as rec.)	dogbone	4
7 mil Ti-15-3 (STA 1025 heat treatment)	dogbone	4
7 mil Ti-15-3 (STA 1100 heat treatment)	dogbone	4
7 mil Ti-15-3 (solution treatment)	dogbone	6

4.1.2 HTCL Fatigue Testing

Open-hole HTCL also known as Titanium Graphite fiber laminates (TiGr) coupons were tested in constant amplitude fatigue cycles to determine the initial reliably detectible crack and crack growth characteristics. Three stress load levels were used to determine a crack length (a) versus number of fatigue cycles (N) curve for the purpose of characterizing fatigue damage. Crack growth rates were determined once the initiated crack was determined.

4.1.2.1 Specimen Preparation

The HTCL coupons studied in this research phase were manufactured at Boeing using the constituent materials outline in chapter 3. The only laminate variable was the embedded titanium foil with four varying heat treatments tabulated in Table 4.1. The HTCL laminate contained the following ply sequence: [45/0/-45/0/Ti/0/-45/0/45] as seen in Figure 4.5 and tabulated in Table 4.3. Each ply has a uniform thickness of 0.178 mm (0.007 in).

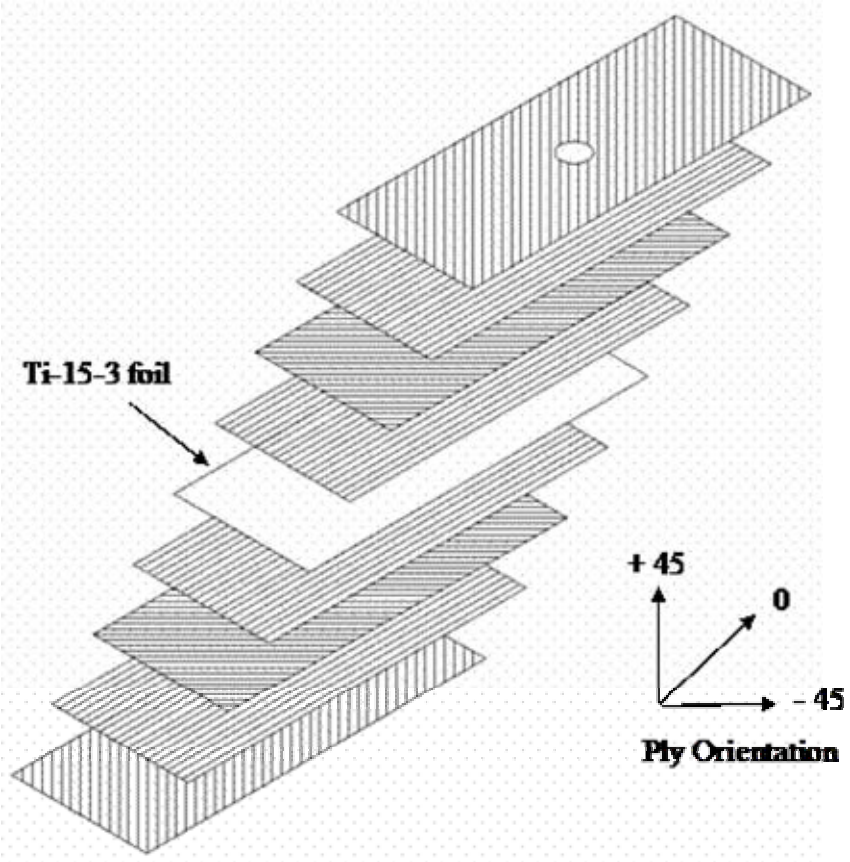

Figure 4.5 Schematic of HTCL layup (ref. [39])

Table 4.3: HTCL Specimen Lay-up of Material and Orientation

Ply #	Material	Orientation
1	PMC prepreg	45
2	PMC prepreg	0
3	PMC prepreg	-45
4	PMC prepreg	0
5	Ti-15-3 foil	L
6	PMC prepreg	0
7	PMC prepreg	-45
8	PMC prepreg	0
9	PMC prepreg	45

The surface treatment and primer used on embedded Ti-15-3 prior to consolidation is the Boeing Sol-Gel batch process surface treatment of titanium foil for use in TiGr laminates designated B-KC00-BWS-M2001-0216. The autoclave process used to cure the HTCL was in accordance with Boeing standard BAC5578 (Type IV, Full Vacuum, .586 MPa (85 psi) (per PSD 6-51, Grade B). The resulting HTCL panels had an average uniform thickness of 1.75 mm (.069 in) and did not appear to have an fabrication defects such as voids, resin rich areas, delamination or uneven fiber distribution. Figure 4.6 shows the post cured laminates through width profile.

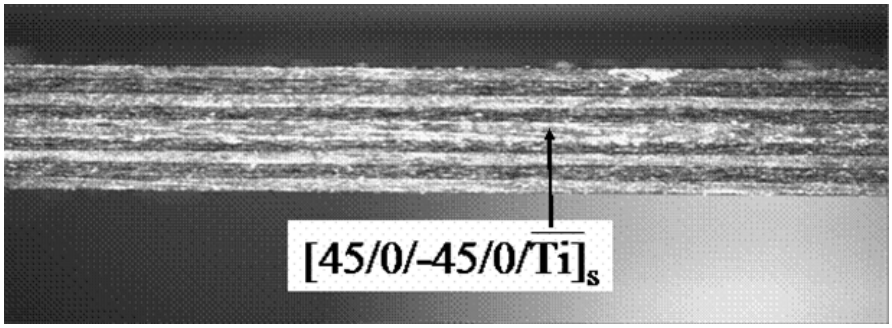

Figure 4.6 Image through the width of HTCL prior to fatigue testing

The balanced, symmetric HTCL panel was then cut into open hole straight sided coupons with dimensions 33 mm (1.5 in) wide x 305 mm (12 in) long with a 6.35 mm (.25 in) diameter center hole as seen in Figure 4.7 and Figure 4.8. The center holes were machined drilled.

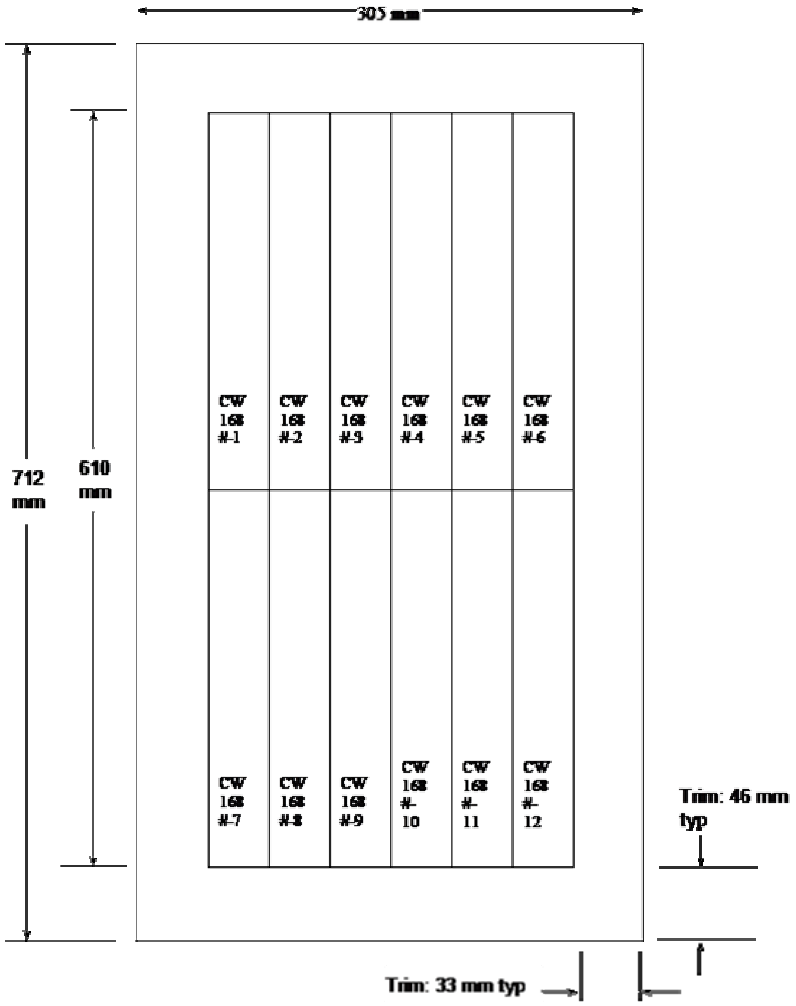

Figure 4.7 Seam and specimen diagram (Boeing Co.)

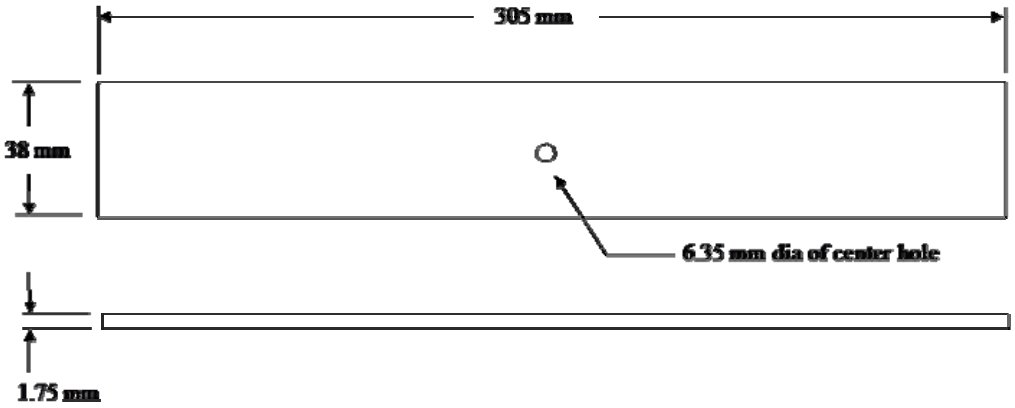

Figure 4.8 HTCL coupon description (Boeing Co.)

4.1.2.2 Constant Amplitude Fatigue Testing

All constant amplitude fatigue testing was conducted in tension-tension loading at a frequency of 10 Hz and a stress ratio of R=0.1. Testing was conducted in a sinusoidal cyclic waveform under load control with a SATEC CATS system 88.9 kN (20 kip) servo hydraulic test frame outfitted with servo hydraulic grips. SURFALLOY surfaced 46 mm (2 in) grips with centering guides were used to ensure proper gripping of the specimen while not creating damage to the exterior carbon epoxy plies. The system utilizes a MTS TestStar II data acquisition/controller system. Using basic testware in the MTS TestStar II data acquisition/controller system the fatigue loading specifications and preset cycle counter were controlled. Prior to testing the test frame was overhauled and modified to meet the specifications for the unique test procedure. The load cell was calibrated prior to the initiation of testing. Each of the HTCL specimen edges and open hole were polished with 500 grit (20 μm) silicon carbide paper to remove any defects that may lead to early crack initiation in the Ti ply.

Initial attempts to visually detect cracks in the Ti ply proved difficult due to the lead shielding box required for crack characterization after initial detection via radiography. For this reason it was decided to use plastic crack replicating tape at predetermined intervals to establish this initial reliably detectible crack. The procedure to replicate cracks calls for the fatigue cycle to be interrupted with 75 % of the maximum applied tensile load placed on the coupon to create crack opening. The cellulose acetate tape was placed in the interior of the center hole and acetone was applied liberally. Immediately a rubber eraser was used to force the tape into any crack that maybe present and held for 30-45 seconds until the tape hardened. It was then removed and placed on a microscope slide for viewing. If a crack was indicated the radiographic inspection was initiated.

4.1.2.3 Radiographic Crack Growth Inspection

The cyclic fatigue tests were performed using the previously mentioned SATEC CATS system 88.9 kN (20 kip) servo hydraulic test frame outfitted with a lead lined wooden enclosure for radiation safety as seen in Figure 4.9. All radiography was conducted in an x-ray safe room which would meet the safety requirements of the Georgia Tech Office of Radiation Safety (GT ORS) which met the minimum state and federal safety requirements.

The shielding box was constructed from 19.05 mm (0.75 in) plywood lined with 3.18 mm (0.125 in) lead. The box had to be modified to work with servo hydraulic grips.

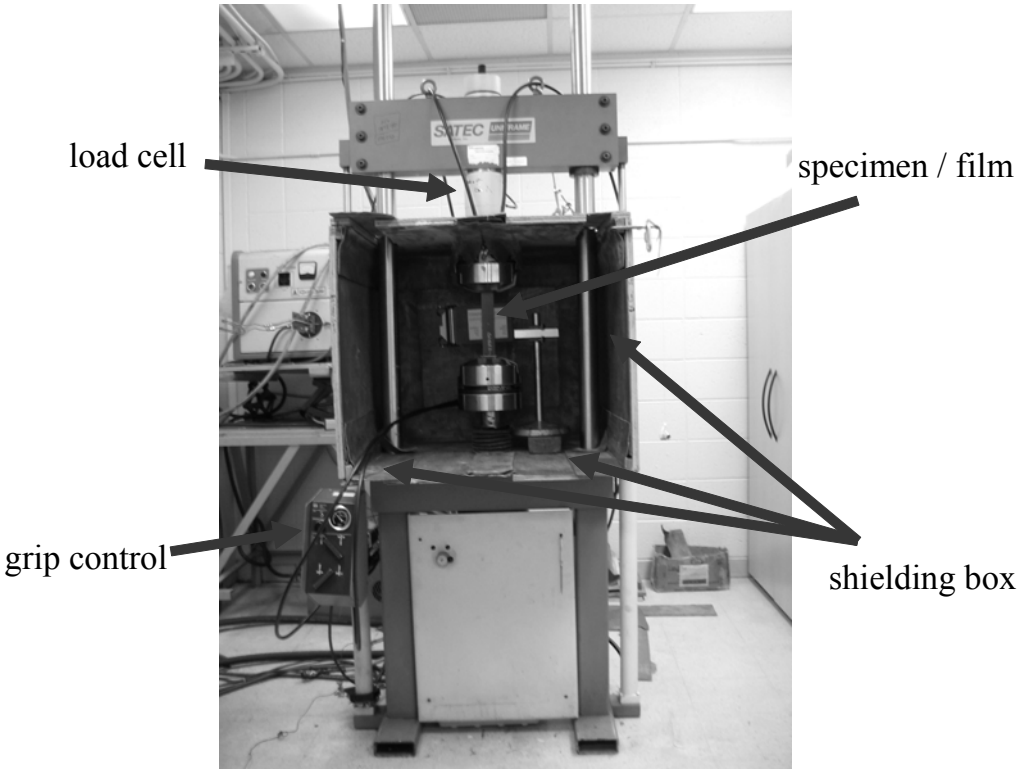

Figure 4.9 SATEC Fatigue Test Frame without x-ray unit in position

As previously mentioned, when a crack was detected via replicate x-ray images were taken. The coupon was kept under 50-75% of the maximum applied fatigue load. The film and film holder were positioned directly behind the center of the open hole in the HTCL specimen as seen in Figure 4.10.

Figure 4.10 HTCL Specimen with Film Setup

The portable tungsten x-ray tube in its enclosure was aligned with the center of the HTCL coupons and moved into position (seen in Figure 4.11) to engage the riser arm safety interlock. This position was cross referenced with aligning marks on the floor and visual cues on the shielding box.

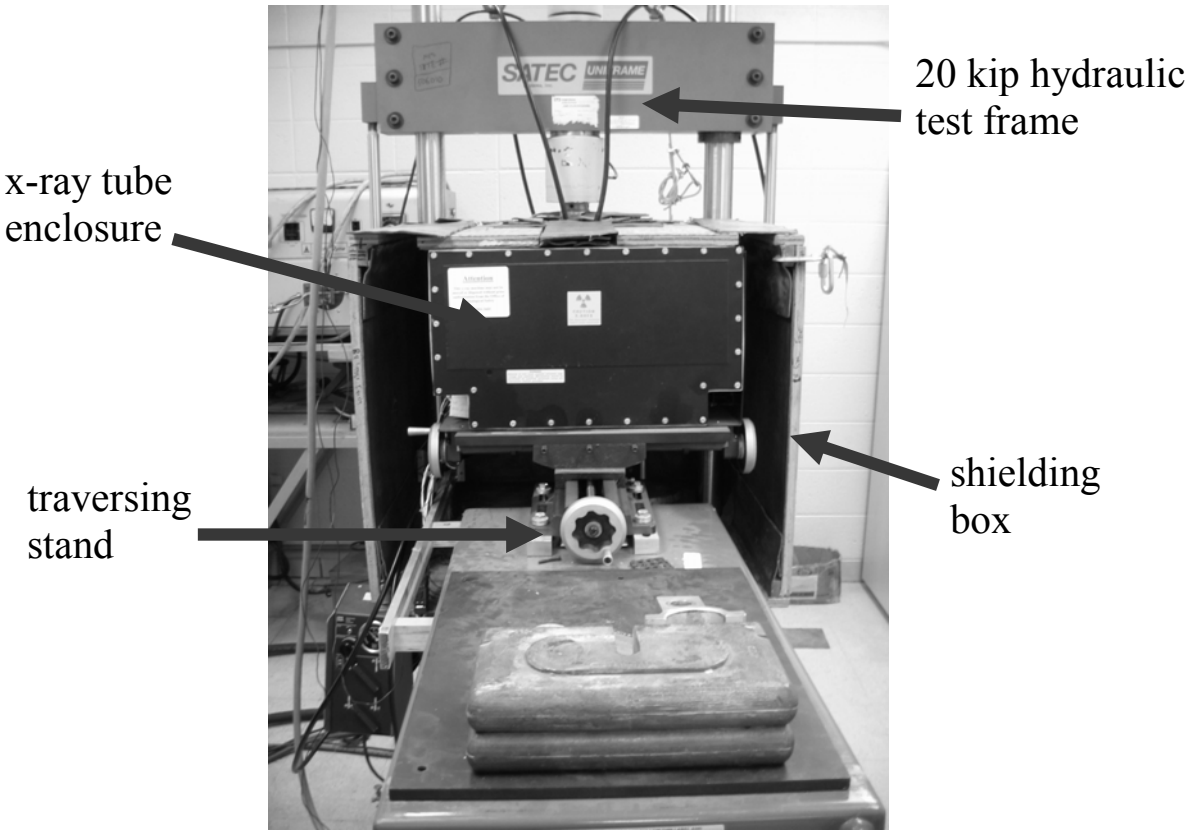

Figure 4.11 Test Frame with X-ray Unit in position

The setting for the Faxitron 110 kV x-ray unit was set at voltage 35 kV, current 1 mA, and a time of 90 seconds were dialed into the control panel. Once the system was energized the room was evacuated and the door was closed closing the final interlock. The specimen was then irradiated to acquire the image of the embedded Ti ply. A schematic of the x-ray focal area and the basic coupon film setup can be seen in Figure 4.12. The image would then be processed in accordance with 4.1.2.5.

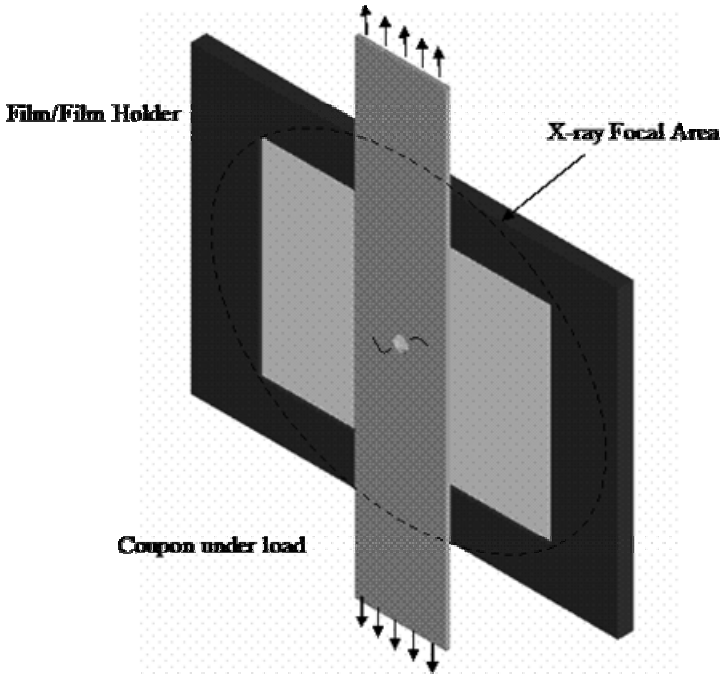

Figure 4.12 Schematic of Specimen and Film/Film Holder (ref. [39])

4.1.2.4 Radiographic Delamination Inspection

The following is a summary of the procedures, materials used and observations made in the course of conducting non destructive evaluation for damage mechanisms other than fatigue cracking. Prior to testing it was necessary to fabricate a batch of Zinc Iodide based liquid dye penetrant, which through seeping by capillary action into cracks, delaminations and other types of damage, provided contrast between those damaged areas and the fiber metal laminate constituent materials [40]. The penetrant mixture was made by adding the following four ingredients to a 125 mL Ehrlenmeyer flask and dissolving into the following solution:

60 g. Zinc Iodide (ZnI_2) 98% pure

8 mL distilled water

10 mL Isopropyl alchol

3 mL Kodak photo flow 200

Once the specimen was properly inserted into the test frame pieces of clear packing tape were placed over the open hole on the front and back side of the specimen. The penetrant was applied into the hole using a 250 μL Hamilton luer tip syringe. The hole was then filled to over ½ the volume. Care was taken to prevent excess penetrant from contaminating the exterior ply surfaces which would lead to a false image.

A load equal to the half maximum cyclic stress was applied. The penetrant was allowed to soak in for approximately 20 minutes to ensure full penetration of the damaged area. The specimen was then removed, rotated 180° and re-inserted into the test frame. The specimen was inspected to ensure that there was proper penetrant level in the hole and no leakage. The specimen was again allowed to soak for 20 minutes. The syringe was then reinserted into the hole to remove any excess penetrant. The tape was removed and the exterior surface was wiped clean with acetone. The Polaroid type 55 P/N film and its holder were placed behind the specimen as described in section 4.1.2.3. The x-ray tubehead was then positioned as described in section 4.1.2.3. The tube voltage, current and exposure time were set to 90kV, 2mA and 90 seconds. These parameters were earlier determined by trial and error to provide the best combination of contrast and image quality. The specimen was then x-rayed under load. The positive was then examined to determined proper exposure and the corresponding negative was then processed as described in section 4.1.2.5. Both positive and negative were then labeled.

4.1.2.5 Film processing and Imaging

Upon completion of the irradiation of the Polaroid Type 55 PN sheet film the Kodak type 545i film holder was shifted from load to process. The film was then pulled from the film holder to spread the developing agent on both the positive and negative images. This film was allowed to sit for approximately 20-30 seconds depending on the room temperature. The sheet film was then opened to separate the positive image from the negative. If the positive image showed excellent image quality and contrast, the negative image would be placed in a fixing agent. For this research the fixing solution was an 18% sodium sulfite solution that was made using anhydrous sodium sulfite from Kodak. The negative is kept in fixing solution for 30-90 minutes depending on the age of the solution. Next the negative was rinsed in warm tap water for 20 minutes to clear all developing and fixing agents. Finally the negative was air dried.

The negative could next be inspected with a Leica stereographic microscope to observe any damage occurring in the embedded Ti layer. Once damage was observed a digital image was taken and further analyzed using the ImagePro Express software.

4.1.2.6 Embedded Crack Measurement Validation Process

Prior to full scale testing in accordance with the pre-determined test matrix a specimen was cycled until cracks were visually detected by inspection and by crack replication process. An as received HTCL specimen was cycled at 289.6 MPa (42 ksi) until cracks were discovered with the use of replicates at 24,000 cycles. The specimen was then x-rayed at various voltage levels, current setting and exposure times until an optimal contrast was generated. Numerous images were taken and the negatives were analyzed under a Leica stereographic microscope using Image Pro Express software

where crack measurements were taken. The 50.8 mm (2 in) center section of the specimen was removed using a water cooled abrasive saw (see Figure 4.13).

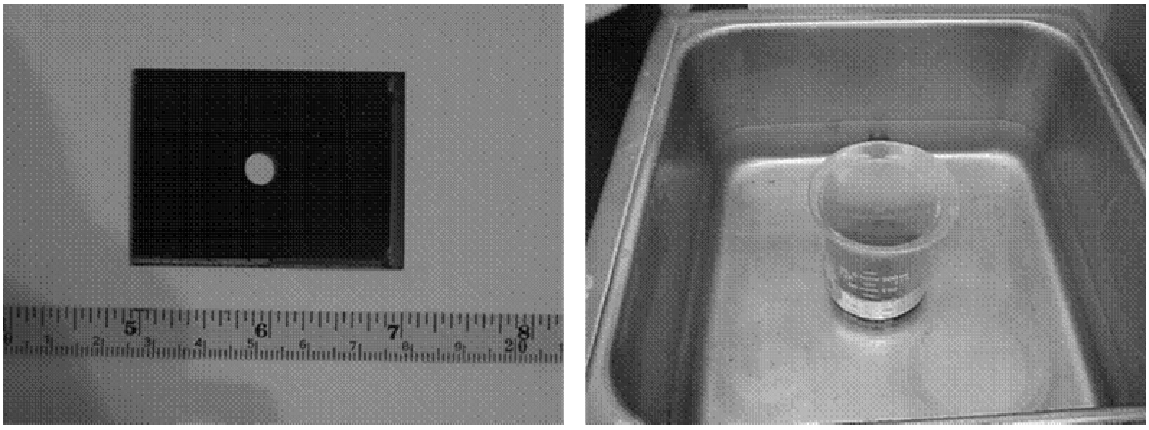

Figure 4.13 Center section of specimen used for crack validation (left) and during matrix digestion process (right)

The cracked Ti-15-3 foil was then separated from the fiber reinforced PMC through a nitric acid solution based matrix digestion process as outlined in ASTM standard D 3171 – 99 annex A1 procedure A at Applied Technical Services.

4.1.2.7 Thermoelastic Stress Analysis Technique (TSA)

The following is a summary of the procedures, materials used and observations made in the course of conducting non destructive evaluation for damage mechanisms other than fatigue cracking in cooperation with Dr. Rami Haj-Ali's, Georgia Institute of Technology, College of Civil Engineering, research team graduate students specifically Shane Johnson, Hoan Kee Kim, and Bo-Siou Wei. Two HTCL specimens, one previously fatigue damaged and one with no fatigue damage, were selected to provide data on delamination area and crack growth characteristics.

The experimental procedure used was modeled closely from the work of El-Hajjar [41]. The thermal measurements were acquired with a Delta Therm DT 1500

thermoelasticity measurement system which uses a liquid nitrogen cooled infrared camera. The TSA system operates by recording the temperature change of the specimen under fatigue loading as seen in Figure 4.14 [42]. A focal plane array in the IR camera is employed to detect the incident radiant energy emitted from the specimen's surface during testing and convert it to an electrical signal [42]. The software in the system coordinates a reference signal from the test frame load cell to ensure that only true temperature changes are monitored [41, 42]. Hundreds of cycles are collected and averaged to improve the signal to noise ratio. In order to properly track stress states in the material, strain gages or other means should be used to correlate the received IR information to a known stress value [41, 42].

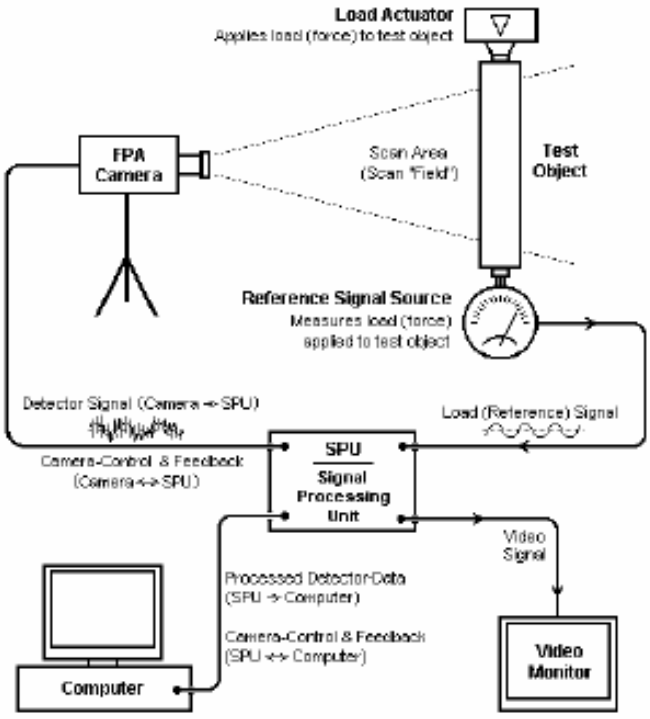

Figure 4.14 Schematic diagram of TSA system (ref. [42])

The goal of this investigation was to determine if the subsurface damage mechanisms in the embedded Ti ply would be detectable at the surface of the coupon. The test frame employed for these tests was a MTS 810 servo hydraulic test system 22.5 kN (55 kip) with 76 mm (3 in) SURFALLOY grips. The HTCL coupons had to be tabbed prior to testing in order to conform with the larger grips. Also, a thin coat of Krylon Ultra Flat black paint was applied to the surface of the HTCL coupon to cut down on environmental noise and improve surface emissivity (Figure 4.15). The specimen was then centered in the grips to eliminate off axis loading and the testing was initiated (Figure 4.16).

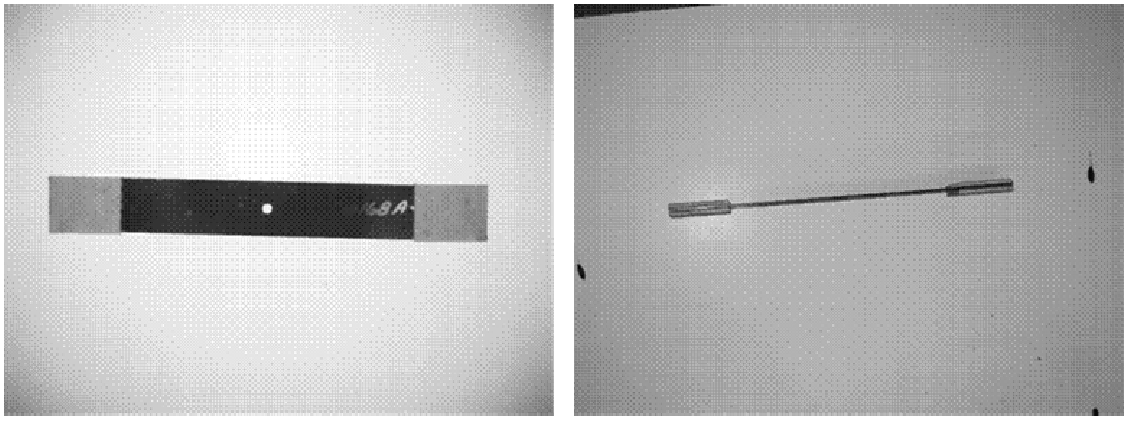

Figure 4.15 HTCL coupon prepared for Thermoelastic Stress Analysis (right and left)

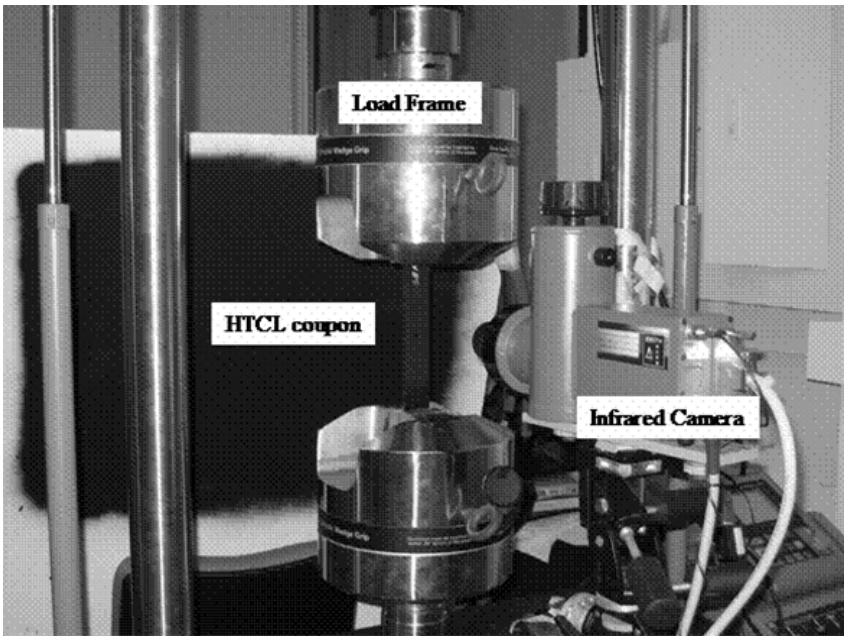

Figure 4.16 TSA infrared camera setup used for HTCL analysis

Following the TSA evaluation of a previously damaged specimen a destructive evaluation was preformed to correlate delamination and identify other damage present through the width adjacent to the open hole. Using a water cooled abrasive saw, the center section of the coupon near the hole was systematically sectioned for visual inspection. Sections at 2mm and 4mm from the hole were produced as seen in Figure 4.17. The resulting surfaces were visually inspected using the Leica microscope.

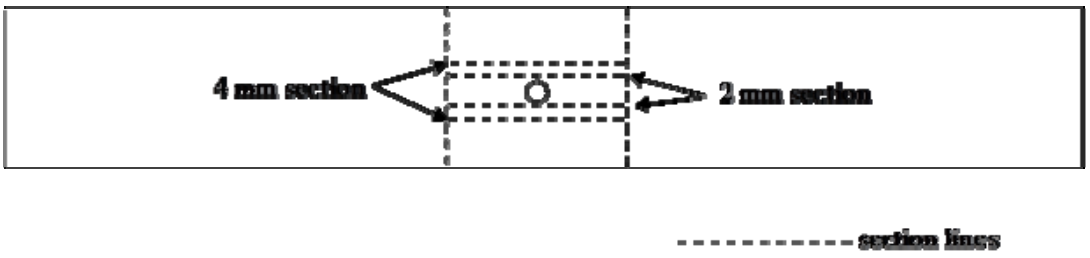

Figure 4.17 Schematic of center sectioning of HTCL coupon

4.1.2.8 HTCL Test Matrix

The testing conducted for this portion of the research was to determine how the four unique heat treatments of the constituent Ti-15-3 foil affected the mechanical response and fatigue properties of the HTCL coupon. As previously stated a number of procedures were implemented to measure the damage mechanism occurring in the HTCL specimens. The HTCL fatigue test matrix is represented by Table 4.4.

Table 4.4: Constant amplitude fatigue test matrix for HTCL coupon with stress ratio of R=0.1

Applied Stress MPa (ksi)	HTCL (as received)	HTCL (STA 1025 HT)	HTCL (STA 1100 HT)	HTCL (Solution HT)
206.8 (30)	2	2	2	2
172.4 (25)	2	2	2	2
158.6 (23)	1	1	1	1
137.9 (20)	1	1	1	1

4.2 Analytical

An analytical analysis was conducted to understand the stresses that will be imparted on the embedded titanium ply near the open hole, which includes calculation of stress concentration factors (SCF). This information was then used to determine initial loading conditions for use in the fatigue tests. The HTCL coupon was a balanced, symmetric laminate that has orthotropic properties, where the material properties vary with loading direction. The combined stress state for orthotropic materials must be

determined, because they, unlike isotropic metals, do not fail strictly due to the maximum failure stress [43]. Therefore, the use of classical lamination techniques was employed in this analysis to determine stress concentration factors for the embedded plies.

4.2.1 Classical Lamination Theory (CLT)

The embedded Ti ply stress values were calculated using a combination of MATLAB codes created primarily by Paul Treasurer, Graduate Research Assistant, Georgia Institute of Technology. The first MATLAB code implemented classical laminate theory equations to determine coupling coefficients based on material properties and geometry of the laminate. The second MATLAB code utilized the found coefficient values and applied loads to determine the overall laminate strain value. These strain values were then used to determine stresses in the embedded Ti ply.

The force-strain response laminate equation (4.5) is the basis for the CLT analysis. The coupling matrices, A, B and D, are directly related to the layup of the laminate and the material properties of the individual layers.

$$\begin{bmatrix} N \\ M \end{bmatrix} = \begin{Bmatrix} A & B \\ B & D \end{Bmatrix} * \begin{bmatrix} \varepsilon \\ \kappa \end{bmatrix} \tag{4.1}$$

where N= applied axial load matrix

M= applied moment matrix

A= extension stiffness matrix

B= extension bending coupling matrix

D= bending stiffness matrix

ε= laminate strain matrix

κ= laminate curvature matrix

As previously stated the HTCL coupon is balanced with respect to material and symmetry. When this occurs the shear forces induced by the off axis, or 0° plies in this case, are cancelled out as seen in Figure 4.18. These shear forces populate the extension bending coupling matrix. With these forces absent the B matrix values are nullified.

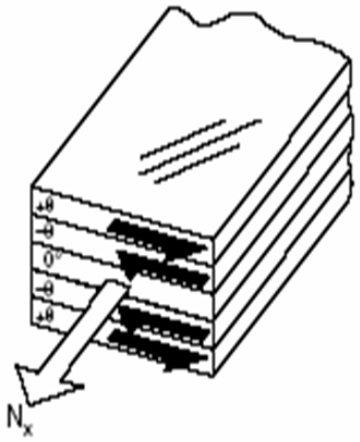

Figure 4.18 CLT balancing of shear forces due to symmetry with axial loading

The modified equation resulting from the symmetry in seen below:

$$\begin{bmatrix} N \\ M \end{bmatrix} = \begin{Bmatrix} A & 0 \\ 0 & D \end{Bmatrix} \cdot \begin{bmatrix} \varepsilon \\ \kappa \end{bmatrix} \tag{4.2}$$

The only external force applied to the HTCL coupon was axial loading, N, which is this case, is parallel to the 0° layers. This can be seen in Figure 4.18. The resulting equation (4.3) is as follows:

$$\begin{bmatrix} N \\ 0 \end{bmatrix} = \begin{Bmatrix} A & 0 \\ 0 & D \end{Bmatrix} \cdot \begin{bmatrix} \varepsilon \\ \kappa \end{bmatrix} \tag{4.3}$$

With no external moment applied to the specimen the bending stiffness matrix is decoupled. Once the D matrix is decoupled no curvature, κ, can result and the laminate is only coupled through the extension stiffness matrix, A. The resulting laminate response is seen in the circled area of Figure 4.19.

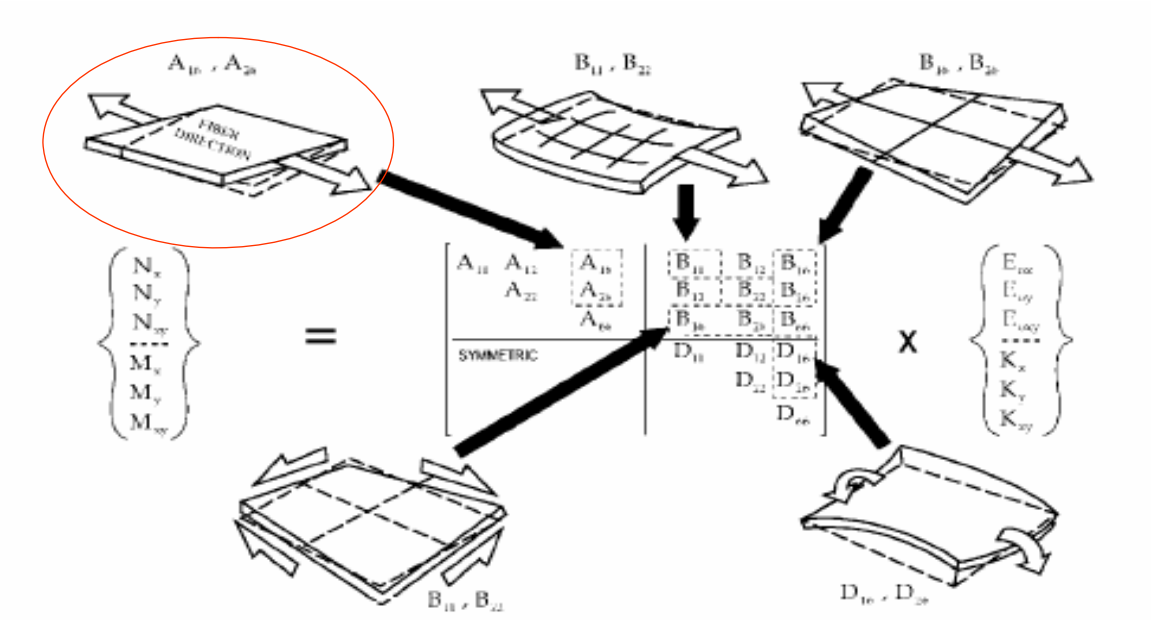

Figure 4.19 Illustration of coupling phenomena in composite plates

The refined force-strain response laminate equation (4.4) requires only extensional stiffness matrix values, A, from CLT. These coupling values were acquired for all the varying Ti-15-3 material properties.

$$[N] = \{A\} \cdot [\varepsilon] \tag{4.4}$$

The inverse of the A matrix and the equivalent applied load, N, for the remote applied stress values were calculated to determine the final laminate strain, ε. The equation is as follows:

$$[\varepsilon] = \{A^{-1}\} \cdot [N] \tag{4.5}$$

All the layers of the HTCL laminate have the same ε value for a given applied load. The layers have the same strain value, but their stress values will differ based on the varying material properties. The laminate strain value (ε) and the individual layer moduli (E) are used to calculate the remote stress in individual lamina through equations (4.6 -7).

$$\sigma = \varepsilon \cdot E \tag{4.6}$$

$$\begin{bmatrix} \sigma_{xx} \\ \sigma_{yy} \\ \sigma_{xy} \end{bmatrix} = \begin{bmatrix} \varepsilon_{xx} \\ \varepsilon_{yy} \\ \varepsilon_{xy} \end{bmatrix} \cdot E \tag{4.7}$$

These values are then used with the SCF values determined in 4.2.2 to determine maximum local stress values.

4.2.2 Lekhnitskii Stress Concentration

Lekhnitskii [44] stated that stress concentration factors for the orthotropic laminate as a whole were insufficient for failure prediction. A layer by layer analysis must be completed in order to determine where the failure will initiate. An orthotropic stress concentration factor K_t for a finite width specimen can be determined from the following expression [44]:

$$K_t = \alpha K_t^{\infty} \tag{4.8}$$

where α = finite width correction factor

K_t^{∞} = stress concentration factor for an infinite orthotropic continuum

The stress concentration factor for an infinite orthotropic continuum containing a circular hole was calculated as [44]:

$$K_t^{\infty} = 1 + \sqrt{\left(\frac{E_L}{G_{LT}} - 2\nu_{LT} + 2\sqrt{\frac{E_L}{E_T}} \right)} \qquad (4.9)$$

For a symmetric laminated plate with orthotropic in-plane stiffness properties, the hole stress concentration factor is given by [44]:

$$K_t^{\infty} = 1 + \left(\frac{2}{A_{22}} \left(\sqrt{A_{11}A_{22}} - A_{12} + \frac{A_{11}A_{22} - A_{12}^{\,2}}{2A_{66}} \right) \right)^{1/2} \qquad (4.10)$$

where A_{11}, A_{22}, A_{12}, and A_{66} = Shear-extension coupling coefficients

To account for geometric differences of actual HTCL coupon in the laminate a finite width correction factor for an isotropic material containing a circular hole is used as follows:

$$\alpha = \frac{2 + [1 - d/W]^3}{[3(1 - d/W]} \qquad (4.11)$$

4.3 Finite Element Analysis

In order to further understand the stresses that are imparted to the embedded titanium ply near the open hole, a finite element analysis was conducted to validate initial loading conditions calculated in MATLAB for use in the fatigue tests. Simulated static loading of the HTCL laminate in ANSYS was used to obtain stress–strain data and stress concentration factors (SCF). Furthermore, work was initiated to model crack growth and damage mechanisms to determine stress intensity factors following cyclic fatigue.

Preliminary predictions were made using Ti-15-3 data collected from tensile test and PMC prepreg data gathered from literature [29, 32, 37, 38].

4.3.1 ANSYS Finite Element

The ANSYS finite element code simulations were created primarily by Amar Atre, Graduate Research Assistant, Georgia Institute of Technology. All layered elements selected, both shell and solid, in ANSYS were specifically designed for composite applications. The HTCL coupons were modeling with quarter symmetry geometry, appropriate symmetric boundary conditions and determined constituent material properties tabulated in Table 3.2 and Table 4.2. Additionally, loading was applied as tabulated in Table 4.4. Schematics of this work can be seen in Figure 4.20 and Figure 4.21 respectively.

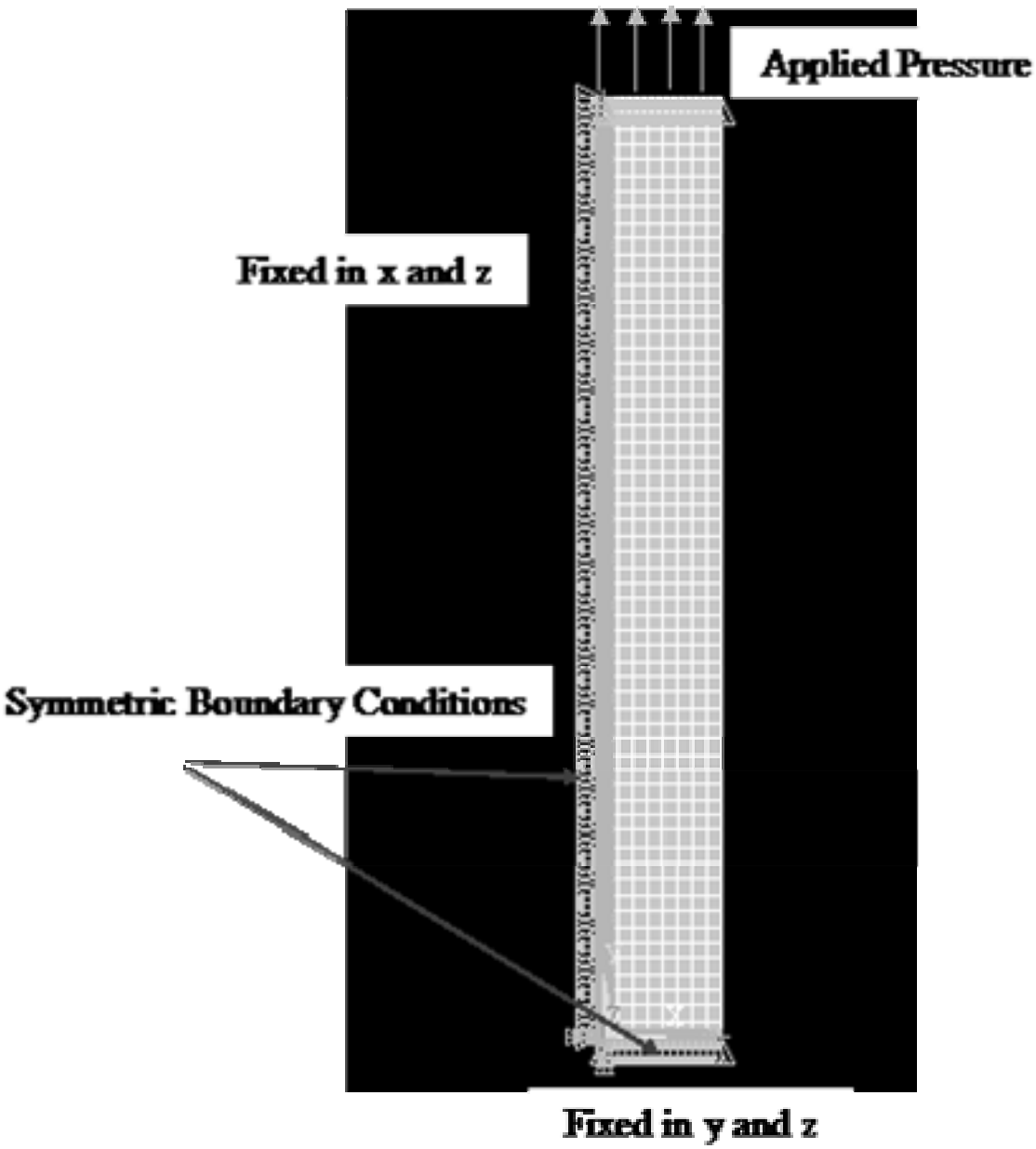

Figure 4.20 HTCL quarter symmetry coupon schematic with boundary conditions and applied stress

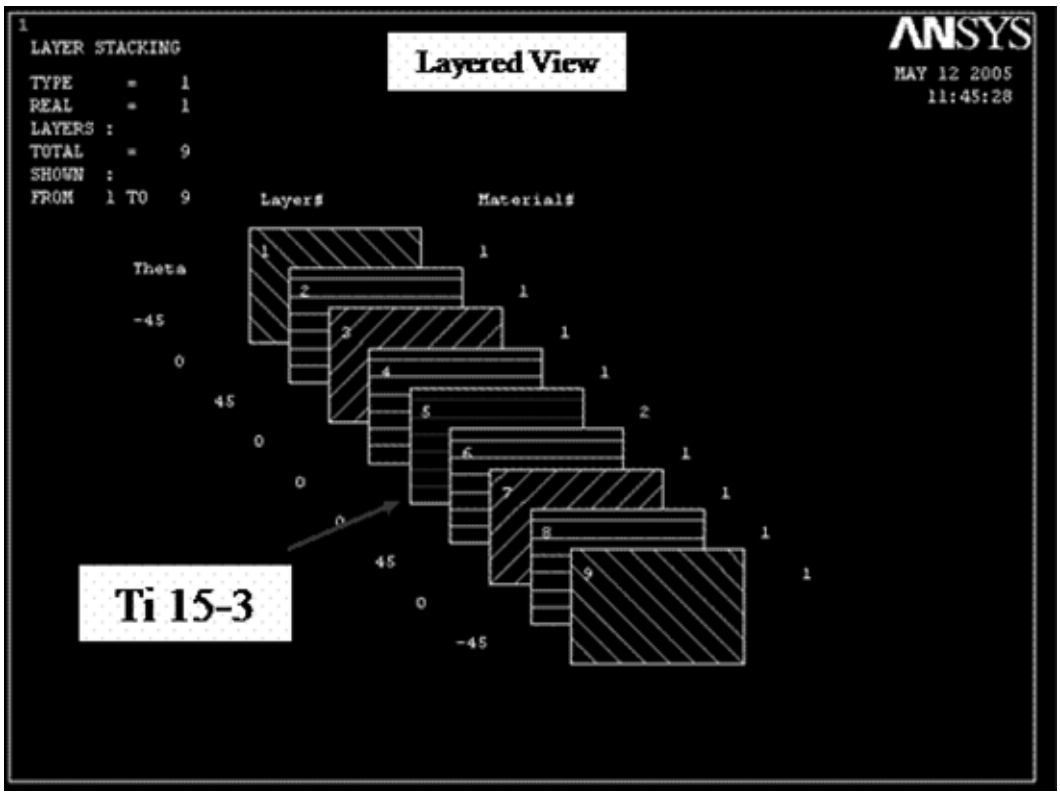

Figure 4.21 Schematic of FE material layering in ANSYS

The first step in this process was to validate the FE model verses the analytical values calculated in the previous section. SHELL 91 elements were utilized due to their ease of implementation and reduction of processing time. A laminate was modeled with no center hole to be used to the validation. Stress states in the varying layers were observed and compared to CLT results. Once the initial validating process was completed a center hole was modeled. Stress concentration factors (SCF) were calculated based on the maximum local stresses and the applied remote loading. An image of the open hole quarter symmetry model is seen in Figure 4.22.

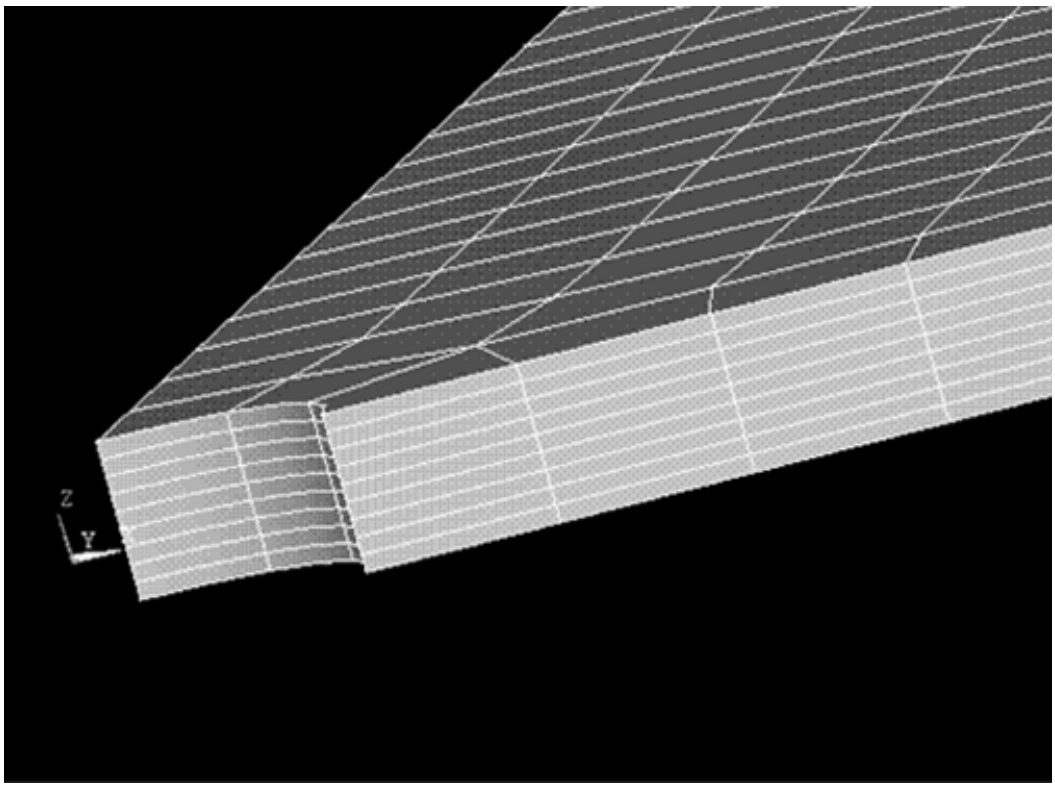

Figure 4.22 Schematic of Open Hole in HTCL coupon using ANSYS

The second step was to compare the SHELL 91 element results to the SOLID 46 element models. SOLID 46 elements are required to simulate the crack opening and other damage mechanisms. This was accomplished through nodal release and other FE elements techniques.

CHAPTER 5

RESULTS AND DISCUSSION

In this chapter, the results from the mechanical characterization testing of titanium foil, foil microscopy with digital associated imaging, HTCL fatigue testing, HTCL evaluation techniques, the analytical results from MATLAB code and finite element analysis from ANSYS modeling are presented and discussed.

5.1 Experimental Tests

Experimental tests were conducted to characterize both the Beta Ti-15-3 foil and the HTCL systems. The results from the tensile testing, fatigue testing and microscopic inspection are presented in the following sections.

5.1.1 Ti Foil

The results for the static tensile tests and associated microscopic inspection are presented and discussed.

5.1.1.1 Modulus

The Ti-15-3 foils were statically tensile tested to determine modulus data for use in analytical and finite element analysis. The results of the modulus testing are presented in Table 5.1. The AR foil showed the highest longitudinal stiffness of the materials tested and the SN foil proved to be the most compliant. The other heat treated had progressively lower stiffness values than AR, but still greater than the SN. The combination of allotropic phase volumes and grain alignment are the reasons for the

varying properties. These differences will be discussed in more detail in section5.1.1.4. The results were similar for the transverse modulus data and the Poisson's ratio (ν_{12}) for all the heat treatment were equal.

Table 5.1: Experimentally determined properties of Ti-15-3 foil following various heat treatments (* G_{12} data from Boyer [32])

Heat Treatment	E_{11}	E_{22}	G_{12}^*	ν_{12}
As Received (AR)	102.7 GPa (14.9 msi)	101.4 GPa (14.7 msi)	43.0 GPa (6.24 msi)	.34
1025° F HT (1025)	100.7 GPa (14.6 msi)	99.3 GPa (14.4 msi)	43.0 GPa (6.24 msi)	.34
1100° F HT (1100)	98.6 GPa (14.3 msi)	97.9 GPa (14.2msi)	43.0 GPa (6.24 msi)	.34
Solution Treatment (SN)	82.0 GPa (11.9 msi)	82.0 GPa (11.9 msi)	43.0 GPa (6.24 msi)	.34

5.1.1.2 Yield Strength

The Ti-15-3 foils were then statically tensile tested to determine yield strength data for use in analytical analysis and finite element modeling. The results of the tensile testing for yield strength for both a .02% and .2% offset are presented in Table 5.2. The AR foil showed the highest yield strength of the materials tested and the SN foil plastically deformed at the lowest applied stress. The other heat treated had progressively lower yield strength values than AR, but still greater than the SN. The combination of

allotropic phase volumes and grain alignment are the reasons for the varying properties. These differences are discussed in more detail in section5.1.1.4.

Table 5.2: Experimental results for average yield strength of Ti-15-3 foil with various heat treatments

Heat Treatment	σ_y (.02 % offset)	σ_y (.2 % offset)
As Received	1.16 GPa (168 ksi)	1.17 GPa (170 ksi)
1025° F HT	1.01 GPa (147 ksi)	1.03 GPa (150 ksi)
1100° F HT	.917 GPa (133 ksi)	.944 GPa (137 ksi)
Solution Treatment	.661 GPa (96 ksi)	.682 GPa (99 ksi)

5.1.1.3 Elongation/Ultimate Strength

The Ti-15-3 foils were then tensile tested to failure to determine elongation and ultimate tensile strength data for use in analytical analysis and finite element modeling. The results of the tensile testing are presented in Table 5.3 and Table 5.4. The AR foil showed the highest average ultimate strength and the least % elongation, which was to be expected based on the previous data. Similarly, the SN foil strained 9% more than the next closest foil. The other heat treated foils had progressively lower elongation values than the SN foil. Figure 5.1 shows the observed strain hardening of the AR, 1025 and 1100 foil. It was also observed that the SN foil did not harden. Figure 5.2 shows the true stress-strain values which have been corrected for the effect of specimen necking during the tensile testing. All the heat treatments appear to strain hardened and show less elongation when the true stress-strain values are used.

Table 5.3: Experimental results for average crosshead displacement and elongation % of Ti-15-3 foil with various heat treatments

Heat Treatment	**Displacement**	**Elong %**
As Received	6.35 mm (.25 in)	9
1025° F HT	7.11 mm (.28 in)	10.5
1100° F HT	9.14 mm (.36 in)	13
Solution Treatment	15.24 mm (.60 in)	22

Table 5.4: Experimental results for average ultimate strength of Ti-15-3 foil with various heat treatments

Heat Treatment	σ_{ult}
As Received	1.24 GPa (180 ksi)
1025° F HT	1.11 GPa (161 ksi)
1100° F HT	1.01 GPa (147 ksi)
Solution Treatment	.710 GPa (103 ksi)

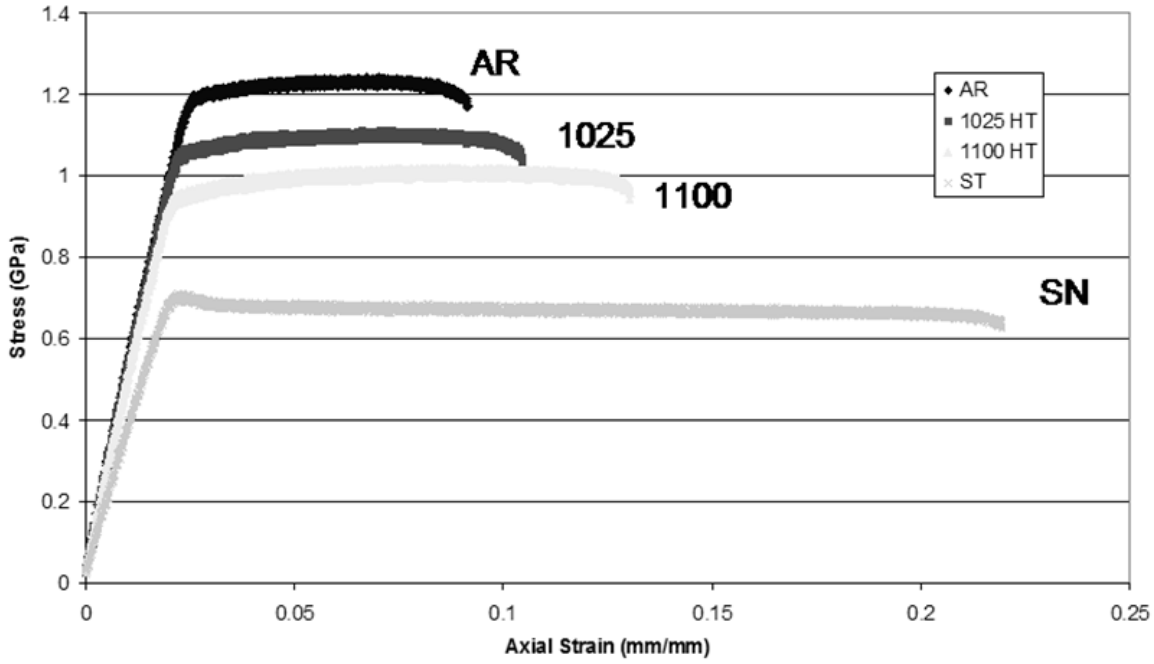

Figure 5.1 Comparison between experimental actual tensile test results of different heat treated Ti-15-3 foil (no correcting for necking)

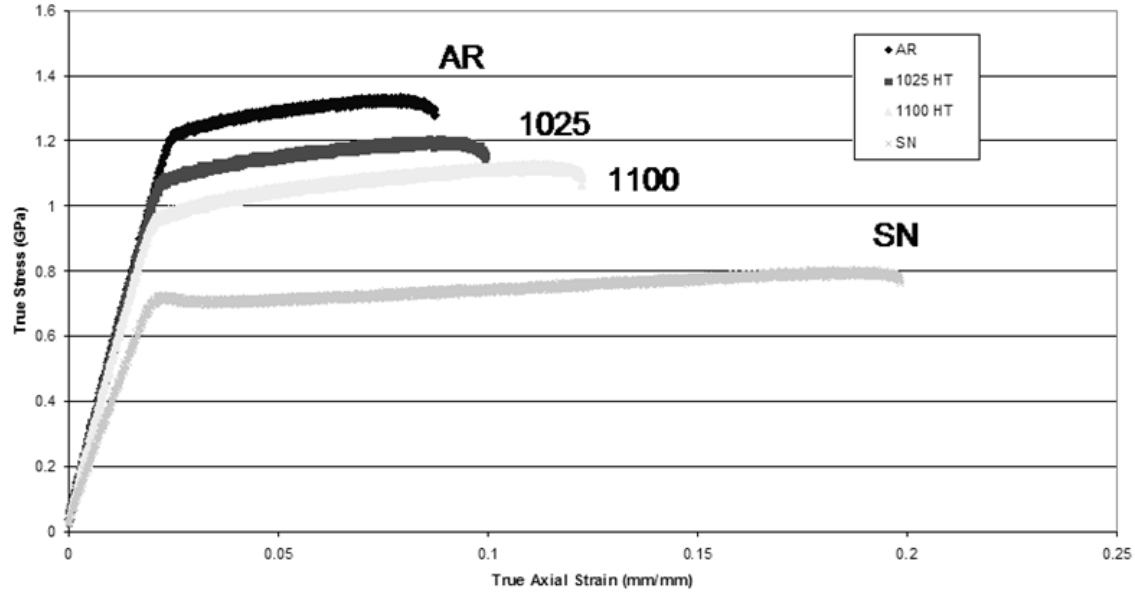

Figure 5.2 Comparison between experimental true tensile test results of different heat treated Ti-15-3 foil (corrected for necking – natural log strain)

Inspection of the fracture surfaces revealed that the AR, 1025 and 1100 foil all had predominant oblique fracture surfaces and Luder's bands were visible on the specimens near the fracture region. Luder's bands are series of dislocations that are forming in great numbers along a given slip plane. Moderate necking was also observed during the tests. The image on the left side of Figure 5.3 shows this type of fracture and the associated damage with these failures.

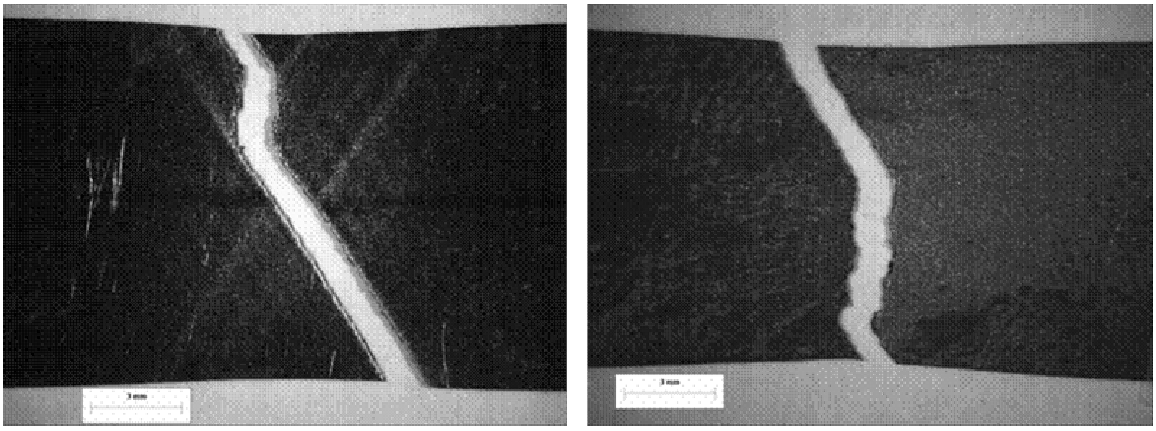

Figure 5.3 Images of predominant oblique fracture (AR, 1025 and 1100 foil) with Luder's bands (left) and fraction oblique fracture (SN foil) with ductile characteristics (right) following Ti-15-3 foil tensile tests

The SN foil had fraction oblique fracture surfaces with smaller cracks and severe surface deformation due to the elastic spring back that occurred upon ultimate failure outside of the gage section. Extreme necking in the gage section was seen during the tensile testing. Clip gage extensometers had to be employed due to the fact that the necking caused the strain gages to debond. The image on the right side of Figure 5.3 shows this type of fracture and the associated damage with these failures.

5.1.1.4 Microstructure

The AR foil microscope image, which is seen in Figure 5.4, shows a very large number of fine alpha (α) precipitates in a beta (β) matrix. The α precipitates, which appear as numerous small dark spots just inside the grain boundaries, are what strengthen the Ti foil. The hexagonal close pack (HCP) crystalline structure of α phase is the reason for strengthening. The larger volume of α precipitates, in accordance with the rule of mixtures, produces the higher modulus, yield strength and ultimate strength values. The trade off is that the material is far less ductile and has lower damage tolerance. The presence of α precipitates also interferes with dislocation motion and causes slip bands to form. These slip bands lead to oblique fractures and Luder's band formation, which were observed in the AR foil. Also, the grains in the AR foil have retained the majority of cold forming characteristics that also increase modulus and strength characteristics. The grains have an elongated shape and have relatively uniform grain size. There are also well defined grain boundaries which resist crack propagation.

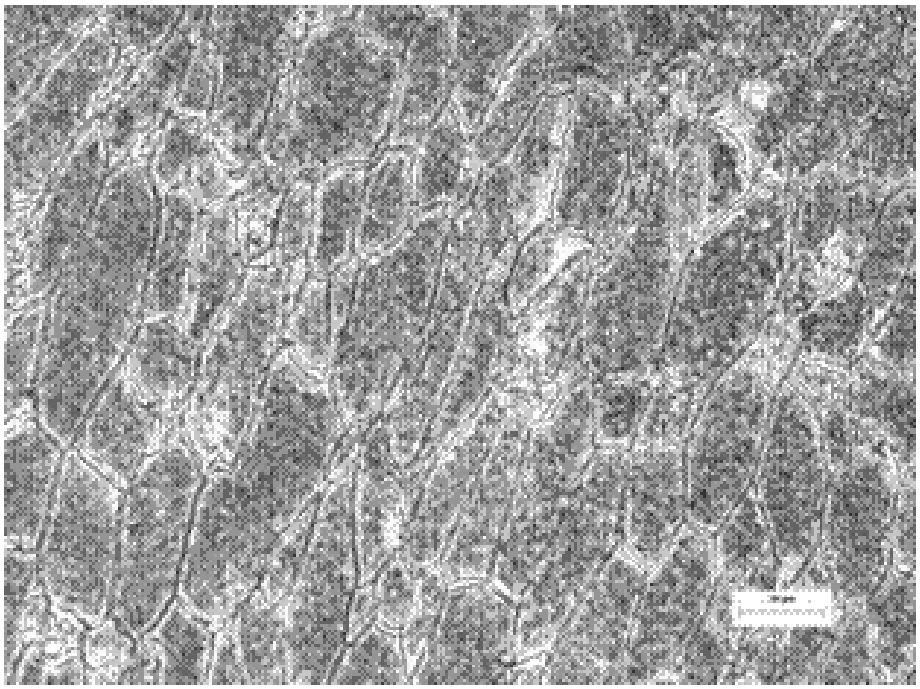

Figure 5.4 Microscopy image of AR Ti-15-3 following polishing and etching (30 micron bar)

The 1025 foil microscope image, which is seen in Figure 5.5, shows fewer numbers of α precipitates in a β matrix. As with the AR foil α precipitates strengthen the Ti foil. Since α precipitate formation is a function time and temperature, the additional heat treatment of this foil has reduced the overall number of α precipitates. Aging of titanium alloys at higher temperatures tends to lower the amount of α precipitation. Shorter aging times also lower the amount of α precipitation that occurs. This in turn has lead to slightly lower strength and modulus values. The ductility was improved by the by the greater volume of β phase, which has a body centered cubic (BCC) crystalline structure. The grains are somewhat less elongated and the grain boundaries are not as organized.

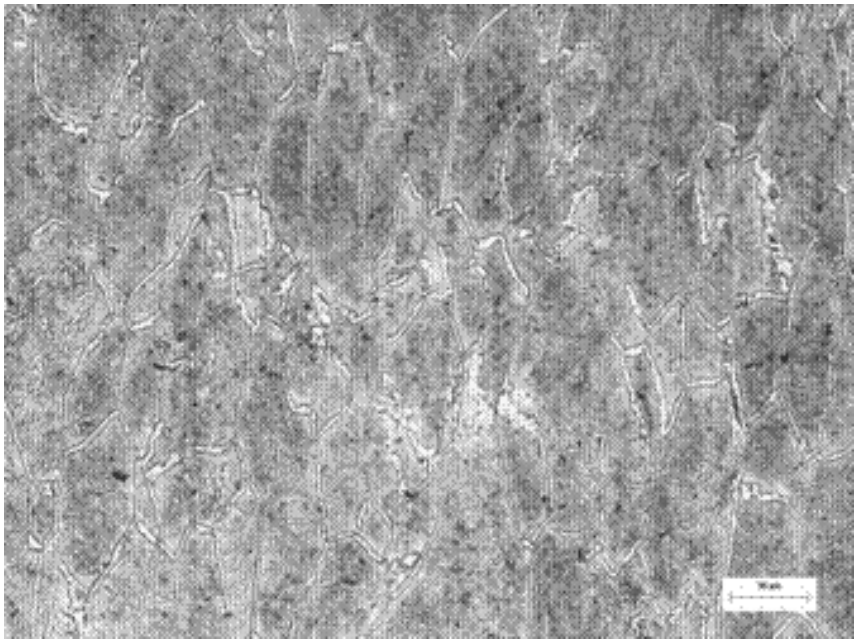

Figure 5.5 Microscopy image of 1025 Ti-15-3 following polishing and etching (30 micron bar)

The 1100 foil microscope image, which is seen in Figure 5.6, again shows fewer numbers of α precipitates in a β matrix. As previously stated, since α precipitate formation is a function of time and temperature, the higher temperature of the heat treatment of this foil has further reduced the overall number of α precipitates. This in turn has lead to slightly lower strength and modulus values. The ductility was improved by the greater volume of β phase, which has a body centered cubic (BCC) crystalline structure. The grains are again less elongated and the grain boundaries are not as organized as in the 1025 foil.

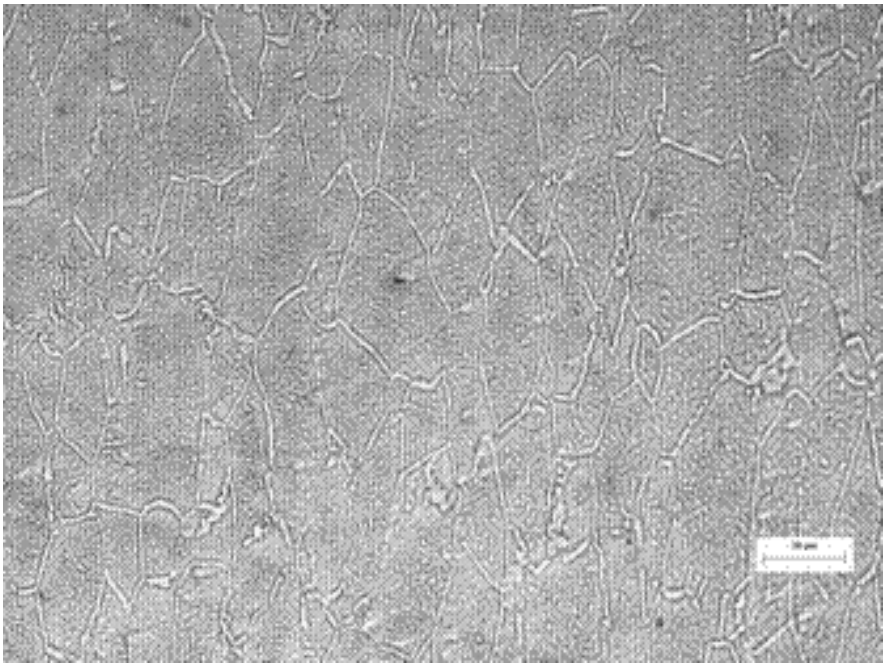

Figure 5.6 Microscopy image of 1100 Ti-15-3 following polishing and etching (30 micron bar)

The ST foil microscope image, which is seen in Figure 5.7, shows almost entirely single phase β matrix. The solution heat treatment elevated the Ti-15-3 above its 883^{o} C (1621^{o} F) beta transus temperature, where the more ductile β phase is formed, and then was rapid quenched using argon. This quenching process effectively froze the β phase and did not allow for α formation during cooling. As the experimental results have shown the ST foil is much more ductile and does not have the increase modulus or strength characteristics of an α strengthened structure. Additionally, the grains have no directional alignment, uniform size or well developed grain boundaries. As previously stated, this could lead to earlier crack initiation, but the SN foil should have greater damage tolerance following initiation [33, 34].

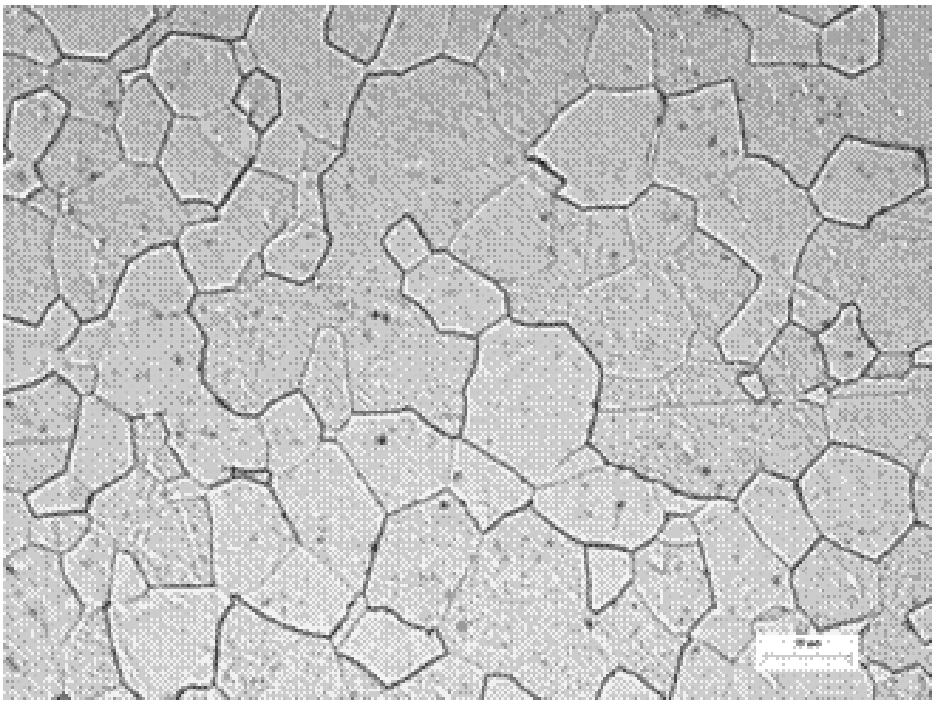

Figure 5.7 Microscopy image of SN Ti-15-3 following polishing and etching (30 micron bar)

5.1.2 HTCL Constant Amplitude Fatigue Characterization

The results for constant amplitude fatigue tests are presented in the following sections. X-ray imaging validation, crack initiation, crack grow rates, compliance and other damage mechanisms as a result of cyclic tension-tension fatigue on the HTCL laminate, with emphasis placed on the Ti-15-3 ply, are presented. These tension-tension tests were performed at a stress ratio (R) equal to 0.1. The specimens were cycled at a frequency of 10 Hz to a pre-determined final value greater than the average lifecycle of an aircraft with an applied safety factor which is approximately 300,000 cycles. A discussion of these results is also included.

5.1.2.1 X-ray Imaging Validation

Measurements of the exposed Ti-15-3 foil were taken and compared with x-ray image measurements taken before the matrix digestion process. The correlation between the actual cracks and the cracks seen in the radiographic inspection was exact for location and 97% correct for length. The comparison of images can be seen in Figure 5.8.

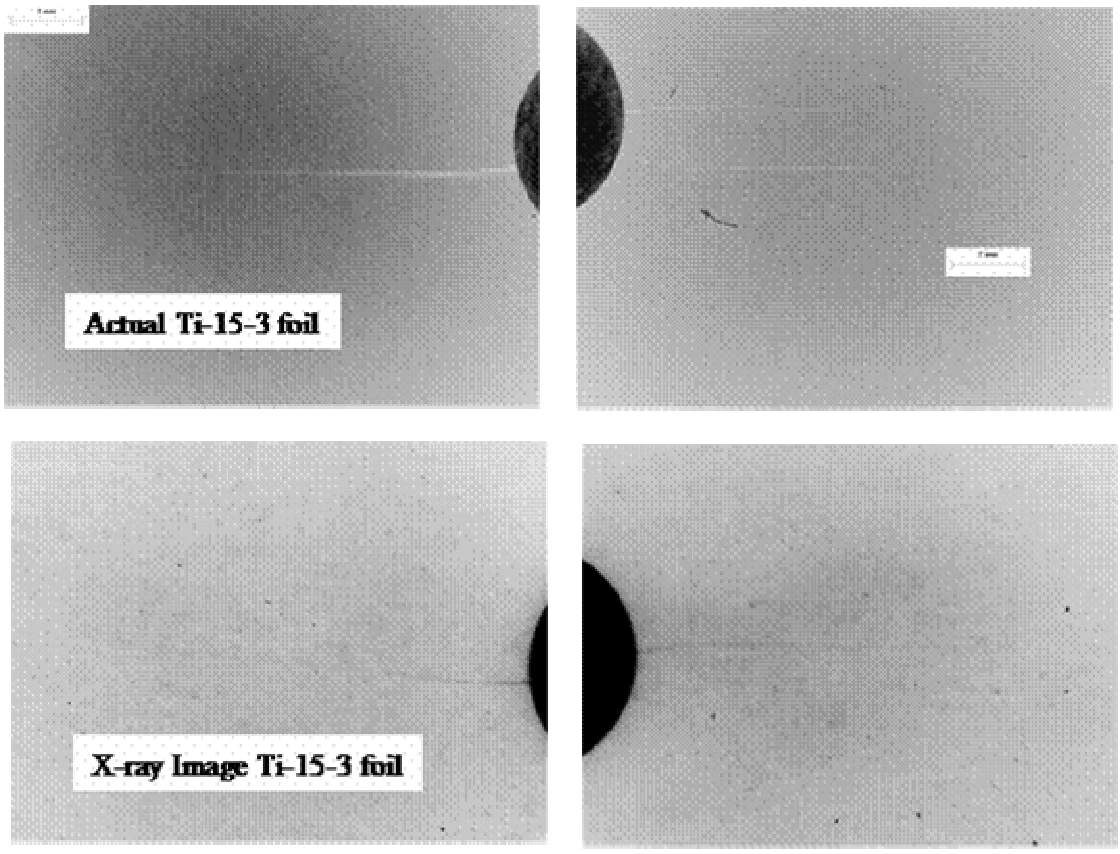

Figure 5.8 Images from radiographic crack detection validation process.

5.1.2.2 Crack Initiation

As an area of great interest, crack initiation was highly scrutinized during experimentation. While the results from both the analytical and finite element analysis when compared to fatigue life data for the Ti-15-3 gave an approximate range of

expected initiation, the actual interaction of the Ti ply within the HTCL laminate was difficult to gage. The determination of actual crack initiation, which occurs on an atomic level, would be not feasible using the macro scale procedures employed in this study. Therefore the idea of an initial reliably detectible crack size was applied in this research. This crack size was determined as a point in which traditional non destructive evaluation techniques would have an extremely high probability of detection. A value of 0.254 mm (.01 in) was applied as the initial reliably detectible crack size.

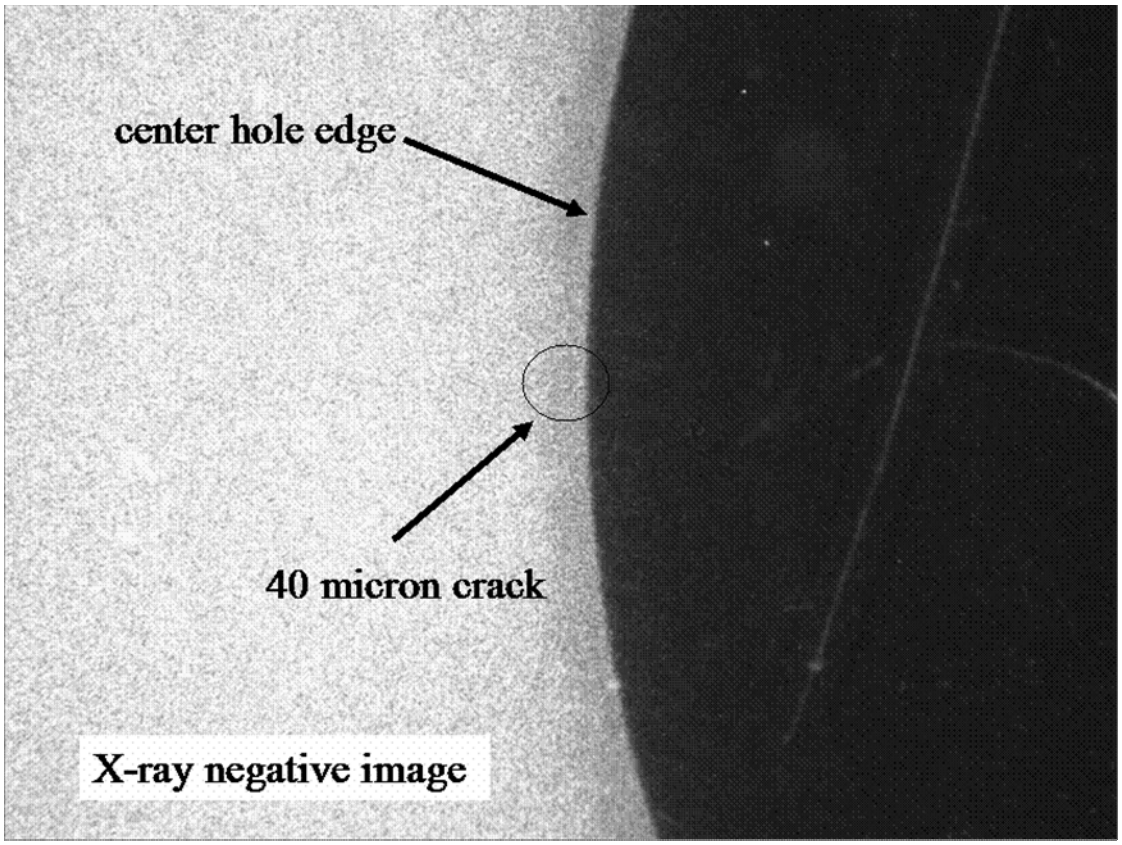

Figure 5.9 X-ray image of 40 micron crack in embedded Ti of HTCL coupon after fatigue at 30 ksi for 35,000 cycles at R=0.1 and frequency of 10 Hz

The use of visual observation, crack replication, x-ray imaging, and regression analysis were employed to determine the point during the fatigue life of the HTCL in which this value was reached in the embedded Ti ply. It was hoped that the tempering of the Ti ply would lead to delayed initial cracking and subsequent damage retardation.

Initial attempts to visually observe this event with a traversing microscope proved difficult due to the obstruction created by the shielding box required for x-ray imaging and the similar light reflective properties of the adjacent 0° carbon fiber plies. While this procedure may be effective for standard fatigue test setups, it proved to be ineffective for detecting cracks in the HTCL coupons.

Crack replication and x-ray imaging proved much more useful but still had limitations for this particular application. Both are labor and time intensive, so fatigue cycle intervals for use were followed for both techniques. The problem lies in the fact that titanium is very notch sensitive and initial crack growth is very rapid. Initial cracks were detected in the different tempered Ti ply of the HTCL at remote stress values of 206.8 MPa (30 ksi), 172.4 MPa (25 ksi) and 158.6 MPa (23 ksi) with varying degrees of certainty. No cracks of any size were detected in the HTCL when a remote stress of 137.9 MPa (20 ksi) was applied. Table 5.5 shows the average number of cycles for initial crack detection of any size obtained by replication and x-ray. The number of cycles to initial detection goes against the statements made in the previous section that crack initiation should appear in the ST specimens prior to the AR, 1025, 1100 specimens. While the initiation of cracks may occur first in the ST specimens for a given applied stress, this would happen on an atomic level and is not detectible by our inspection capabilities. Comparison between results of initial crack data of embedded Ti crack

length for the four Ti-15-3 foil heat treatments in HTCL laminates are shown in Figure 5.10 and Figure 5.11 with 2nd order polynomial trend lines added. The scatter in the data is a result of the somewhat unpredictable fatigue properties of the metallic foil and the fact that crack detection is truly "hit or miss". This is why an initial reliably detectible crack size will provide a better yardstick to measure the fatigue characteristics of the HTCL variations.

Table 5.5: Comparison of the number of fatigue cycles to the initial crack detection by any inspection technique

Applied Stress MPa (ksi)	HTCL (AR)	HTCL (1025)	HTCL (1100)	HTCL (SN)
206.8 (30)	15,000	10,000	10,000	20,000
172.4 (25)	20,000	20,000	20,000	40,000
158.6 (23)	300,000	200,000	300,000	200,000
137.9 (20)	N/A	N/A	N/A	N/A

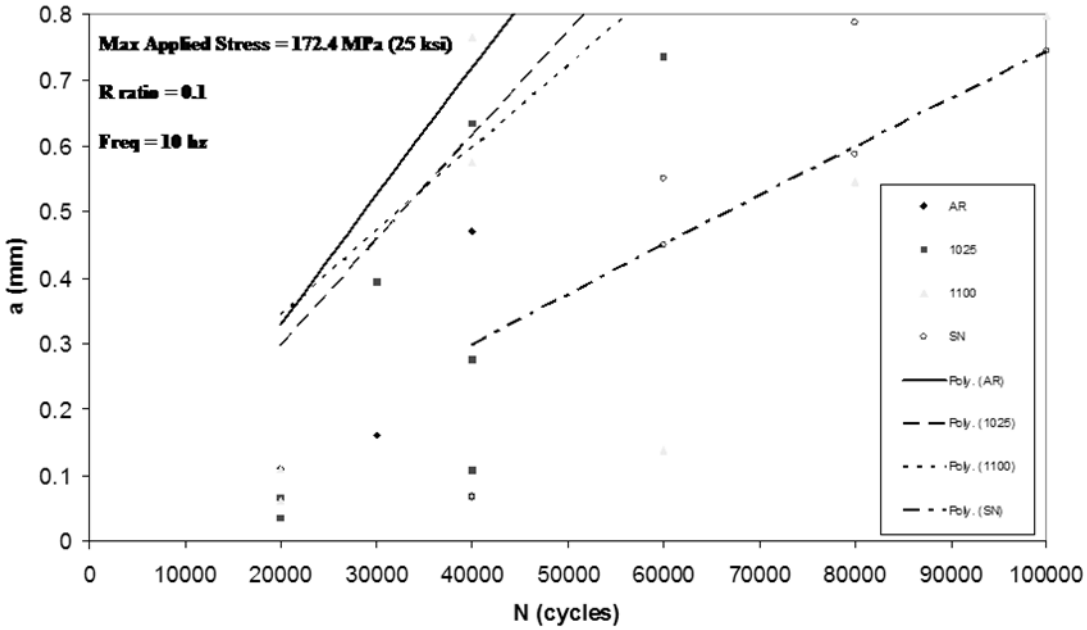

Figure 5.10 Comparison between results of embedded Ti crack length (a) vs constant amplitude fatigue cycles (N) for 4 Ti heat treatments in a [45/0/-45/0/Ti]s at 172.4 MPa (25 ksi) (initial crack data range)

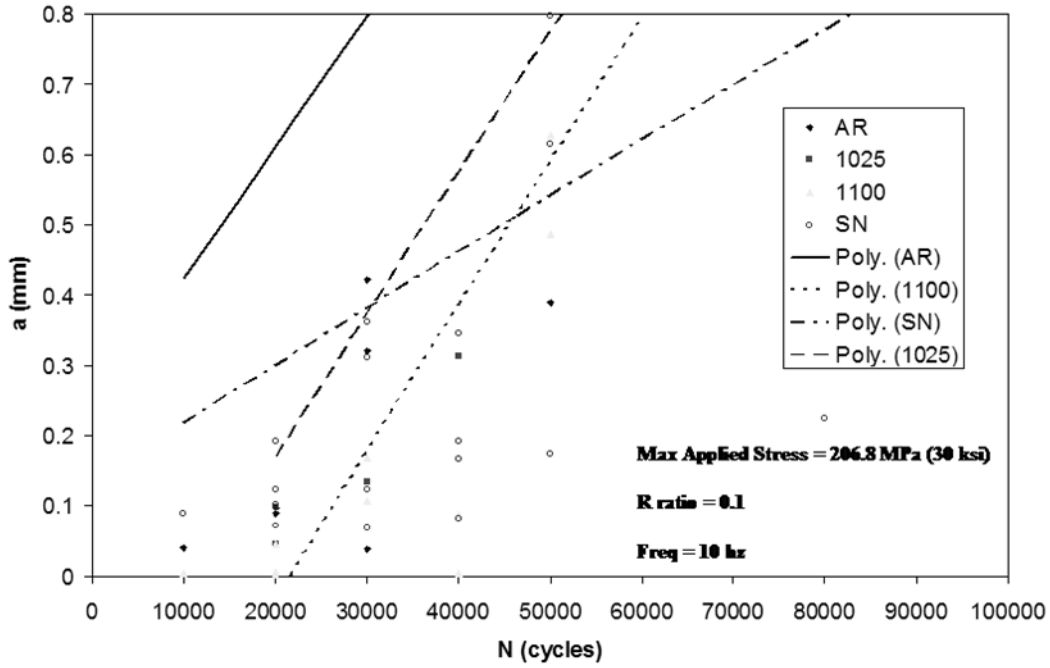

Figure 5.11 Comparison between results of embedded Ti crack length (a) vs constant amplitude fatigue cycles (N) for 4 Ti heat treatments in a [45/0/-45/0/Ti]s at 206.8 MPa (30 ksi) (initial crack data range)

The information on crack growth data in section 5.1.2.3 and the previously presented initiation data on average number of fatigue cycles to the initial crack detection can be used in trend calculations to determine the number of fatigue cycles to obtain the initial reliably detectible crack size. The cycles were projected for a 0.254 mm (.01 in) crack using crack growth data for the HTCL coupons and a MS Excel TREND function with exponential growth equation included. Table 5.6 shows the results of this analysis for the number of cycles (in thousands) to smallest reliably detectible crack for the applied stress levels of 206.8 MPa (30 ksi) and 172.4 MPa (25 ksi). No cracks in the 158.6 MPa (23 ksi) applied stress testing produced cracks greater than 0.254 mm (.01 in), so they were not considered. When comparing the results of this analysis there appears to a slight delay in initial crack detection for the HTCL specimens as the embedded Ti ply

heat treatment was changed from as received (AR) condition to the solution treated (SN) laminate for both applied stresses. The combination of fiber bridging and the improved damage tolerance properties of the Ti foil are the probable reasons for the results observed.

Table 5.6: Comparison of the calculated number of fatigue cycles to obtain an initial reliably detectible crack size of 0.254 mm (.01 in)

Applied Stress MPa (ksi)	HTCL (AR)	HTCL (1025)	HTCL (1100)	HTCL (SN)
206.8 (30)	31,100	31,900	41,200	45,000
172.4 (25)	33,700	34,300	43,700	49,700

The use of radiography or crack replication for determination of crack initiation in HTCL specimen is limited and other techniques would prove more useful for this evaluation. One such technique is thermoelastic stress analysis (TSA), which will be discussed in section 5.1.2.5.2.

5.1.2.3 Crack Growth Rates

Following the initial crack detection, x-ray images were taken at a predetermined fatigue cycle interval under applied loads to observe damage propagation. This series of images allowed for the collection of crack growth characteristics in the embedded Ti ply that could not be observed from surface inspection. All cracking observed was in the Ti ply originating from the center open hole of the coupon. As stated in the previous section cracks were detected in the different tempered Ti ply of the HTCL at remote stress values of 206.8 MPa (30 ksi), 172.4 MPa (25 ksi) and 158.6 MPa (23 ksi). Each series of remote applied stress levels will be discussed, but not each individual coupon tested.

The HTCL coupons that were fatigue tested at a remote stress level of 206.8 MPa (30 ksi) produced cracks that were easily distinguishable in x-ray images. Radiographic images had high image quality and sharp contrast. Crack mouth and tip features were pronounced. A case with two cracks emanating from the center open hole will provide for detailed discussion of crack growth characteristics. An embedded as received Ti ply crack initiating on the right side of the open hole at 20,000 cycles is shown in Figure 5.12. X-rays of the HTCL specimen were then taken at 40, 60, 80, 100, 200, 300 and 500 thousand cycles. After processing the x-ray images were then viewed under the stereographic microscope to determine the crack length and path for each number of fatigue cycles. The progression and magnitude of cracking as fatigue cycles accumulate can be seen in Figure 5.13 through Figure 5.19. The images on the right have not been modified while the images on the left have the cracks highlighted for better viewing.

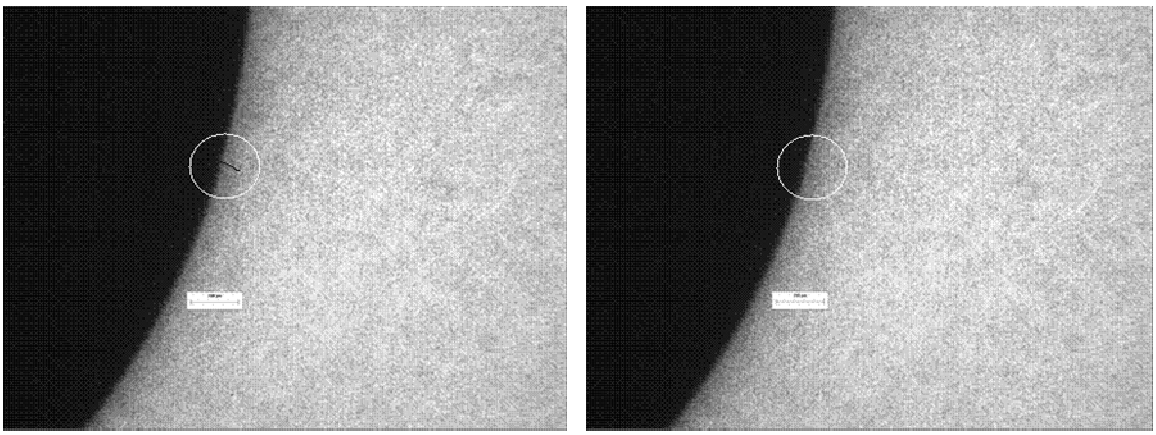

Figure 5.12 X-ray modified (left) and actual (right) image of .110 mm (.004 in) crack in embedded Ti of HTCL coupon after fatigue at 206.8 MPa (30 ksi) for 20,000 cycles at R=0.1 and frequency of 10 Hz

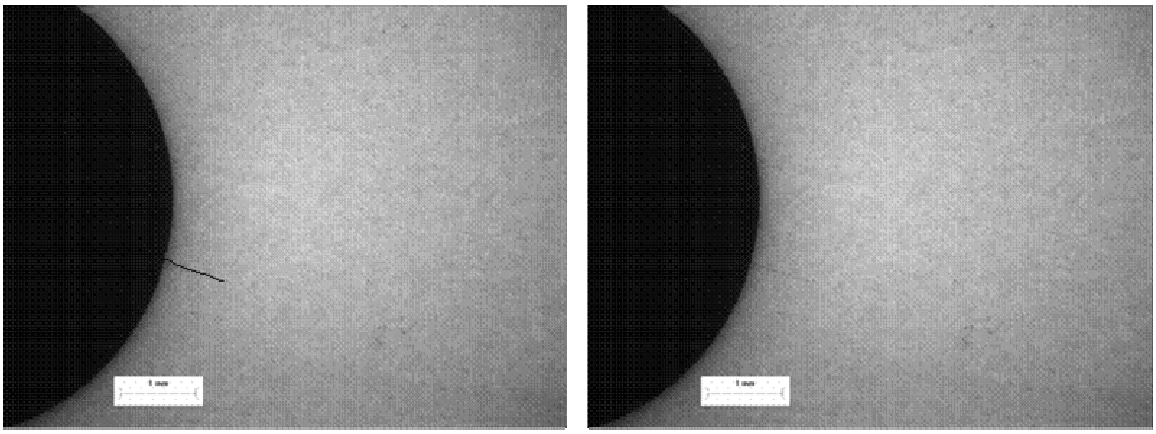

Figure 5.13 X-ray modified (left) and actual (right) image of .474 mm (.019 in) crack in embedded Ti of HTCL coupon after fatigue at 206.8 MPa (30 ksi) for 40,000 cycles at R=0.1 and frequency of 10 Hz

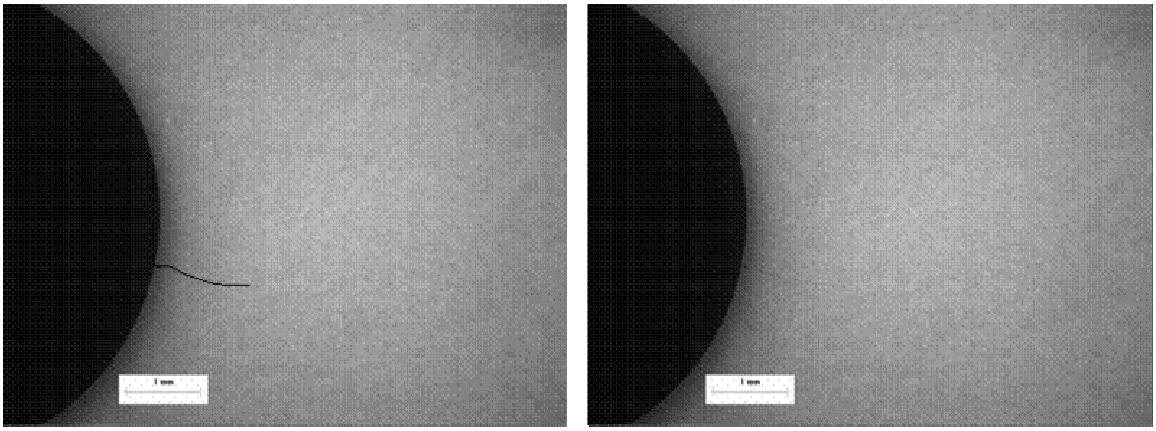

Figure 5.14 X-ray modified (left) and actual (right) image of 1.319 mm (.052 in) crack in embedded Ti of HTCL coupon after fatigue at 206.8 MPa (30 ksi) for 60,000 cycles at R=0.1 and frequency of 10 Hz

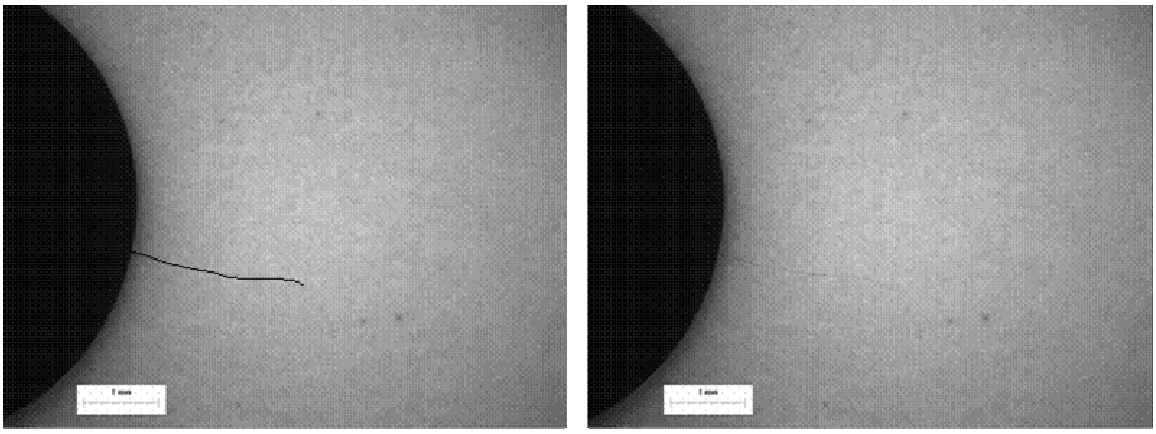

Figure 5.15 X-ray modified (left) and actual (right) image of 1.805 mm (.071 in) crack in embedded Ti of HTCL coupon after fatigue at 206.8 MPa (30 ksi) for 80,000 cycles at R=0.1 and frequency of 10 Hz

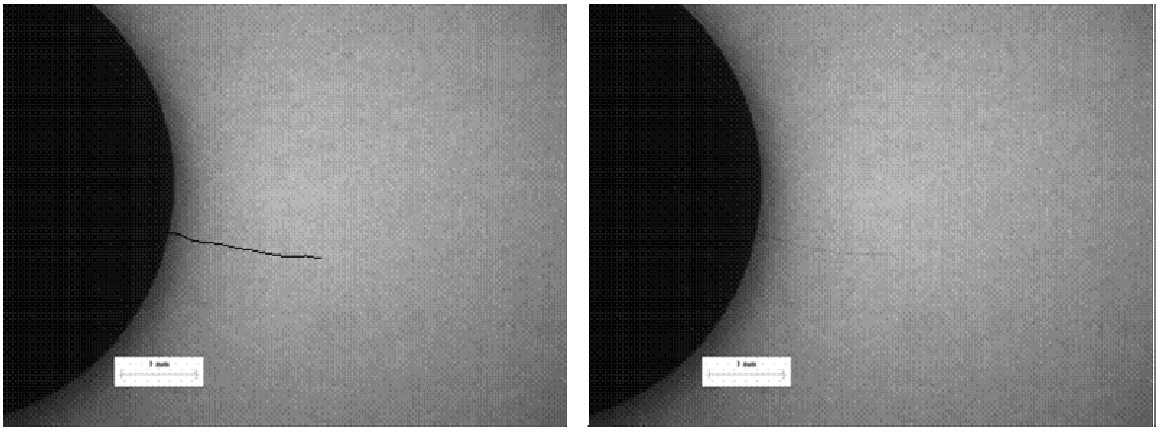

Figure 5.16 X-ray modified (left) and actual (right) image of 1.928 mm (.076 in) crack in embedded Ti of HTCL coupon after fatigue at 206.8 MPa (30 ksi) for 100,000 cycles at R=0.1 and frequency of 10 Hz

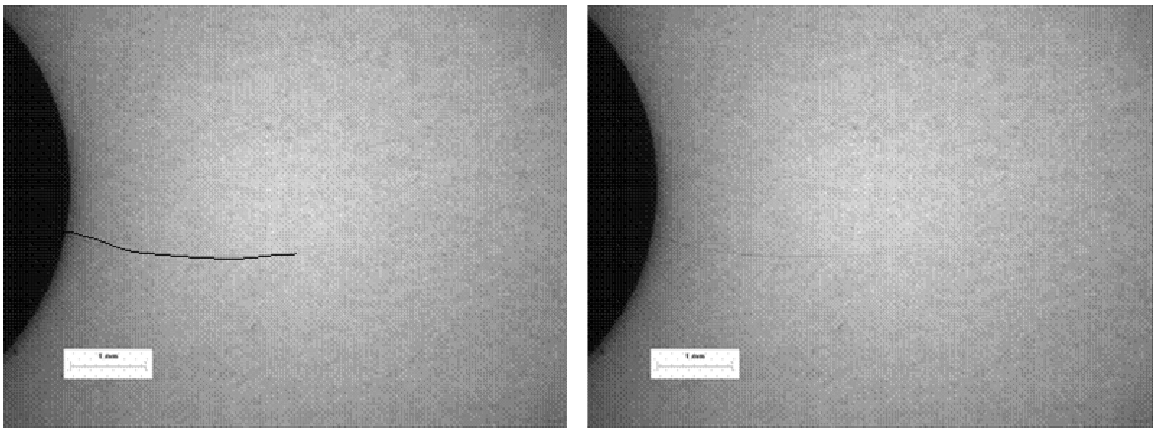

Figure 5.17 X-ray modified (left) and actual (right) image of 3.148 mm (.123 in) crack in embedded Ti of HTCL coupon after fatigue at 206.8 MPa (30 ksi) for 200,000 cycles at R=0.1 and frequency of 10 Hz

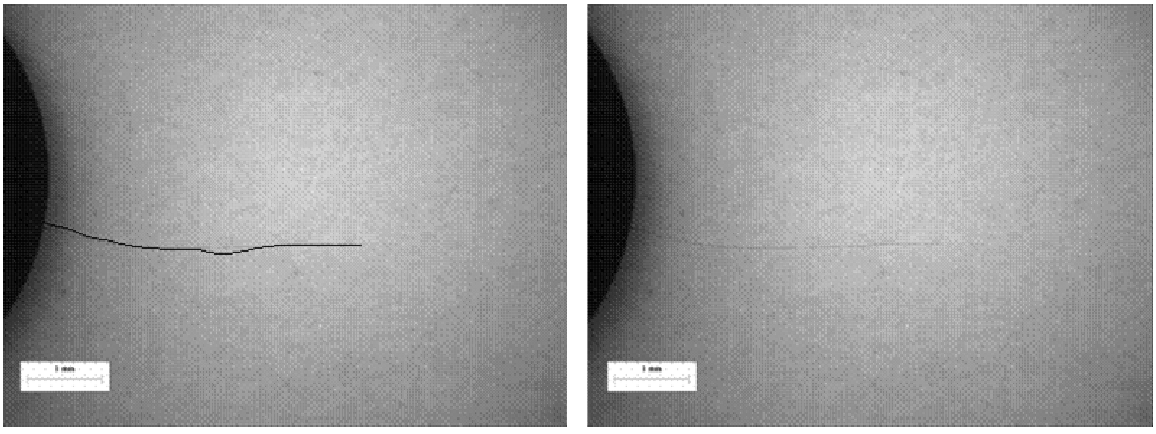

Figure 5.18 X-ray modified (left) and actual (right) image of 4.187 mm (.165 in) crack in embedded Ti of HTCL coupon after fatigue at 206.8 MPa (30 ksi) for 300,000 cycles at R=0.1 and frequency of 10 Hz

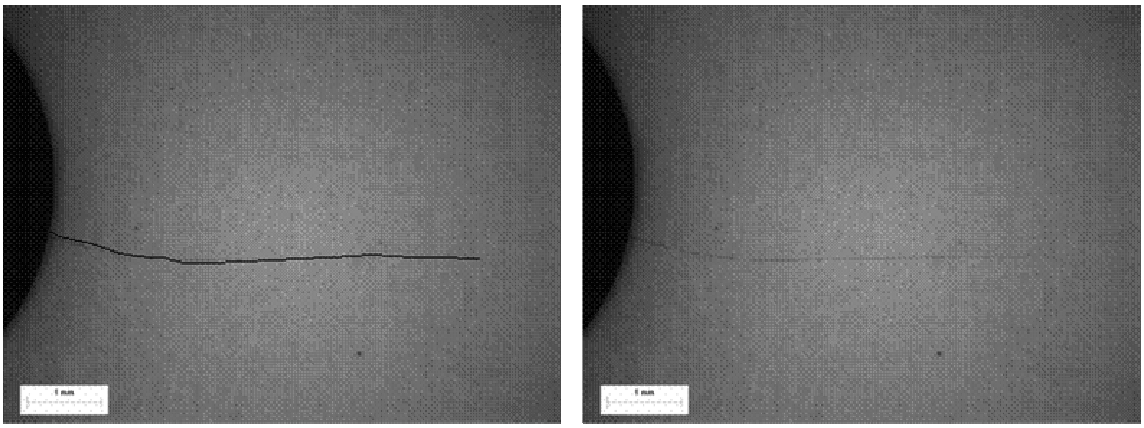

Figure 5.19 X-ray modified (left) and actual (right) image of 5.578 mm (.219 in) crack in embedded Ti of HTCL coupon after fatigue at 206.8 MPa (30 ksi) for 500,000 cycles at R=0.1 and frequency of 10 Hz

A number of observations were made from these figures and the approximately 300 other x-ray images processed in the course of this research. First, the cracks in almost all cases did not initiate at locations on the edge of the open hole that were exactly perpendicular to the applied loading. Second, cracks initially grow away from the open hole at shallow angles and then turn to grow perpendicular to the loading. Third, in most cases multiple cracks are visible in the initial stages of fatigue life and then a certain number of those cracks dominate. Fourth, crack growth rates decrease in all cases following an initial fast growth phase and heat treatment of the embedded Ti foil ply greatly affects crack growth rates. Finally, x-ray image quality decreases with increasing heat treatments.

The initial observation is a result of two probable causes. First, the titanium is very notch sensitive. Even with hole preparation prior to fatigue testing, flaws could be present that could cause crack initiation at locations other than what was expected. Second, and more probable, is that a combination of material and laminate anisotropy lead to the location of the crack. The HTCL coupons are symmetric and balanced, but

localized anisotropy due to interaction of 45^{o} fibers near the hole may create higher stresses at a position not perpendicular with the applied loading. Also, as seen in the foil test results, titanium alloys have some of the highest anisotropy values of any of the isotropic metals. The tendency for Luder's bands to form in these materials and fracture to occur at oblique angles adds to this possibility.

The possible explanation for the second observation was partially tied to the explanation to the first observation. The mixed mode I and II load that was induced by the material and system anisotropy will generate out of plane crack growth within the Ti ply. The crack will continue to grow along a favorable slip plane until the stress intensity factor is such that it grows perpendicular to the applied loading.

The third observation was not as easy to develop an explanation for, in the cases where two or more crack emanated from either side of the open hole as seen in Figure 5.20, a possible cause is that the notch sensitivity of the titanium allowed for multiple cracks to initiate simultaneously. If sufficient energy is provided to the system, then all fatigue cracks will grow simultaneously. This could continue until a point in which one crack may begin to dominate, or shield, other cracks or total energy required to drive the cracks is greater than the energy applied to the specimen. At this point crack growth would decrease or cease. In general it was observed that the HTCL laminates with the higher heat treatments of embedded Ti ply show larger numbers of cracks growing simultaneously at the elevated applied stress levels. It is believed that the combination of a decrease in localized stresses of the higher heat treated Ti plies and the fatigue characteristics of the β phase associated with these heat treatments cause the multiple nucleation points.

Figure 5.20 X-ray images (modified to show crack geometry) of cracks in embedded Ti of HTCL coupon after fatigue at various heat treatments and applied stress levels at R=0.1 and frequency of 10 Hz (fatigue cycles designated and cracks to scale)

The fourth observation is the result of a combination of the fiber bridging mechanism and the damage tolerant characteristics of the embedded Ti ply. The initial fast crack growth phase was one in which insufficient fiber bridging was occurring to transfer enough load from the Ti ply to reduce the effective stress intensity factor at the crack tip. Once the crack reached a certain length, crack growth retardation occurred. Another source of fatigue crack growth (FCG) retardation is that when the cracked ply becomes more compliant it will carry less load. Also it has been suggested, by Dowling [45] and others, that as the small cracks in the Ti ply grow beyond the area of higher stress concentration created by the open in the laminate that a slight decrease in crack growth rate will occur as the crack grows into a growth region dominated by the stress intensity factor at the crack tip . This transitional crack length would lead to a small decrease in crack growth, short crack region, and not long term crack growth retardation, long crack region.

The constituent Ti alloys' heat treatment had a direct impact on the crack growth rates within the HTCL specimen. Figure 5.21 and Figure 5.22 show the results of the fatigue crack growth analysis completed on the HTCL specimen with all data included including initial detections. In Figure 5.21 all the HTCL specimens showed retarded crack growth, the specimens with the SN foil embedded were on average 46 % of the average crack length of the next lowest HTCL type (1100). Again in Figure 5.22 all of the HTCL specimens showed retarded crack growth, the specimens with the SN foil embedded was 60 % of the average crack length of the next lowest HTCL type (1100) at 500,000 fatigue cycles. Figure 5.23 and Figure 5.24 show the results of the fatigue crack

growth analysis completed on the HTCL specimen normalized to the initial reliable detectible crack size of 0.254 mm (0.01 in). Similarly, there was a decrease in the crack growth rates where the SN HTCLs showed final average crack lengths which were 40 % and 53 % respectively of the next lowest heat treatments (1100) crack lengths. Figure 5.25 and Figure 5.26 show the results of the fatigue crack growth analysis completed on the HTCL specimens with the crack length (a) defined as the entire length from crack tip to crack tip including the open hole. Once again crack growth in the SN HTCL specimens was 85% and 81% respectively of the next lowest heat treatments (1100) crack lengths. The reduced crack growth rates in the SN HTCLs were due to the ductile β phase Ti-15-3 which is more damage tolerant. The extent of fiber bridging and directly associated delamination will be discussed in section 5.1.2.5.2. The results of the destructive evaluation of one of the HTCL specimen following TSA is of great interest to future research of the HTCL system.

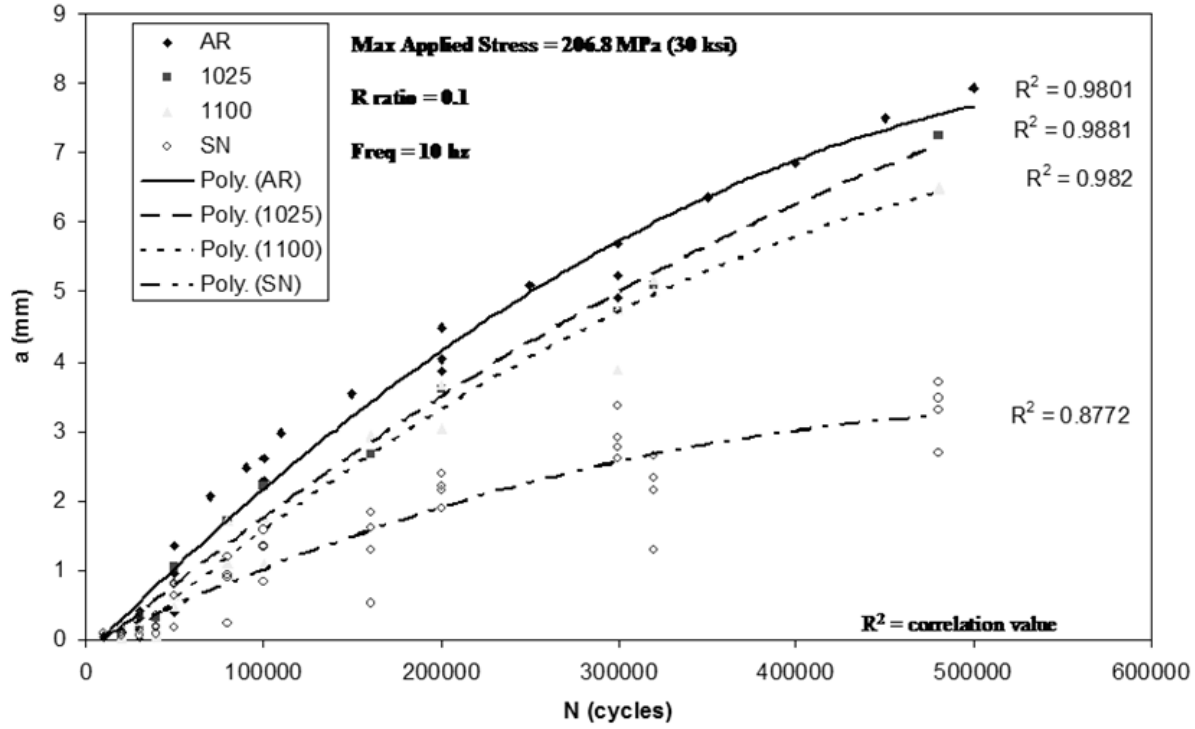

Figure 5.21 Comparison between results of embedded Ti crack length (a) vs constant amplitude fatigue cycles (N) for 4 Ti heat treatments in a [45/0/-45/0/Ti]s at 206.8 MPa (30 ksi) (range of data to 500 k cycles)

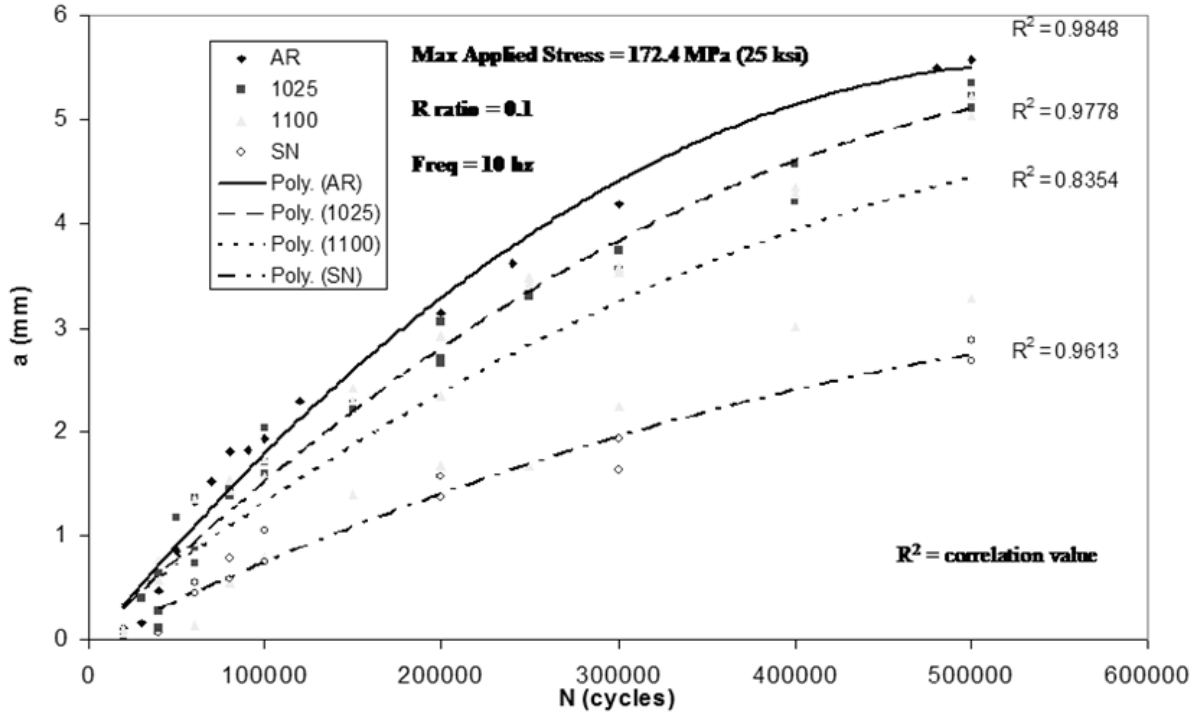

Figure 5.22 Comparison between results of embedded Ti crack length (a) vs constant amplitude fatigue cycles (N) for 4 Ti heat treatments in a [45/0/-45/0/Ti]s at 172.4 MPa (25 ksi) (range of data to 500k cycles)

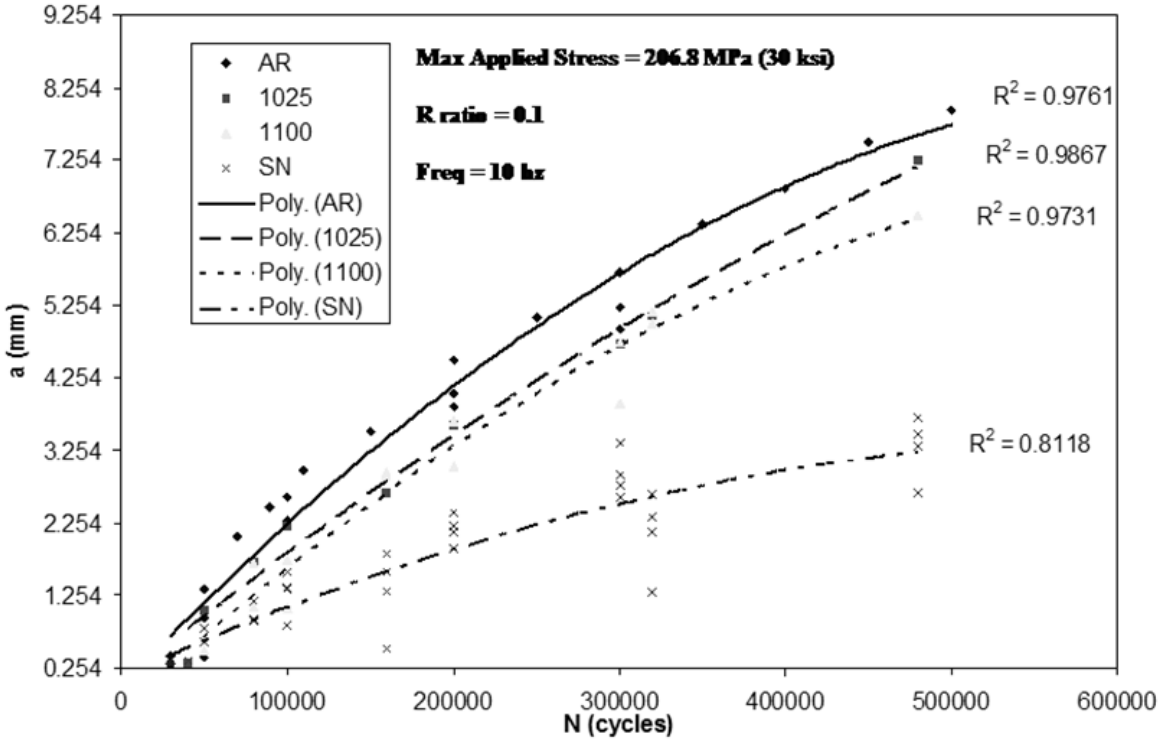

Figure 5.23 Comparison between results of embedded Ti crack length (a) vs constant amplitude fatigue cycles (N) for 4 Ti heat treatments in a [45/0/-45/0/Ti]s at 206.8 MPa (30 ksi) (range of data to 500 k cycles) from initial crack length of .254 mm (.01 in)

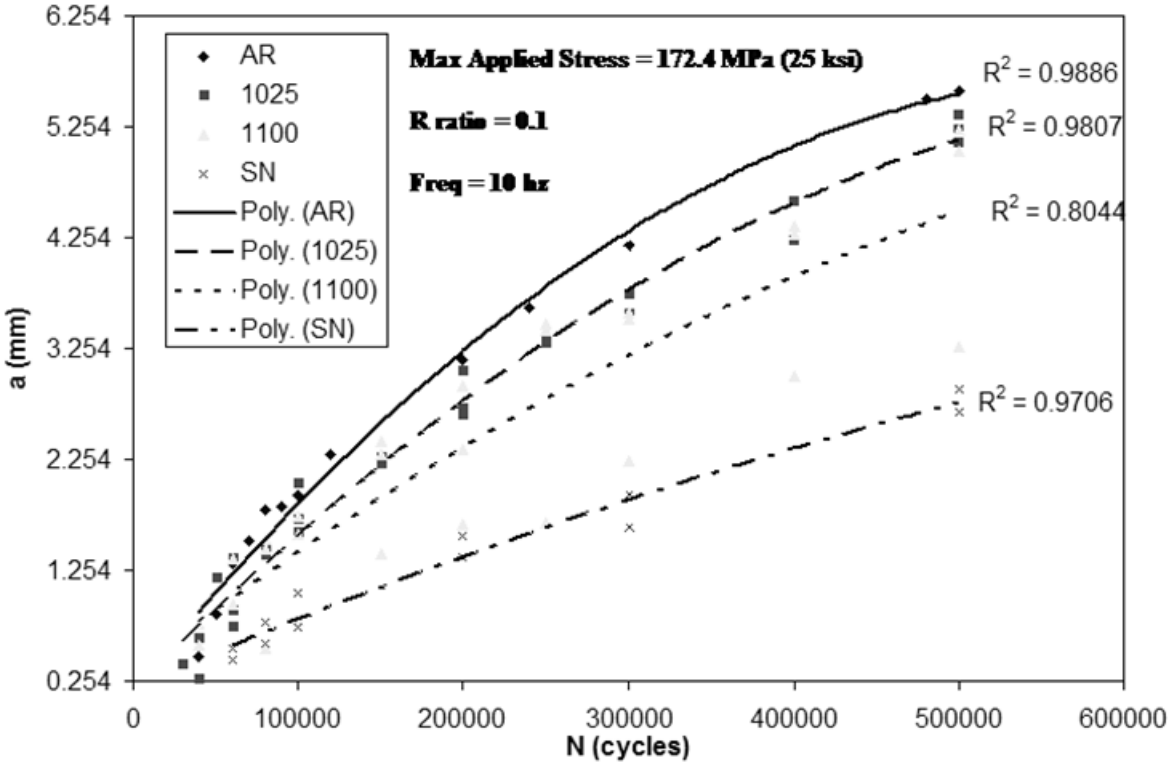

Figure 5.24 Comparison between results of embedded Ti crack length (a) vs constant amplitude fatigue cycles (N) for 4 Ti heat treatments in a [45/0/-45/0/Ti]s at 172.4 MPa (25 ksi) (range of data to 500 k cycles) from initial crack length of .254 mm (.01 in)

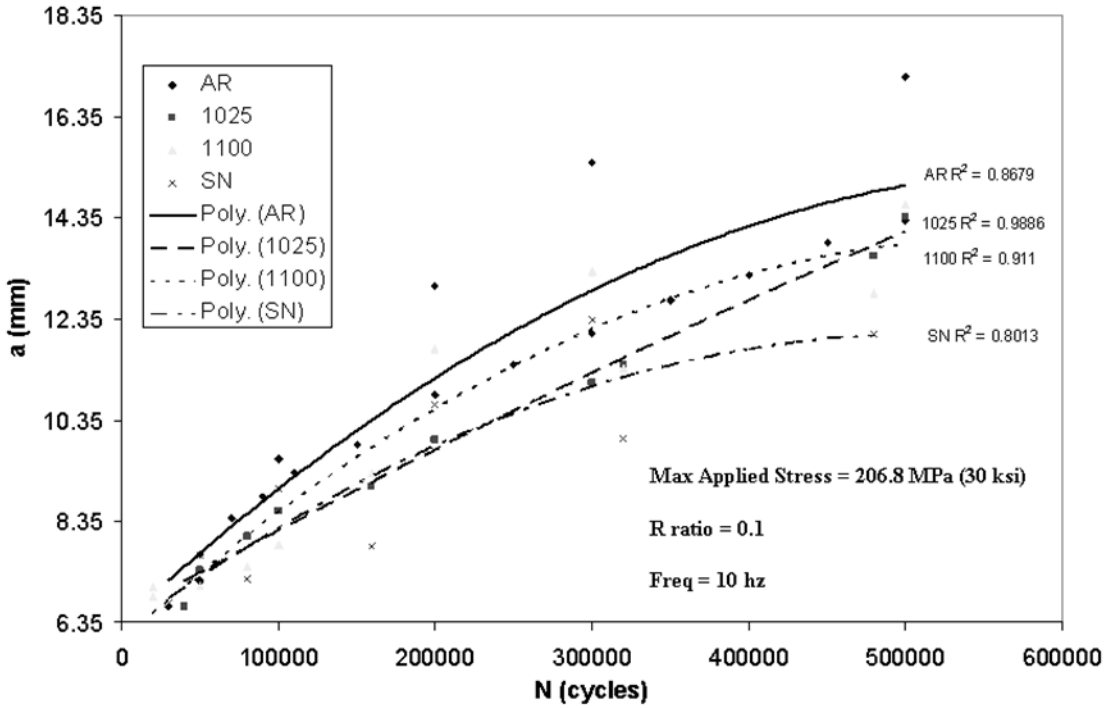

Figure 5.25 Comparison between results of embedded Ti crack length (a) vs constant amplitude fatigue cycles (N) for 4 Ti heat treatments in a [45/0/-45/0/Ti]s at 206.8 MPa (30 ksi) (range of data to 500 k cycles) from initial crack length of .254 mm (.01 in) from crack tip to crack tip including open hole

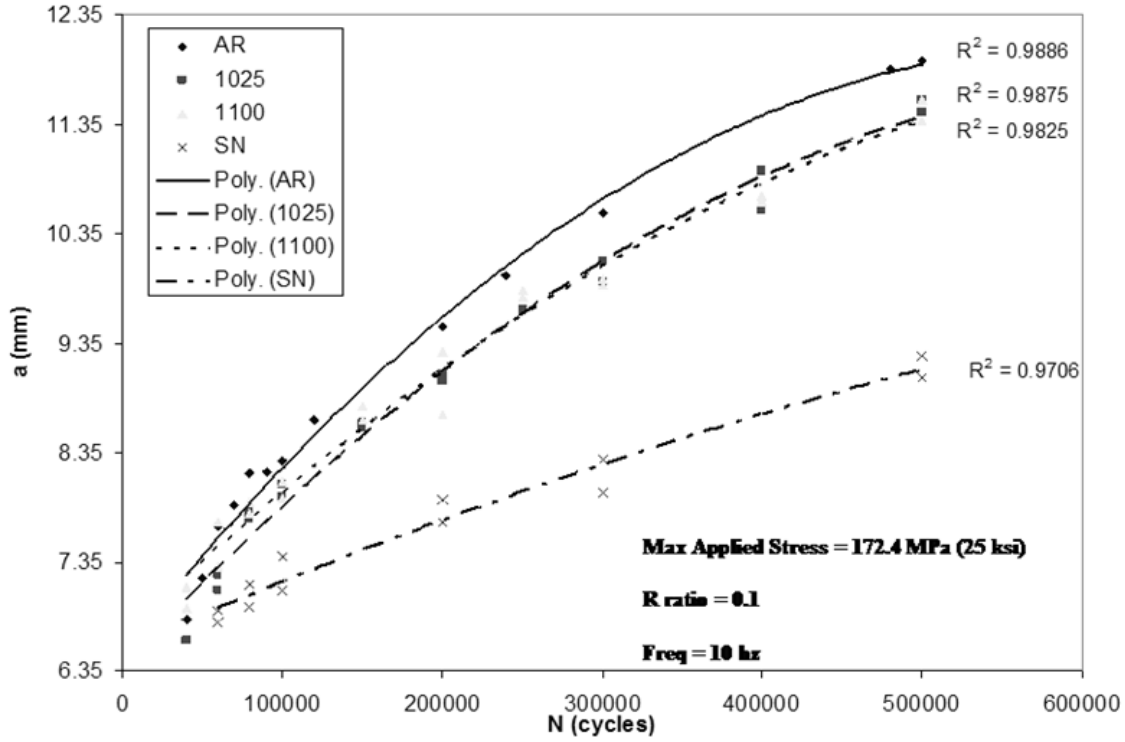

Figure 5.26 Comparison between results of embedded Ti crack length (a) vs constant amplitude fatigue cycles (N) for 4 Ti heat treatments in a [45/0/-45/0/Ti]s at 172.4 MPa (25 ksi) (range of data to 500 k cycles) from initial crack length of .254 mm (.01 in) from crack tip to crack tip including open hole

The final observation is more for future research using radiographic imaging. The image quality and contrast of the x-rays decreased as the ductility of the embedded Ti foil increased. Based on the results of the foil tensile tests two explanations can be developed. First, and less likely, explanation was that small cracks form in the higher stress regions near the open hole and allow additional x-rays to pass through the material which reduces the sharpness of the dominant crack. Second, is that the jagged fracture

surface of a ductile material causes shielding of some of the x-rays which leads to contrast problems.

5.1.2.4 Compliance

Testing was conducted to determine if a crack initiation in the Ti ply led to a stiffness loss in the HTCL laminate. A series of specimens were outfitted with an extensometer to collect strain data at initial state prior to fatigue testing at 206.8 MPa (30 ksi) and after a crack had been determined by replicate and x-ray.

The results of this analysis showed that the stiffness of the HTCL coupon did not show a definitive change between damaged and undamaged laminates. The strain values at initial state and after damage initiation were within the error range of the extensometer. This can be explained by the fact that the carbon fiber plies with 0° fiber orientation dominate the overall mechanical properties of the laminate. With no damage or broken fibers in these 0° plies, their higher elastic modulus easily assumes the increased load from the damaged plies.

5.1.2.5 Delamination

For all FMLs the preferred response to fatigue loading would be a controlled delamination, because this leads to stable crack growth. Therefore, great importance must be placed on the ratio of crack length and delamination area when fiber bridging efficiency is needed to increase damage tolerance of the laminate. Two methods were employed to determine if and to what extent delamination and other damage mechanisms were occurring.

5.1.2.5.1 Radiographic Delamination Inspection

In order to determine the extent of damage created during the fatigue testing on the HTCL specimens beyond cracking of the Ti ply additional x-ray techniques were utilized. The initial method of introducing a dye penetrant, zinc iodide, into the damage region proved inconclusive. A series of penetration soak times and varying levels of x-ray exposure showed no distinguishable change between the images with penetrant and without penetrant. Zinc Iodide has the highest relative radiographic opacity value of any inorganic penetrant [46]. The use of organic penetrants was not considered due to their volatile nature and associated increased safety concerns.

These results lead to two possibilities. First, that the relative opacity of the titanium, when compared to the zinc iodide, was so much greater that in order for x-rays to penetrate the Ti foil the signature of the dye penetrant was washed out and lost. Second, is that there was little to no delamination or other damage occurring besides the mixed mode cracking of the Ti ply.

5.1.2.5.2 Thermoelastic Stress Analysis

The inconclusive results from the radiographic delamination inspection called for another form of non destructive evaluation. Thermoelastic stress analysis (TSA) was used to determine if delamination was occurring between the Ti ply and the adjacent fiber reinforced PMC layers. TSA is a process where the changing thermal signature of surface of the material can be equated to a change in stress state. If the internal damage mechanisms produced sufficient heat through plasticity and friction, this heat would then radiate to the surface and provide a real time view of damage progression.

First a pre-fatigued specimen, with known crack geometry and lengths in the Ti ply, was cycled at a maximum stress of 206.8 MPa (30 ksi) at R=0.1 with a frequency of 10 Hz until it reached a thermal steady state. The specimen had been previously tested to 500 k fatigue cycles and had a detailed x-ray analysis. Figure 5.27 shows the positive qualitative correlation between the infared image of the HTCL specimen's surface and the accompanying x-ray image with respect to crack origin. The crack mouth can easily be distinguished in the IR image (at 4 and 10 o'clock positions), but crack length and growth direction was not as obvious. It was originally estimated that the areas of high emissivity, which stand out as lighter regions, indicated a delamination zone.

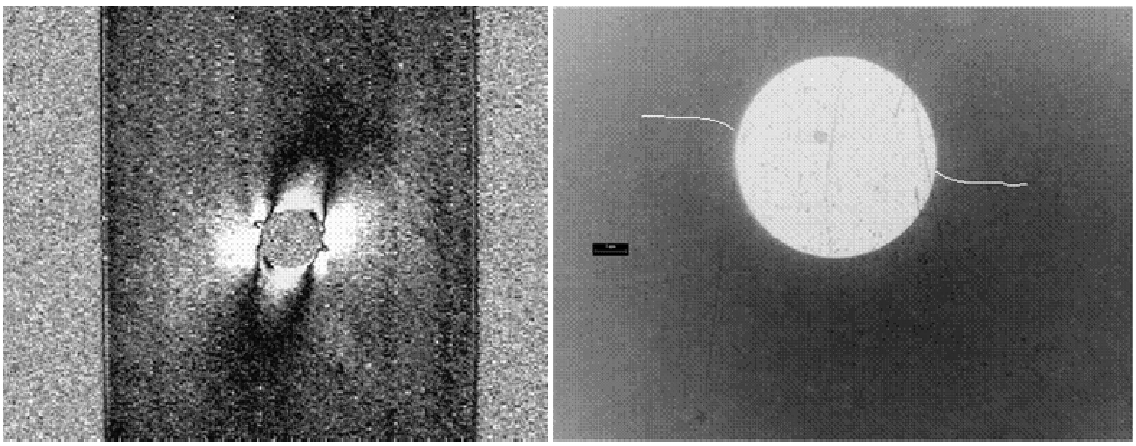

Figure 5.27 TSA image (left) and constrast inverted x-ray image (right) of pre-fatigued specimen at a maximum stress of 206.8 MPa (30 ksi) at R=0.1 with a frequency of 10 Hz (cracks have been manually highlighted from the orginial x-ray image)

Following the TSA evaluation of the previously damaged specimen a destructive evaluation was preformed to correlate this possible delamination and identify other damage present through the width adjacent to the open hole. Figure 5.28 shows the cross

section of the HTCL specimen at a distance of 2 mm (.07 in). There appeared to be no delamination between the Ti ply and the adjacent fiber reinforced PMC layers. Destructive sectioning of a HTCL specimen was not able to show that delamination was occurring at the Ti / PMC interface. It is suspected that debonding is occurring at the Ti / PMC interface, but that without external load applied to the specimen no separation occurs. Interlaminar cracking was observed in the upper -45° ply, which suggests that the mixed mode loading within the laminate was strong enough to damage the toughened epoxy matrix but not the adhesive interface between the Ti and PMC enough to be visible. This was not a positive damage mechanism like the controlled delamination mechanism covered in section 2.4.2. It is possible that the HTCL laminate would fail through this interlaminar crack growth. This cracking was observed in all sectioned specimens and approximately corresponded with the lighter regions in the IR imaging used for TSA.

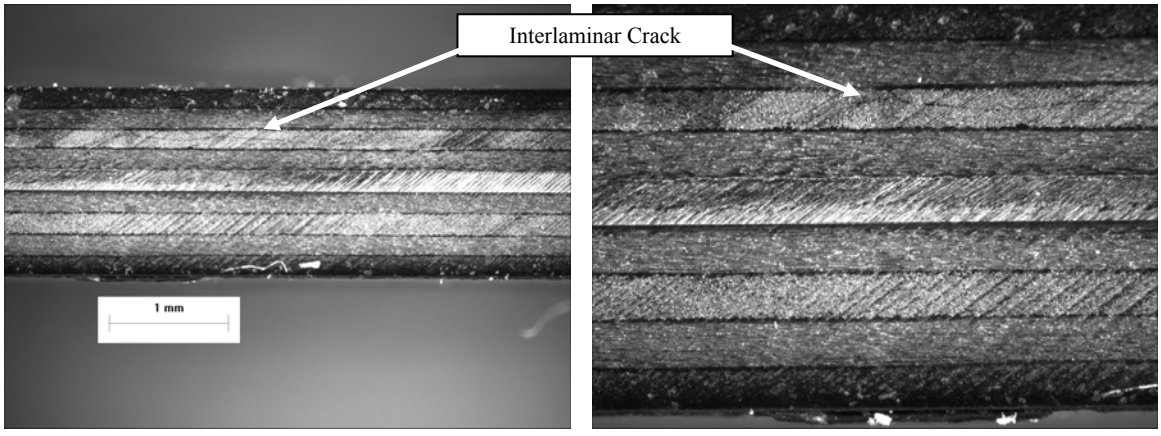

Figure 5.28 Interlaminar Crack as seen in wide view (left) and close view (right) in section of HTCL cut 2mm (.07 in) from center open hole

The second TSA analysis started with a HTCL specimen that had not been previously fatigue cycled. Initial IR and x-ray images were taken to ensure that no cracking or damage existed prior to the initiation of fatigue testing. The initial IR image, Figure 5.29, showed non-uniform surface preparation with the flat black paint. These areas showed up as dark spots on the IR camera. It was decided to remove the initial paint coating and reapply. The resulting IR image is seen in Figure 5.31. Initial crack detection was observed at 22,000 fatigue cycles via the IR camera, as seen in Figure 5.30. The specimen was then removed from the TSA test frame and a x-ray image was taken to validate the TSA findings. A crack was observed in the same area of the HTCL as was indicated by the IR images. Fatigue cycling with TSA continued to 80,000 cycles and additional x-ray images where taken. At 180,000 fatigue cycles a second crack was observed in the Ti foil using the IR camera. This can be seen in Figure 5.32. An x-ray image was again taken to validate the IR image. The IR images and the x-ray images correlated extremely well for initial crack detection, but crack length could not be determined. Additional experimentation would be required to determine the stress state on the surface of the specimen with an IR image in the TSA system. The TSA system for the purposes of this limited analysis shows great promise on a qualitative basis, but more research would be required to determine if quantitative data could be obtained.

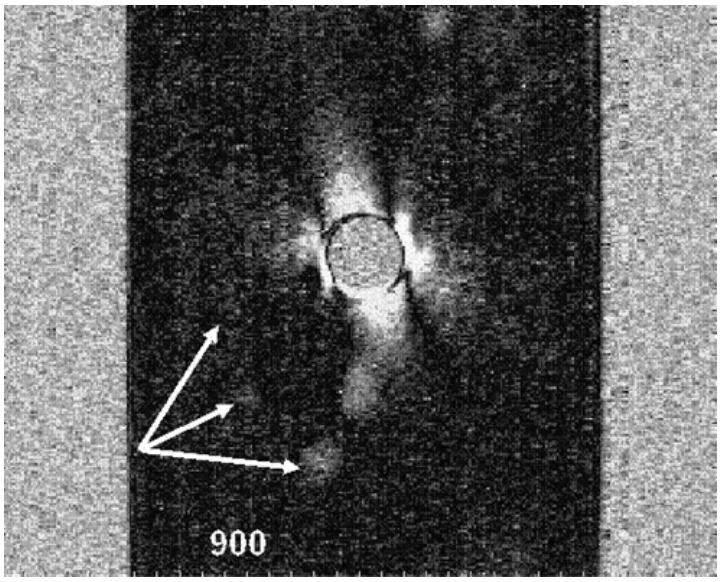

Figure 5.29 TSA image of HTCL specimen after 900 fatigue cycles at a maximum stress of 206.8 MPa (30 ksi) at R=0.1 with a frequency of 10 Hz. (Arrows indicate regions of non-uniform surface coating)

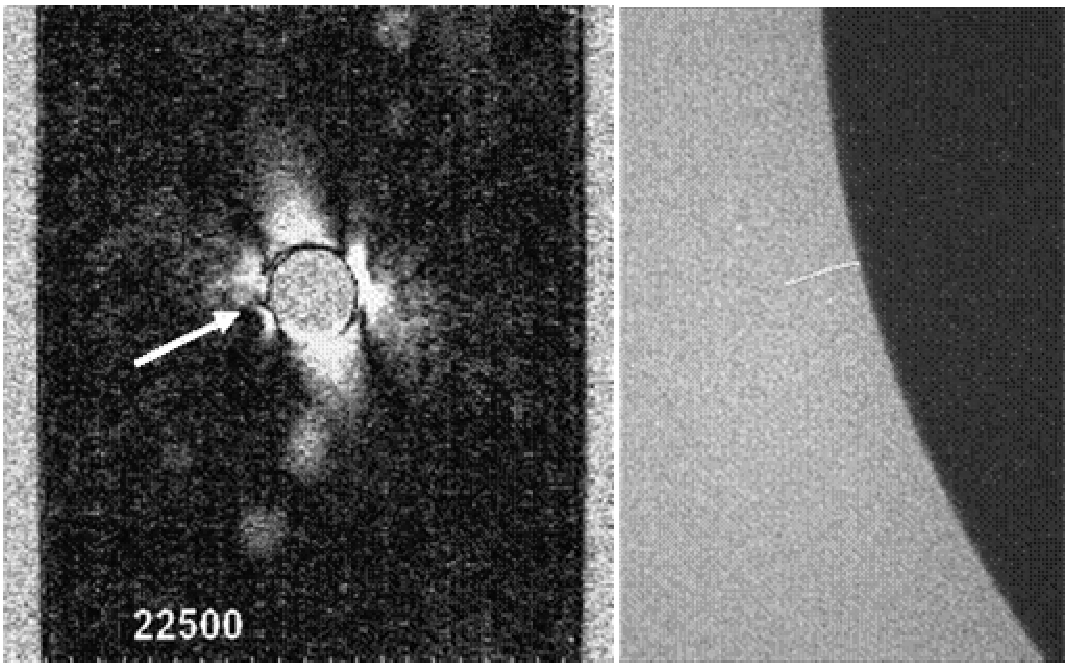

Figure 5.30 TSA image (left) and x-ray image (right) of HTCL specimen after 22,500 fatigue cycles at a maximum stress of 206.8 MPa (30 ksi) at R=0.1 with a frequency of 10 Hz. (Arrow indicates regions of initial crack detection) (x-ray image enhanced)

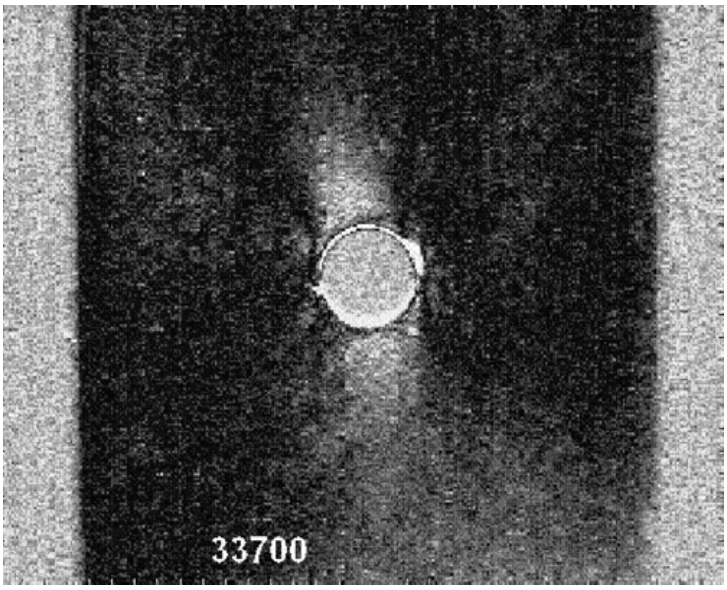

Figure 5.31 TSA image of HTCL specimen after 33,700 fatigue cycles at a maximum stress of 206.8 MPa (30 ksi) at R=0.1 with a frequency of 10 Hz. (Following application of new surface coating)

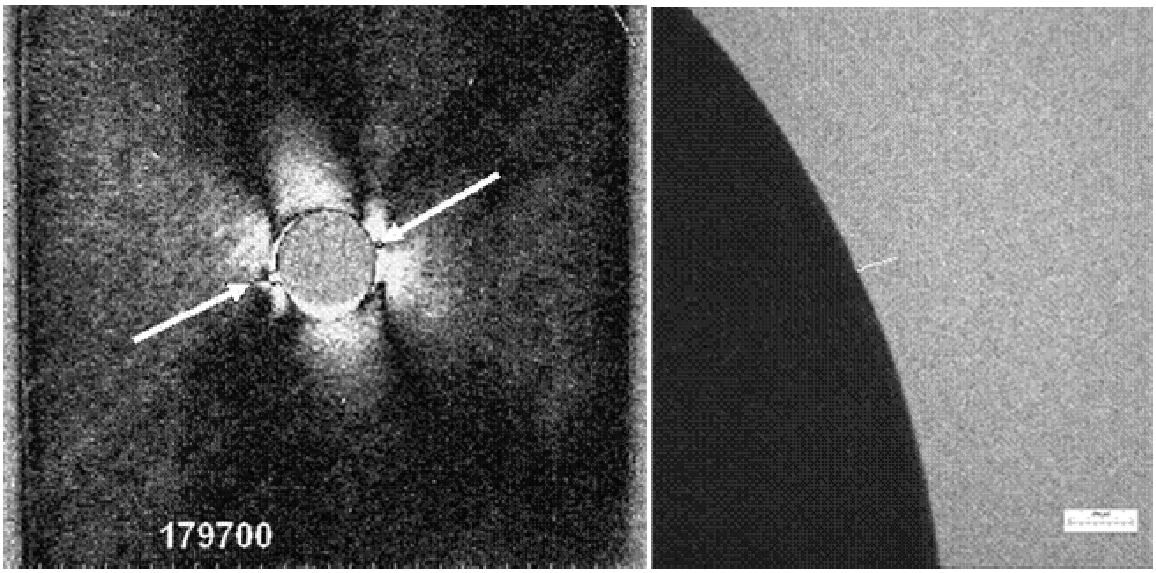

Figure 5.32 TSA image (left) and x-ray image (right) of HTCL specimen after 179,700 fatigue cycles at a maximum stress of 206.8 MPa (30 ksi) at R=0.1 with a frequency of 10 Hz. (Arrows indicate regions of cracks present) (x-ray image enhanced)

5.2 Analytical Predictions

An analytical analysis was conducted to determine initial loading conditions for use in the fatigue tests. Understanding the stresses that will be imparted on the embedded titanium ply near the open hole are required for proper testing.

5.2.1 Embedded Ti Ply Stresses

The maximum local stresses near the hole in the y-direction for the embedded Ti ply were determined using a MATLAB code based on classical laminate theory outlined in section 4.2. These values which are tabulated in Table 5.7 were used in conjunction with the values from the ANSYS analysis (see section 5.3.1) to determine cyclic fatigue stress values. All values remained within the linear elastic region of the Ti when compared to the values in Table 5.2 with the exception of the SN HTCL at a maximum applied load of 206.8 MPa (30 ksi).

Table 5.7: Maximum local stresses near the hole in the y-direction for the embedded Ti ply as calculated using a MATLAB code based on classical lamination theory

	Heat Treatment			
	AR	1025	1100	SN
Max Applied Stress MPa (ksi)	σ_{22max}	σ_{22max}	σ_{22max}	σ_{22max}
206.8 (30)	965.3 (140)	951.5 (138)	937.7 (136)	820.5 (119)
172.4 (25)	834.2 (121)	813.6 (118)	792.9 (115)	682.6 (99)
158.6 (23)	779.1 (113)	751.5 (109)	730.8 (106)	641.2 (93)
137.9 (20)	661.9 (96)	641.2 (93)	634.3 (92)	558.5 (81)

5.3 Finite Element Modeling

A finite element analysis was conducted to determine stresses and material response of the embedded Ti ply in the HTCL systems. The results from this analysis are presented in the following sections. Additional information is also provided on initial work conducted to determine energy release rate of the cracked ply using a virtual crack closure technique.

5.3.1 Ply Stress Analysis

The maximum stresses in the y-direction were determined using ANSYS modeling techniques. These values which are tabulated in Table 5.8 were used in conjunction with the analytical values for the previous section to determine cyclic fatigue stress values. As in the previous section all values remained within the linear elastic region of the Ti when compared to the values in Table 5.2 with the exception of the SN HTCL at a maximum applied load of 206.8 MPa (30 ksi).

Table 5.8: Maximum local stresses near the hole in the y-direction for the embedded Ti ply as calculated using ANSYS modeling

	Heat Treatment			
	AR	1025	1100	SN
Max Applied Stress MPa (ksi)	σ_{22max}	σ_{22max}	σ_{22max}	σ_{22max}
206.8 (30)	917.0 (133)	903.2 (131)	889.4 (129)	772.2 (112)
172.4 (25)	765.3 (111)	751.5 (109)	744.6 (108)	634.3 (92)
158.6 (23)	703.3 (102)	696.4 (101)	682.5 (99)	592.9 (86)
137.9 (20)	613.6 (89)	599.8 (87)	592.9 (86)	510.2 (74)

The stresses from the ANSYS model were then applied to the stress concentration factor (K_t) equation to calculate the associated K_t for each combination of Ti foil temper and max remote applied load. The results in Table 5.9 show an as expected decrease in the K_t from the as received to the solution treated condition. The K_t remained fairly constant for each heat treatment with different applied loading.

Table 5.9: Stress concentration factors (SCF) at the open hole for the HTCL laminate as calculated using ANSYS modeling and analysis

	Heat Treatment			
	AR	1025	1100	SN
Max Applied Stress MPa (ksi)	K_t	K_t	K_t	K_t
206.8 (30)	4.43	4.36	4.3	3.7
172.4 (25)	4.44	4.36	4.32	3.7
158.6 (23)	4.43	4.39	4.3	3.7
137.9 (20)	4.45	4.35	4.3	3.7

The results from the ANSYS finite element modeling also proved that the modeling program could possibly provide insight into the unusual crack geometry associated with embedded Ti foils in HTCL specimen under load. Stress profiles were observed in the quarter symmetry model under load that correlated well with the actual path of crack growth in the embedded Ti ply. A modified image of this can be seen in Figure 5.33.

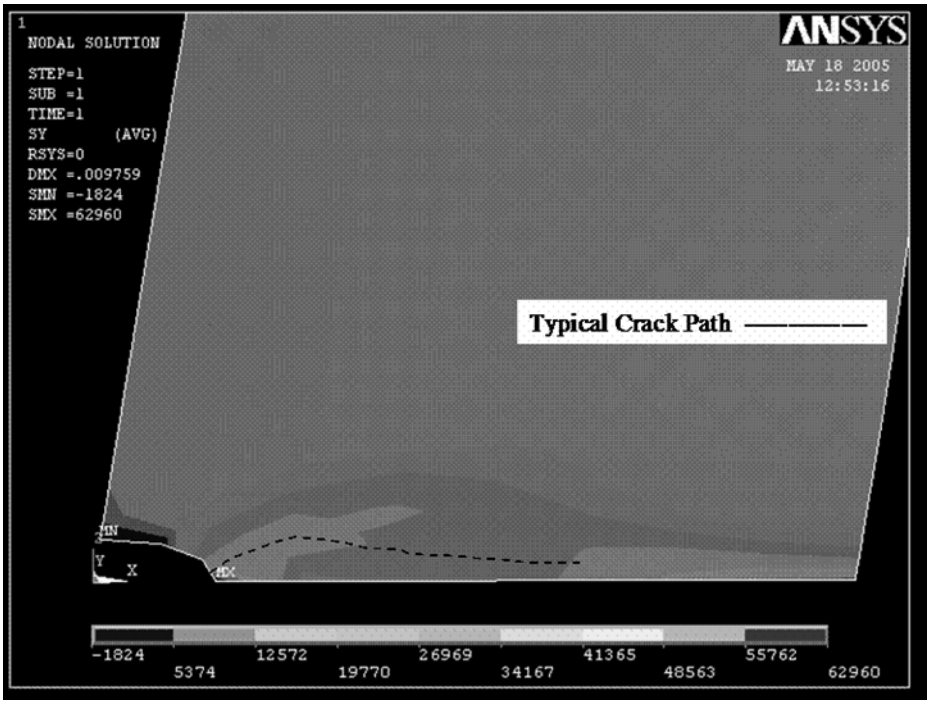

Figure 5.33 ANSYS image with typical crack path traced on surface of stress profile of Ti ply under load

Initial work was conducted on modeling a HTCL specimen with a crack growing in the embedded ply. The goal of this work was to determine the stress intensity factors or the associated energy release of the system as a crack propagated through the embedded foil using a virtual crack closure technique. While it was possible to generate a crack in the model using nodal release at the boundary conditions, the shape and extent of delamination were not obtained. The use of an estimated delamination region could be a quick fix, but the unusual nature of the damage mechanisms in the HTCL specimen as witnessed in radiographic analysis and TSA suggest further evaluation prior to implementation.

Figure 5.34 and Figure 5.35 show the extent of the modeling completed to date with respect to the embedded Ti. Load transfer is visible in both images and expected material deformation is seen in the adjacent 0° fiber PMC plies.

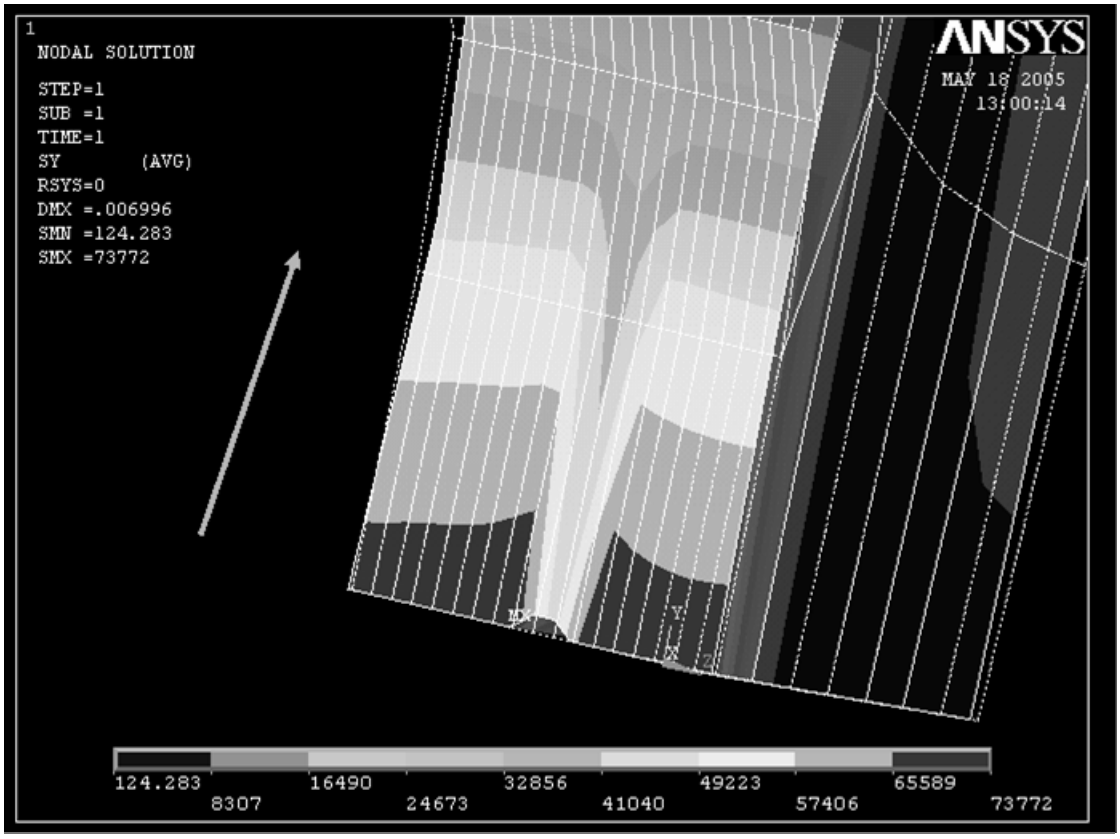

Figure 5.34 ANSYS model of 9 ply HTCL (18 sections) with solid 46 nodes released in center section of laminate to replicate a perfect mode I crack (Arrow indicates direction of applied stress)

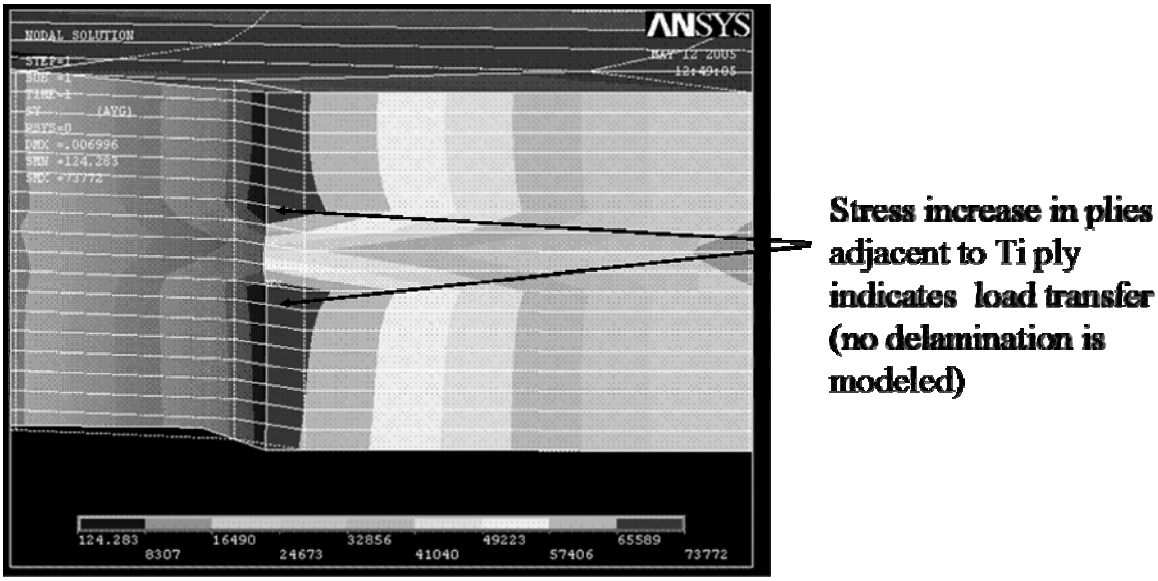

Figure 5.35 Through length view of ANSYS model with load transfer visible following solid 46 nodes release

CHAPTER 6

CONCLUSIONS

An experimental research program was designed to evaluation the crack growth characteristics in hybrid titanium composite laminates (HTCL) via in-situ radiography and determine the mechanical properties of the constituent Ti-15-3 foil. Destructive and non destructive evaluation techniques were utilized to determine the extent of damage created by fatigue testing. Analytical analysis and finite element modeling were employed to determine laminate stress-strain responses for applied loading.

Monotonic testing was conducted on β Ti-15-3 foil dogbone coupons with four separate tempers. The foil had been subjected to four different heat treatments that resulted in varying mechanical properties. The as received (AR), STA 1025 heat treatment (1025), and STA 1100 heat treatment (1100) foils had similar average modulus values of 14.9 Msi, 14.6 Msi, and 14.3 Msi, while the solution treated (SN) foil was less stiff at 11.9 Msi. The AR, 1025, and 1100 yielded at 1.16 GPa (168 ksi), 1.01 GPa (147 ksi), and .917 GPa (133ksi) respectively. These tempered alloys were observed to strain harden upon yielding. The SN alloy yielded at .661 GPa (96 ksi) and no hardening was observed during elongation. Average elongation % for the AR, 1025, 1100 and SN alloys were 9, 10.5, 13 and 22 respectively. Decreasing ultimate strength values were seen starting with AR at 1.24 GPa (180 ksi), 1025 at 1.11 GPa (161 ksi), 1100 at 1.01 GPa (147 ksi) and finally SN at .710 GPa (103 ksi). The fracture surfaces of the AR, 1025, and 1100 were predominantly oblique fractures with visible Luder's bands, while the SN fracture surfaces were fraction oblique with ductile characteristics. The

microscopic images of the AR, 1025 and 1100 show aligned grains with alpha (α) precipitates in a beta (β) matrix. The higher volume % of α precipitates (HCP crystalline structure) in the AR foil leads to increased mechanical strength. Images of the SN foil show a mostly β matrix (BCC crystalline structure) with more ductile characteristics. Higher heat treatment temperatures with shorter aging times lead to increasing ductility and improved damage tolerance, but decreased mechanical strength.

The HTCL laminates were manufactured with a [45/0/-45/0/Ti/0/-45/0/45] balanced, symmetric layup using the previously mention β Ti-15-3 foil embedded as the Ti ply. Straight sided open-hole coupons were constant amplitude fatigue tested to determine crack growth characteristics via in situ radiography at various stress levels. A polymer matrix composite (PMC) matrix digestion process was utilized to validate crack measurements made of Ti foil embedded in the HTCL. Crack initiation, which occurs on the atomic level, cannot be determined with radiographic inspection. An initial reliably detectible crack size of 0.254 mm (.01 in) could be determined at remote applied stress at 286.8 MPa (30 ksi) and 172.4 MPa (25 ksi) at R=0.1 with a frequency of 10 Hz. First cracks in these specimens appeared between 10,000 and 40,000 fatigue cycles. Cracks smaller than 0.254 mm (.01 in) were detected at approximately 200,000 to 300,000 fatigue cycles at a remote applied stress of 158.6 MPa (23 ksi), but none propagated past this reliably detectible value. No cracks of any size were detected in HTCL coupons, to 1,000,000 fatigue cycles, when a remote stress of 137.9 MPa (20 ksi) was applied.

Fatigue crack growth rates, within the titanium ply, were characterized for the HTCL coupons of varying embedded Ti foil tempers. The specimens fatigue tested at 286.8 MPa (30 ksi) and 172.4 MPa (25 ksi) produced fatigue crack growth that was

initially quicker and then retarded as the crack length increased. The HTCL with the SN foil embedded showed a 232% and 65% reduction in average final crack length verses the next closest HTCL type following 500,000 fatigue cycles for applied stresses of 286.8 MPa (30 ksi) and 172.4 MPa (25 ksi) respectively. Fatigue crack growth rates decrease in all cases following an initial fast growth phase and heat treatment of the embedded Ti ply greatly affects crack growth rates. The combination of fiber bridging and the toughness of the Ti foil control the growth rate.

The fatigue cracks in general did not initiate at locations on the edge of the open hole that were exactly perpendicular to the applied loading. Cracks initially grow away from the open hole at shallow angles and then turned to grow perpendicular to the loading. This resulted from the notch sensitivity of the Ti ply and the anisotropy of the HTCL system. In most cases multiple cracks were visible in the initial fatigue life stage and then a certain number of those cracks dominated.

The use of dye penetrants to highlight damage mechanisms, other than crack growth in the titanium ply, via in-situ radiography proved inconclusive. This was attempted to map out the debonded areas in and around the PMC / Ti interface. It is believed that the opacity of the Ti ply does not allow the comparatively much lower opacity of the zinc iodide penetrant to appear on the resulting x-ray images.

For this reason thermoelastic stress analysis (TSA) was employed to determine the delamination area in the wake of the crack tip and identify other HTCL fatigue crack events. The infared (IR) imaging utilized in TSA proved its ability at this point to deliver qualitative data on a limited number of HTCL specimens. It is believed that early crack detection and other damage mechanisms can be obtained for both surface and subsurface

regions. This methodology is only applicable under live cyclic loading, therefore it may not be a useful NDI tool in service.

Destructive sectioning of a HTCL specimen was not able to show that delamination was occurring at the Ti / PMC interface. We do suspect that debonding is occurring at the Ti / PMC interface, but that without external load applied to the specimen no separation occurs. Interlaminar crack growth was observed in the -45 degree ply which suggests that the adhesive interface between the Ti foil and the adjacent PMC ply is tougher than the matrix material in the PMC. This would be a negative damage mechanism due to its uncontrollable nature.

It is has been suggested that delamination may not be occurring in this particular HTCL layup due to the compliant nature of the polymer epoxy matrix that is used in the fiber reinforced PMC. Previous HTCL specimens had an alternating layup of Ti foil and PMC prepreg which created a dimpling effect in the metal foil that possibly created debonding under fatigue loading. As these previous HTCL specimens were cyclically loaded the adjacent Ti foils would narrow due to Poisson effect and create delamination. With one ply of Ti foil , as in this HTCL layup, the matrix material in the surrounding plys would simply comply and create no debonding. Further evaluation is required to prove or disprove this theory.

Both analytical analysis, classical lamination theory, and finite element methods, ANSYS, showed good correlation when comparing HTCL mechanical properties and stress concentration factors at the open hole. The analytical values tended to be more conservative than the FE values. The FE results also proved good correlation of internal stress states with actual crack growth geometry. Initial modeling of crack growth within

the Ti ply using FE methods appears promising, but additional experimental data is required for proper characterization.

In general it is concluded that the HTCL specimen with the embedded SN treated β Ti-15-3 appears to be the most promising of the candidate laminates. In general this is an extremely promising material for aerospace and other applications due it advantageous material properties and excellent damage tolerance characteristics, such as lower crack growth rates and improved toughness.

CHAPTER 7

RECOMMENDATIONS

There are many areas for further investigation with respect to hybrid titanium composite laminates (HTCL) development. Novel uses of combined experimental, evaluation and modeling techniques could lead to the possibility of implementation of this type of hybrid material on future aircraft and other structural applications. A possible next step for the HTCL evaluation would be bearing resistance testing in a controlled environment followed by filled hole tension-tension testing. It maybe found that the softer SN Ti ply may not perform as well here and one of the other heat treatments is a better material fit.

Further evaluation of HTCL laminates using thermoelastic stress analysis (TSA) could provide for a better understanding of stress states within the laminate. The correlation of surface temperature changes with changing stress levels created by fatigue damage would be interesting to develop. This understanding could further be employed to make design, manufacturing and maintenance decisions. The real time imaging capability of TSA makes it a possible field NDE technique.

Continued finite element analysis work should be conducted to model the full damage profile of the HTCL laminates to help optimize design in an empirical approach. Results of this modeling would need to be experimentally validated, but a large time savings could be realized if this occurred.

For future in-situ radiographic imaging it is recommended that at least 50% of the applied fatigue load be used to hold the crack fully open. So long as the load is within the elastic limit of all materials employed no further damage would be realized. The possible acquisition of a digital imaging plate and associated imaging software would enhance an already promising evaluation technique.

REFERENCES

1. Krishnakumar, S., *Fiber Metal Laminates - The Synthesis of Metals and Composites.* Materials and Manufacturing Processes, 1994. **9**(2): p. 295-354.

2. Kaufman, J.G., *Fracture Toughness of 7075-T6 and -T651 Sheet, Plate and Multilayered Adhesive-Bonded Panels.* Journal of Basic Engineering, 1967. **89**: p. 503-507.

3. Johnson, W.S. and J.M. Stratton, *Effective Remote Stresses and Stress Intensity Factors for an Adhesive Bonded Multi-Ply Laminate.* Engineering Fracture Mechanics, 1977. **9**: p. 411-421.

4. Johnson, W.S., *Damage Tolerance Evaluation of Adhesively Laminated Titanium.* Journal of Engineering Materials and Technology, 1983. **105**: p. 182-187.

5. Treasurer, P., *Plane Stress vs. Plane Strain Schematic*, F.M.L.P.-G.I.o. Technology, Editor. 2005: Atlanta, GA.

6. Volgelesang, L.B. and J.W. Gunnink, *A State of the Art, ARALL, Material for the Next Generation of Aircraft*, D.o.A. Engineering, Editor. 1983, Delft University of of Technology: The Netherlands.

7. Verbruggen, M., *Aramid Reinforced Aluminum Laminates: ARALL*, in *Report LR-503*. 1986, Delft University of Technology.

8. Bucci, R.J., Mueller, L.N., Schultz, R.W., and Prohaska, J.L. *Advanced Materials Technology '87*. 1987.

9. Rhymer, D.W., *Conversation concerning ARALL use on C-17 aircraft*. 2005: Atlanta, GA. p. Coffee Talk.

10. Young, J.B., Landry, J.G.N. and Cavoulacos, V.N., *Crack Growth and Residual Strength Characteristics of two grades of glass-reinforced aluminum 'Glare'.* Composites Structures, 1994. **27**: p. 457-469.

11. Shim, D.J., Alderliestien, R. C., Spearing, S. M., and Burianek, D. A., *Fatigue crack growth predictions in GLARE hybrid laminates.* Composites Science and Technology, 2003. **63**(12): p. 1759-1767.

12. Dornheim, M.A., *Low-fatigue material saves weight in A380.* Aviation Week & Space Technology, 1995.

13. Grabilnikov, A.S., Mashinskaya, G. P., Zhelezina, G. F., Zinevich, O. M. and Deyev, I. S., *Interlaminar Fracture Toughness of a Hybrid Composite Material of the ALOR Type.* Mechanics of Composite Materials, 1994. **30**(2): p. 136-145.

14. Freischmidt, G., Coutts, R.S.P., Janardhana, M.N., *Aluminum/lithium Alloy-Carbon Fibre/Epoxy Laminated hybrid Composite Material Part I, Preliminary Results.* Journal of Materials Science Letter, 1994. **Vol. 13**: p. 1027-1031.

15. Ritchie, R.O., Yu, W. and Bucci, R.J., *Fatigue Crack Propogation in ARALL^P Laminates: Measurement of the Effect f Crack-Tip Shielding from Crack Bridging.* Engineering Fracture Mechanics, 1989. **32**(3): p. 361-377.

16. Gutierrez, S.E. and R.D. Bradshaw, *Fatigue and Crack Investigation of Aluminum Fiber Metal Laminates.* 2005.

17. Miller, J.L., Progar, D. J., Johnson, W. S. and St. Clair, T. L., *Preliminary Evaluation of Hybrid Titanium Composite Laminates*, N.A.S. Administration, Editor. 1994, Langley Research Center: Hampton, Virginia.

18. Li, E., *Characterization of Mechanical and Fatigue Properties for a Hybrid Titanium Composite Laminate*, in *Material Science and Engineering*. 1997, Georgia Institute of Technology: Atlanta, GA. p. 210.

19. Marissen, R., *Fatigue crack growth in ARALL-A hybrid aluminum-aramid composite material*. 1988, Delft University of Technology.

20. Cobb, T.Q., *Optimization of hybrid Titanium Composite Laminates*, in *Materials Science and Engineering*. 1998, Georgia Institute of Technology: Atlanta, GA.

21. Burianek, D.A., Giannakopoulos, A. E. and Spearing, S. M., *Modeling of facesheet crack growth in titanium-graphite hybrid laminates, part I.* Engineering Fracture Mechanics, 2003. **70**(6): p. 775-798.

22. Rhymer, D.W. and W.S. Johnson, *Fatigue damage mechanisms in advanced hybrid titanium composite laminates.* International Journal of fatigue, 2002. **24**(9): p. 995-1001.

23. Davidson, D.L. and L.K. Austin, *Fatigue Crack Growth Through ARALL-4 at Ambient Temperature.* Fatigue Fracture Engineering Structures, 1991. **14**(10): p. 939-951.

24. Lin, C.T. and P.W. Kao, *Delamination growth and its effect on crack propagation in carbon fiber reinforced metal laminates under fatigue loading.* Acta Mater, 1996. **44**(3): p. 1181-1188.

25. Bakuckas, J.J.G. and W.S. Johnson, *Application of Fiber Bridging Models to Fatigue Crack Growth in Undirectional Titanium Matrix Composites.* Journal of Composites Technology & Research, 1993. **Fall**.

26. Macheret, J., Teply, M. and Winter, E.F., *Delamination Shape Effects in Aramid-Epoxy-Aluminum (ARALL) Laminates with Fatigue Cracks.* Polymer Composites, 1989. **10**(5): p. 322-327.

27. Johnson, S., and Rhymer, D., *Determination of Residual Stresses of Titanium Foil During Cure of TiGr Laminate*, T.B. Company, Editor. 2003, Georgia Institute of Technology.

28. Shames, A., Rosenblum, M., and Treple, W.B., *Cold Formin Titanium 15-3 Alloy*, in *Manufacturing Technologies Division*, A.F.W.A. Laboratories, Editor, Fairchild Republic Company: Long Island, NY.

29. Rosenberg, H.W., *"Ti-15-3: A New Cold-Formable Sheet Titanium Alloy".* *Journal of Metals*, (November 1983): p. 30-34.

30. Wells, M., *Light Metals Lecture 18: Titanium*. 2004, University of British Columbia.

31. Bania, P.J., Lenning, G.A. and Hall, J.A., *Development and Properties of Ti-15V-13Cr-3Sn-3Al (Ti-15-3).* Beta Titanium Alloys in the 1980's. 1984, Warrendale, P.A., 1984: The Metallurgical Society of AIME.

32. Boyer, R., Welsch, G., Collings, E.W. *Titanium Alloys*. in *ASM International*.

33. Breslauer, E. and A. Rosen, *Relationship Between Microstructure and Mechanical Properties in Metastable Beta-Titanium 15-3 Alloy.* Material Science and Technology, 1991. **May**: p. 441-456.

34. Kawabe, S. and S. Muneki, *Strengthing Capability of Beta Titanium Alloys*, in *Beta Titanium Alloys of the 1990's*, E.e. al., Editor. 1993, TNS: Warrendale, PA. p. 187.

35. Nishida, S. and e. al., *Effect of heat treatment on fatigue strength of Ti-15V-3Cr-3Sn-3Al alloy.* Transactions of the Japan Society of Mechanical Engineers, Part A, 1995. **v61**(n589): p. p 2016-2020.

36. Griffiths, B., *Boeing sets pace for composite usage in large civil aircraft.* Composite World, 2005(May).

37. Toray Carbon Fibers America, I., *Technical Data Sheet No. CFA-007*. 2005.

38. Sawicki, A.J. and P.J. Minguet, *Failure Mechanisms in Compression-Loaded Composite Laminates Containing Open and Filled Holes.* Journal of Reinforced Plastics and Composites, 1999. **18**(18).

39. Webber, K., *HTCL lay-up*. 2005, Georgia Institute of Technology: Atlanta, GA.

40. Talreja, R., *Damage Development in Composites: Mechanisms and Modeling.* Journal of Strain Analysis for Engineering Design, 1989. **24**(4): p. 215-222.

41. El-Hajjar, R.F., *Experimental Study and Analytical Modeling of Translayer Fracture In Pultruded FRP Composites*, in *School of Civil and Environmental Engineering*. May 2004, Georgia Institute of Technology: Atlanta, GA. p. 169.

42. Gyekenyesi, A.L. and G.Y. Baaklini, *Thermoelastic Stress Analysis: The Mean Stress Effect in Metallic Alloys*, G.R. Center, Editor. 1999, NASA (STI). p. 11.

43. Mallick, P.K., *Fiber-Reinforced Composites*. Second Edition ed. 1993: Marcel Dekker, Inc. c.

44. Lekhnitskii, S.G., *Theory of Elasticity of an Anisotropic Body*. 1963, San Francisco: Holden Day.

45. Dowling, N.E. *Fatigue at Notches and the Local Strain and Fracture Mechanics Approach*. in *ASTM STP 677*. 1979. Philadelphia: American Society for Testing and Materials.

46. Van Daele, R., Verpoest, I. and De Meester, P., *Detection of Damage in Composite Materials Using Radiography*, in *Manual on Experimental Methods for Mechanical Testing of Composites*, R.a.T. Pendleton, M., Editor. 1989, Society for Experimental Mechanics, Inc.: Bethel, CT. p. 115-127.